Acoustic propagation in forest environments : time domain numerical methods toward bioacoustic applications

Quentin Goestchel

THÈSE DE DOCTORAT

DE
LE MANS UNIVERSITE
SOUS LE SCEAU DE
LA COMUE ANGERS – LE MANS

ECOLE DOCTORALE N° 602
Sciences de l'Ingénierie et des Systèmes
Spécialité : Acoustique

Par
Quentin GOESTCHEL

Acoustic propagation in forest environments. Time domain numerical methods toward bioacoustic applications.

Thèse présentée et soutenue à Strasbourg, le 18 octobre 2023
Unité de recherche : Unité Mixte de Recherche en Acoustique Environnementale (UMRAE)
Thèse N° : 2023LEMA1014

Rapporteurs avant soutenance :

Maarten Hornikx	Full Professor, Eindhoven University of Technology
Régis Marchiano	Professeur des Universités, Sorbonne Université

Composition du Jury :

Président :	Simon Félix	Directeur de recherche CNRS, Le Mans Université
Examinateurs :	Ariane Emmanuelli	Maîtresse de conférences, Ecole Centrale de Lyon
Dir. de thèse :	Benoit Gauvreau	Directeur de recherche, Université Gustave Eiffel
Co-encadrant :	Gwenaël Guillaume	Chargé de recherche, Cerema
Co-encadrant :	David Écotière	Ingénieur Divisionnaire des Travaux Publics, Cerema

Invité(s)

Jérôme Sueur	Maître de conférences, Muséum National d'Histoire Naturelle

Le Mans University - UMRAE

PhD Thesis

Acoustic propagation in forest environments. Time domain numerical methods toward bioacoustic applications.

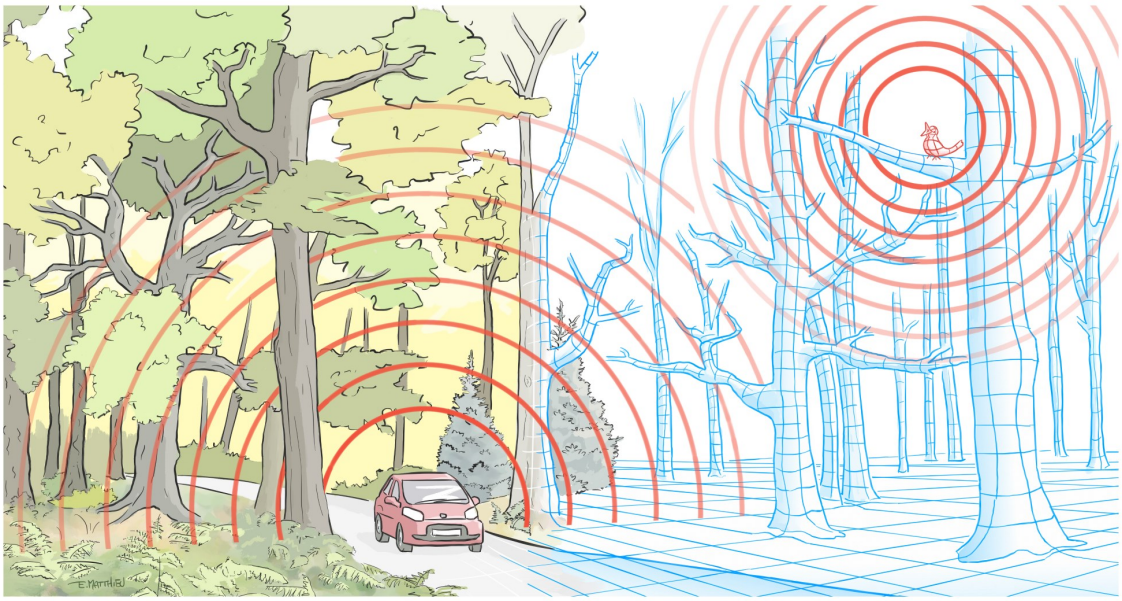

Author:
Quentin Goestchel

Director:
Benoit Gauvreau
Supervisors:
Gwenaël Guillaume
David Ecotière

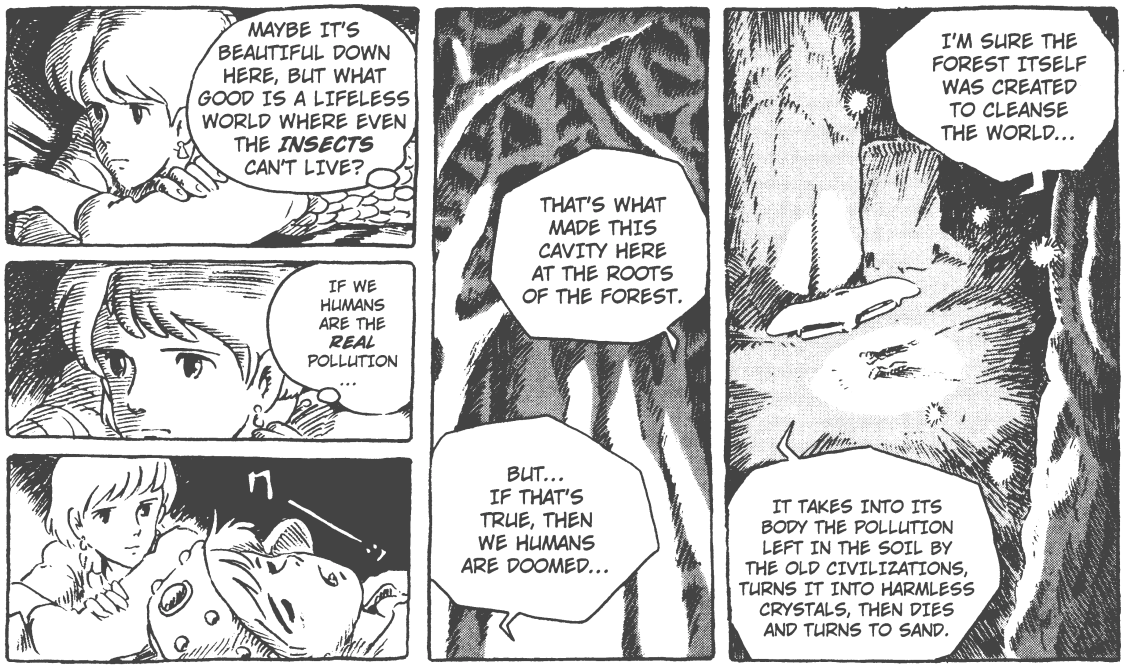

Nausicaä Of The Valley Of The Wind, Chapter 1. Hayao Miyazaki, 1982.

Contents

Abstract

This manuscript investigates sound propagation modeling in forest environments, intending to understand the limitations of existing models and explore their potential bioacoustic applications. The subject is introduced by presenting current concerns about the impact of noise on health and biodiversity. A literature review examines previous studies and existing outdoor sound propagation models, both analytical and numerical, for their applicability to forest scenarios. Then, as a time-domain solver, the Transmission Line Matrix (TLM) model is thoroughly investigated, and the update of its theory allows for highlighting limitations when modeling outdoor long-range sound propagation. Numerical experiments are presented to quantify the subsequent errors and limitations in the TLM model. The computational implications of modeling a significant number of points implied by large frequency-distance ratios are discussed. Finally, some applications to model sound propagation within forests, with multiple impedance boundary conditions, are presented, and a validation method is proposed through comparisons with in-situ measurements at the Nouragues research station (French Guiana). Overall, this research contributes to the understanding of how to simulate sound propagation within forests and the potential practical applications that can arise from it.

General introduction

1 Environmental and societal context

Noise is now widely acknowledged as a form of pollution, imposing environmental and health burdens on living organisms [100, 108]. From a human perspective, noise exposure emerges as a critical public health issue, capable of exacerbating cardiovascular and stress-related conditions for instance [97]. Moreover, accurately identifying and isolating factors responsible for health problems to assess their specific effects remains a prevailing and unsolved challenge. In light of this, the concept of Disability Adjusted Life Years (DALYs) presents itself as a valuable indicator, capturing the impact of hazards on life expectancy while accounting for the affected individual's well-being [54, 108]. The latter is crucial in understanding the impact of noise on human health, as it predominantly induces indirect effects that lead to discomfort and disabilities. Recently, the social cost of noise in France was estimated at 147.1 billion euros per year, giving an additional metric to grasp the outcomes of this nuisance [36, 92].

Adopting a more wildlife-centered perspective, similar observations can be drawn, given that environmental stresses also have an impact on animals and biodiversity in general. However, the scientific literature concerning this specific subject is presently less extensive compared to that which focuses on humans [118]. Indeed, establishing a causal link between the disappearance of a particular taxon and a specific factor among various interrelated external stresses remains a complex challenge [99, 79]. Moreover, discerning the impact of noise in the presence of mixed factors such as food scarcity, habitat modification, or temperature rises is crucial for raising awareness and implementing effective preservation measures [47, 118, 120]. Anthropogenic noise is known to have an impact on animal communication (see [21] and references therein) as it masks some useful acoustic signals and can mislead animals when they communicate about food foraging, potential dangers or reproduction. Avian-based studies also reveal that modifications of acoustic signals in the presence of anthropogenic noise are a common response for taxa that can adapt [44]. To better understand the actual biodiversity crisis and the role played by anthropogenic activities in this imbalance, gathering data about populations and their habitat is of crucial importance [32]. Consequently, various wildlife population monitoring approaches exist and are improving with technological advancements [135].

Within this context, the characterization and preservation of existing quiet areas is an important matter for humans and ecosystems altogether [98]. In Europe, the subject is addressed by the Directive 2002/49/EC that legislates the assessment and management of environmental noise [3]. Indeed, determining the areas where noise levels are acceptable is a primary step, particularly by requiring that they be identified and preserved. According to a misleading intuition, protected areas such as forests are considered quiet. For a rough idea, only 27 % of Europe's protected Natura 2000 sites are considered havens of quiet [98], and even in a protected forest, aircraft noise can be dominant around the year [58]. In the United States, protected areas are actually exposed to twice the noise levels predicted by sound models [23]. Hence, monitoring these sites non-invasively and gathering information on wildlife populations serves a double purpose and coincides with European legislation.

2 Research questions and objectives

Among the monitoring methods introduced as essential in the preceding context, passive acoustic monitoring appears to be a promising approach [55]. Indeed, acoustic signals can be recorded continuously throughout the year and day, providing valuable insights into animal behavior and distribution with minimal invasiveness. When it comes to acoustic monitoring of animal populations, most of the measurement campaigns focus on the question of marine mammals and birds [118]. Indeed, vocal communication must be a characteristic of the studied specimen to record an acoustic signal. In Europe, a recent study expresses global alarming trends for bird population, with an estimated overall decline of -25% between 1996 and 2016 [111]. A meaningful insight from this study is that agricultural intensification is the main factor of such decline, with farmland species decreasing by approximately -60%. For woodland species, the global decline is estimated to -18%, which makes forests a good starting candidate to study and attempt to mitigate this trend. Thus, understanding acoustic propagation in the medium that species use as a communication vector appears as a key point. The main research question emerges from this last observation: can sound propagation models be of assistance to passive acoustic monitoring in the framework of biodiversity conservation?

In the scientific literature concerning outdoor sound propagation through vegetation, forests - or tree belts - are mostly studied as potential noise barriers to protect areas from transportation noise (railways, roads). The interest in sound propagation through vegetation mostly started from sound propagation through crops and extended further to more and more comprehensive considerations [7, 50]. Thus, the present doctoral work focuses on sound propagation in forests at a finer space scale, focusing on the sound fields *within* the forest. As bird monitoring increasingly becomes a key point for biodiversity preservation, getting insights about sound fields in woodland and potential help from numerical methods is one of the objectives of this document. Indeed, when recording sound signals in a forest, little is known about the area covered by the measurements. Hence, including sound field modeling in the process to optimize microphone positions could induce potential cost reductions and improve measurement reliability.

Recently, research has begun to move in this direction. For instance, a semi-analytical physics-based model has been used to predict the acoustic detection distance in forests and study its variations across seasons [70]. The approach of this study is to summarize the studied forests as attenuation coefficients calculated from measurements along a one-dimension transect. This assumes that the forest is a homogeneous environment so that the proposed method can be generalized, making it already applicable to further in-situ studies. Another example is the use of a numerical sound propagation model to assess the influence of meteorological conditions and mountainous topography on birds' active spaces, showing the benefits of such interdisciplinary cooperation for bird monitoring [59]. This method uses a frequency-based model that has proven efficient to model long-range sound propagation scenarios. Its limitations come from the fact that two-dimensional simulations are rotated around an axis to model three-dimensional scenarios.

In the present Ph.D. work, the research is more preliminary and the main objectives are to determine the potential help that outdoor sound propagation models such as the Transmission Line Matrix model (TLM) could bring to forest bioacoustics. The feasibility study encompasses the study of a three-dimensional full-wave model for forest scenario modeling. As every model is an approximation, assessing the overall reliability of available methods is also part of the goals addressed in this document. Another objective, prior to using a numerical model in a field application, is to confront simulation results to in-situ measurements to evaluate the reliability of the model.

3 Structure of the manuscript

To assess the potential use of numerical methods to model sound propagation within forests and the additional data they can provide to assist passive acoustic monitoring, this manuscript is divided into four chapters.

Chapter one. Existing models that could potentially apply to sound propagation in forests are introduced through a literature review. The analytical model for sound waves in complex media is outlined, along with some of its existing derivations for forest modeling. Then, various numerical methods that model sound propagation are presented, among the TLM model, a numerical method that has been developed at the Joint Research Unit in Environmental Acoustics (UMRAE) over the last decades. An overview of outdoor sound propagation phenomena is then proposed, addressing the implementation of acoustic impedance boundary conditions in time-domain numerical methods and impedance models. Overall, the chapter aims at giving insights to the reader about current practices in outdoor sound propagation modeling.

Chapter two. A theoretical update of the TLM theory is proposed. The formalism is partially revised to conduct stability analyses of the model, in its formulation applied to homogeneous and inhomogeneous media. The outcomes of the analyses enable the introduction of the numerical dispersion effect and its potential impacts on simulated sound pressure levels. Furthermore, the chapter examines time-domain source specifications and boundary conditions with particular interest in modeling sound propagation within forests.

Chapter three. Based on the theoretical results of the previous chapter, the focus shifts to an investigation and quantification of inherent numerical errors within the TLM model. The main concern is to assess its reliability when applied to outdoor scenarios representative of forest acoustics. Beginning with a presentation of the TLM model's implementation details, the accuracy of the model is evaluated through source validation procedures. The effects of anisotropic numerical dispersion in free-field and interfering wave fields are studied, relying on numerical experiments and error quantification.

Chapter four. This last part contains a preliminary study informed by the results of the previous chapters. The main objective is to present the practical applications of the TLM method to the modeling of sound propagation within forests. To begin with, methodological approaches for generating 3D forest geometries are presented. Then, the chapter explores the use of digital forests generated from statistical datasets and showcases the application of TLM simulations within this context. Furthermore, the methodology for comparing numerical simulations to acoustic measurements made in French Guiana is detailed. The comparison is then exploited to provide insights into the model's performance and potential practical applications.

Finally, a conclusion summarizes all the relevant findings and key points throughout the manuscript. Discussions of these results and subsequent perspectives are suggested as potential future projects identified by this Ph.D. work.

4 Scientific contributions related to this doctoral work

Publications

- [Under submission process] Goestchel, Q., Guillaume, G., Ecotière, D., & Gauvreau, B. (2023). Transmission Line Matrix Model: Numerical Dispersion Effects on Simulated Specular Reflection. SSRN Scholarly Paper, 4398222. *10.2139/ssrn.4398222*
- Goestchel, Q., Guillaume, G., Ecotière, D., & Gauvreau, B. (2022). Analysis of the Numerical Properties of the Transmission Line Matrix Model for Outdoor Sound Propagation. *Journal of Sound and Vibration*, 116974. *10.1016/j.jsv.2022.116974*

Conference papers

- Goestchel, Q., Guillaume, G., Ecotiere, D., & Gauvreau, B. (2023). Transmission Line Matrix Method for sound propagation modelling in forests: comparison with in-situ measurements. In *Forum Acousticum*. [Incoming HAL link after conference]
- Goestchel, Q., Guillaume, G., Ecotiere, D., & Gauvreau, B. (2022). Properties of the Transmission Line Matrix Model for Outdoor Sound Propagation: Numerical Dispersion Effects. In *International Congress on Acoustics*. https://hal.science/hal-04007605

International Scientific Communications

- Sep, 2023 - 10$^{\text{th}}$ Forum Acousticum, Torino, Italy
  Oral presentation [Scheduled, in-person]: *Transmission Line Matrix Method for sound propagation modelling in forests: comparison with in-situ measurements*
- Oct, 2022 - 24$^{\text{th}}$ International Congress On Acoustics, Gyeongju, South Korea
  Oral presentation [Virtual]: *Properties of the transmission line matrix model for outdoor sound propagation: Numerical dispersion effects*

National Scientific Communications

- Jun, 2023 - Technical days on acoustics and vibration, Aix-en-Provence, France
  Oral presentation [Virtual]: *Propriétés du modèle TLM pour la propagation du son à l'extérieur: Effets de dispersion numérique*
- Jun, 2022 - Engineering Sciences Doctoral School Congress, Vannes, France
  Oral presentation [In-person]: *Acoustic propagation in forest environments. Numerical study for environmental applications*
- Fev, 2022 - 16$^{\text{th}}$ French Acoustics Society Congress, Marseille, France
  Oral presentation [In-person]: *Stability analysis of TLM model for sound propagation in outdoor environment*
- Oct, 2021 - 'Doctoriales' Planning, Mobility and Environment, Le Croisic, France
  Poster [In-person]: *Acoustic propagation in forest environments. Numerical study for environmental applications*

Chapter 1

Forests sound propagation modeling

This chapter explores the existing literature on modeling outdoor sound propagation, specifically focusing on forest environments and encompassing both analytical and numerical approaches. It exposes key aspects of outdoor sound propagation in complex media, aiming to provide a comprehensive understanding of sound behavior in forested areas.

The chapter begins with an investigation of analytical models that provide insight into the complex nature of sound propagation in forests. It examines the behavior of sound waves in complex media, based on the wave equation in inhomogeneous media. Moving on to numerical models, the chapter discusses various techniques employed to model sound propagation through and within forests. A brief comparison of different numerical methods is provided, offering an overview of their respective advantages and limitations. The chapter also underlies phenomena that are known to occur when sounds propagate outdoors, such as atmospheric absorption or wind and temperature effects. Their implications for accurate modeling of sound in forested environments are discussed. Furthermore, boundary conditions play a crucial role in modeling sound propagation in forests. Thus, this chapter details fundamental theoretical aspects such as the pressure reflection coefficient, acoustic impedance conditions, recursive convolution techniques, and impedance models suited for forests. In addition, the Perfectly Matched Layer (PML) technique is briefly introduced as a method for simulating open boundaries of computational domains.

1.1 Analytical model - Waves in complex media

Within the framework of sound propagation, understanding how acoustic waves interact with complex environments is crucial. Forests are challenging environments where the intricate arrangement of trees and the nature of the ground significantly affect the behavior of sound waves. A comprehensive literature review of the analytical theories applied to this problem has already been carried out during a previous doctoral research [26]. It covers topics such as the multiple scattering theory and the modeling of forests as sound crystals [129, 90, 52]. Here, the initial steps of the waves in complex media theory are introduced to provide additional insights into sound propagation in forests and the connections that exist among different theories. The following description is directly inspired by literature entries [14, 15] and [107, 103].

1.1.1 Wave equation in inhomogeneous media

In non-moving inhomogeneous media and in the absence of sources, the non-dissipative linear propagation of pressure waves is governed by the following Partial Differential Equation (PDE) [112]:

$$\Delta p(\vec{r},t) - \frac{1}{c^2(\vec{r})}\frac{\partial^2 p(\vec{r},t)}{\partial t^2} = 0, \tag{1.1}$$

where $p(\vec{r},t)$ denotes the acoustic pressure, representing a local pressure deviation around the ambient atmospheric pressure, and $\vec{r}$ is a vector describing the spatial coordinates. The environment schematized on Fig. 1.1 is considered as a realization of a random process of the positions of scatterers occupying the medium. Within these scatterers, the sound speed denoted as $c(\vec{r})$, differs from a reference sound speed c_0. $c(\vec{r})$ is considered spatially dependent in order to model the heterogeneity of the medium.

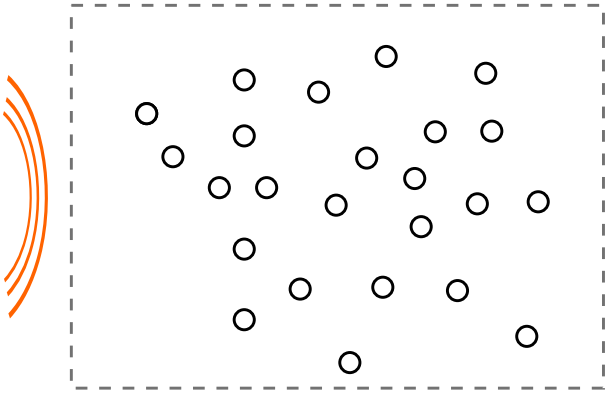

Figure 1.1. 2D Schematic view of an incident wave (orange) reaching a complex medium (represented as a box) randomly filled with scatterers (black circles).

Defining t as the time and $\omega = 2\pi f$ the angular frequency, the consideration of a monochromatic regime such as $p = \Psi(\vec{r})e^{i\omega t}$ in Eq. (1.1) leads to the Helmholtz equation for inhomogeneous media:

$$\Delta\Psi(\vec{r}) + \frac{\omega^2}{c^2(\vec{r})}\Psi(\vec{r}) = 0. \tag{1.2}$$

At this stage, the inhomogeneity potential $\mu(\vec{r})$ is introduced as:

$$\mu(\vec{r}) = 1 - \frac{c_0^2}{c^2(\vec{r})}, \tag{1.3}$$

where μ is a dimensionless random variable that describes the spatial inhomogeneity of the medium. Two main characteristics of μ must be defined before going further:

- m_μ, the statistic mean of μ such as $m_\mu = E\{\mu\}$ describing the distribution of scatterers over probabilistic random realizations.
- $R_{\mu\mu}$, the autocorrelation function of μ such as $R_{\mu\mu}(\vec{r}_1,\vec{r}_2) = E\{\mu(\vec{r}_1)\mu(\vec{r}_2)\}$ describing the similarity in the inhomogeneity at two different positions $\vec{r}_1$ and $\vec{r}_2$.

Introducing Eq. (1.3) in Eq. (1.2) gives another form of the Helmholtz equation for inhomogeneous media:

$$\Delta\Psi + k_0^2\Psi = k_0^2\mu(\vec{r})\Psi, \tag{1.4}$$

with $k_0 = \omega/c_0$ the free-field wavenumber.

Thus, the problem is reduced to solve Eq. (1.4) knowing the statistical parameters of the complex propagation media. For this, Green's functions are used, as for the homogeneous

media theory [112, 105]. First, let's recall that the free-field Green's function G_0 is defined as the solution of the wave equation for homogeneous media in the presence of an impulse source term $\delta(\vec{r}-\vec{r}_s)$ located in $\vec{r}_s$:

$$(\Delta + k_0^2)G_0 = \delta(\vec{r}-\vec{r}_s). \tag{1.5}$$

This function can be written under various forms, depending on the considered Fourier spaces:

$$G_0(\vec{r},t) = \frac{-1}{4\pi}\frac{\delta(t-|\vec{r}-\vec{r}_s|/c_0)}{|\vec{r}-\vec{r}_s|}, \tag{1.6}$$

$$G_0(\vec{r},\omega) = \frac{-1}{4\pi}\frac{e^{ik_0|\vec{r}-\vec{r}_s|}}{|\vec{r}-\vec{r}_s|}, \tag{1.7}$$

$$G_0(\mathfrak{q},\omega) = \frac{1}{k_0^2-\mathfrak{q}^2}, \tag{1.8}$$

$\mathfrak{q}$ being the spatial frequency domain counterpart (or Fourier dual) of $\vec{r}$. Similarly, the equation for inhomogeneous media is written:

$$(\Delta + k_0^2)G = k_0^2\mu(\vec{r})G + \delta(\vec{r}-\vec{r}_s), \tag{1.9}$$

where G is the solution of the Helmholtz equation with the source term $f(\vec{r},\vec{r}_s) = k_0^2\mu(\vec{r})G(\vec{r},\vec{r}_s)+\delta(\vec{r}-\vec{r}_s)$. Thus, following the approach employed in the homogeneous case, the solution is of the form:

$$G(\vec{r},\vec{r}_s) = \Psi_0(\vec{r}) + \int G_0(\vec{r},\vec{r}_1)\left[k_0^2\mu(\vec{r}_1)G(\vec{r}_1,\vec{r}_s)+\delta(\vec{r}_1-\vec{r}_s)\right]d^3r_1. \tag{1.10}$$

Providing the condition that there is no potential far away from the source, $\Psi_0(\vec{r}\gg\vec{r}_s)=0$ and the Green function for inhomogeneous media is then:

$$G(\vec{r},\vec{r}_s) = G_0(\vec{r},\vec{r}_s) + k_0^2\int G_0(\vec{r},\vec{r}_1)\mu(\vec{r}_1)G(\vec{r}_1,\vec{r}_s)d^3r_1. \tag{1.11}$$

However, the problem is more complex than in free field because Eq. (1.11) is recursive. A similar equation can be developed for Ψ if a source distribution $S(\vec{r}_s)$ is considered:

$$\Psi(\vec{r}) = \int G(\vec{r},\vec{r}_s)S(\vec{r}s)d\vec{r}_s, \tag{1.12}$$

$$\Psi(\vec{r}) = \int G_0(\vec{r},\vec{r}_s)S(\vec{r}s)d\vec{r}_s + k_0^2\int G_0(\vec{r},\vec{r}_1)\mu(\vec{r}_1)\int G(\vec{r}_1,\vec{r}_s)S(\vec{r}s)d\vec{r}_s d^3r_1, \tag{1.13}$$

$$\Psi(\vec{r}) = \int G_0(\vec{r},\vec{r}_s)S(\vec{r}s)d\vec{r}_s + k_0^2\int G_0(\vec{r},\vec{r}_1)\mu(\vec{r}_1)\Psi(\vec{r}_1)d^3r_1, \tag{1.14}$$

$$\Psi(\vec{r}) = \underbrace{\Psi_{\text{inc}}(\vec{r})}_{\text{Incident wave}} + \underbrace{k_0^2\int G_0(\vec{r},\vec{r}_1)\mu(\vec{r}_1)\Psi(\vec{r}_1)d^3r_1}_{\text{Multiple scattered wave}}. \tag{1.15}$$

Thus, as indicated by Eq. (1.15), the sound field can be decomposed into two terms: the direct field $\Psi_{\text{inc}}(\vec{r})$ between the source and the evaluation point $\vec{r}$ and the multiply scattered field described by a recursive term. The second term can be interpreted as the field reaching $\vec{r}_1$ ($\Psi(\vec{r}_1)$) being scattered by $\mu(\vec{r}_1)$ and traveling in the air ($G_0(\vec{r},\vec{r}_1)$) to the evaluation point $\vec{r}$.

1.1.2 Born's expansion

As an analogy to quantum scattering theory [15], it is possible to develop the recursive Eq. (1.11) as:

$$\begin{aligned} G(\vec{r},\vec{r}_s) &= G_0(\vec{r},\vec{r}_s) \\ &+ k_0^2 \int \underbrace{G_0(\vec{r},\vec{r}_1)}_{\vec{r}_1 \text{ to } \vec{r}} \underbrace{\mu(\vec{r}_1)}_{\text{interaction at } \vec{r}_1} \underbrace{G_0(\vec{r}_1,\vec{r}_s)}_{\vec{r}_s \text{ to } \vec{r}_1} d^3r_1 \\ &+ k_0^4 \int G_0(\vec{r},\vec{r}_1)\mu(\vec{r}_1)G_0(\vec{r}_1,\vec{r}_2)\mu(\vec{r}_2)G_0(\vec{r}_2,\vec{r}_s)d^3r_2d^3r_1 \\ &+ k_0^6 \int G_0(\vec{r},\vec{r}_1)\mu(\vec{r}_1)G_0(\vec{r}_1,\vec{r}_2)\mu(\vec{r}_2)G_0(\vec{r}_2,\vec{r}_3)\mu(\vec{r}_3)G_0(\vec{r}_3,\vec{r}_s)d^3r_3d^3r_2d^3r_1 \\ &+ \dots \end{aligned} \tag{1.16}$$

However, this sum of integrals is infinite. To overcome this, determining the ensemble average of the green function $< G >$ is a solution, considering that μ is a random variable with statistical parameters [15].

1.1.3 Field decomposition

Thanks to Eq. (1.15), an expression of the pressure field Ψ can be written. However, the recursivity of this equation makes it infinite. Thus, using the ensemble average to separate the coherent field from the diffuse field leads to:

$$\Psi =< \Psi > +\delta\Psi, \tag{1.17}$$

$<>$ being the ensemble average, and $\delta\Psi$ a "perturbation" representing the incoherent field. To evaluate the coherent and incoherent fields, further theories exist. Some of them are summarized below.

1.1.4 "Average" field and Dyson's equation

Thus, to express $< \Psi >$, a statistical approach is used considering all the possible realizations of the complex media. To achieve this, the $<>$ operator is applied to Eq. (1.16), and further assumptions are made regarding the inhomogeneity potential μ:

- $< \mu >= 0$, so that the sound speed is c_0 on average over all the possible realizations of the medium.
- μ is a random variable following a normal distribution, so the nth-order moments can be expressed depending on the associated autocorrelation function, $R_{\mu\mu}$.

Then Eq. (1.16) turns into:

$$\begin{aligned} < G(\vec{r},\vec{r}_s) > &= G_0(\vec{r},\vec{r}_s) \\ &+ k_0^4 \int G_0(\vec{r},\vec{r}_1)G_0(\vec{r}_1,\vec{r}_2)R_{\mu\mu}(\vec{r}_1,\vec{r}_2)G_0(\vec{r}_2,\vec{r}_s)d^3r_2d^3r_1 \\ &+ \dots \end{aligned} \tag{1.18}$$

Using Feynman diagrammatic theory and introducing the self energy operator $\sum(\vec{r}_1,\vec{r}_2)$, the Dyson equation can be derived from the previous calculations [15, 114]:

$$< G(\vec{r},\vec{r}_s) >= G_0(\vec{r},\vec{r}_s) + \int G_0(\vec{r},\vec{r}_1) \sum(\vec{r}_1,\vec{r}_2) < G(\vec{r}_2,\vec{r}_s) > d^3r_2 d^3r_1. \tag{1.19}$$

$\sum$ accounts for all orders of multiple scattering that cannot be factorized using the ensemble average. Unfortunately, its exact calculation is impossible in most cases (*e.g.* scattering through trunks, stems and leaves for instance). Making the additional hypothesis that μ is statistically spatially stationary leads to the demonstration that the "average" inhomogeneous Green's function is a double spatial convolution product (as denoted by the differential element $\partial\vec{r}$ of the convolution product *):

$$< G >= G_0 \underset{\partial\vec{r}}{*} \sum \underset{\partial\vec{r}}{*} < G > . \tag{1.20}$$

Applying a 3D spatial Fourier transform (written $\widehat{\ }$) and reformulating leads to this expression:

$$< \widehat{G} >= \frac{1}{k_0^2 - \widehat{\sum} - \mathfrak{q}^2}. \tag{1.21}$$

Recognizing the form of the homogeneous Green's function Eq. (1.8) leads to the conclusion that the coherent field interacts with the complex medium as if it was a spatially "averaged" medium with an effective wavenumber $k_{\text{eff}} = k_0^2 - \widehat{\sum}$. The difficulty resides in evaluating $\widehat{\sum}$, or calculating k_{eff} differently. Subsequently, two major properties can be extracted to describe the effective medium:

$$l_s = \frac{1}{2\,\text{Im}(k_{\text{eff}})}, \tag{1.22}$$

$$c_{\text{peff}} = \frac{\omega}{\text{Re}(k_{\text{eff}})}. \tag{1.23}$$

where l_s is the scattering mean free path and c_{peff} the effective phase speed for the coherent wave.

1.1.5 Bourret approximation

In this approximation, valid if the wave number is small compared to the correlation length of the scatterers $k_0 << l_\mu$, no 'loop' scattering paths are considered so

$$\sum(\vec{r}) = k_0^4 G_0(\vec{r}) R_{\mu\mu}(\vec{r}), \tag{1.24}$$

and the spatial Fourier transform of the self-energy becomes:

$$\widehat{\sum}(\mathfrak{q}) = -\frac{k_0^4}{\mathfrak{q}} \int_0^\infty e^{ik_0 r} R_{\mu\mu}(r) \sin qr dr, \tag{1.25}$$

This method is one of the existing methods used to approximate the effective wavenumber of a complex media, allowing to simplify the modeling of a coherent wave propagating through it [96].

Although additional methods exist, along with those used to estimate the incoherent field $\delta\Psi$ (using the Bethe-Salpeter, the radiative transfer or the diffusion equation [15]), they are not detailed in this document. The primary goal here is to introduce the concept of effective wavenumber, providing perspective on its application for modeling sound propagation through forests.

1.1.6 Complex media theory applied to sound propagation in forests

The effective medium theory employed in the literature offers a formulation of effective wavenumbers applicable to forest environments employing the 3D multiple scattering theory [107, 103, 102]. Specifically, this theory approximates the effective wavenumber by modeling tree trunks as finite vertical cylinders and canopy layers as diffuse scatterers of various shapes. It gives:

$$k_{\text{eff}}(\vec{r},\vec{u}) = k_0 + \frac{2\pi\nu}{k_0} f_{\text{scat}}(\vec{r},\vec{u}) \tag{1.26}$$

with $\vec{u}$ the unit vector in the propagation direction, ν the number of scatterers per unit volume and $f_{\text{scat}}(\vec{r},\vec{u})$ the scattering amplitude, calculated differently for the trunk layer or the canopy layer of the forest. While a comprehensive presentation of the underlying theory is beyond the scope of this document, it is explained in the existing literature [107]. Nevertheless, it holds significant promise for forest acoustics, as demonstrated in the application presented in Section 1.2.4. The author strongly recommends further exploration of this modeling technique in future developments of numerical methods.

In the following, an overview of existing numerical methods commonly employed to solve similar PDEs is given, as analytical problem formulations usually necessitate computational solutions when applied to specific complex scenarios.

1.2 Numerical methods - Solving waves PDEs in forests

This section aims to look into various numerical methods which could be used to model sound wave propagation in forest environments by solving Partial Differential Equations (PDEs). In the field of numerical methods, it is fundamental to distinguish between continuous (exact) and discrete (approximated) variables. For clarity, the following formulation convention is adopted throughout this document: numerically approximated values are written in upper case, while physically continuous values are written in lower case.

1.2.1 Discretization

As linear physical quantities are continuous, representing them numerically requires a discretization of space and time. For the following developments, the spatial domain is split equally (Fig. 1.2) in all directions with uniform step sizes $\Delta\ell$ such as $x_d = j_d\Delta\ell,\ j_d \in \mathbb{Z}$ and the time is decomposed into steps such as $t_n = n\Delta t,\ n \in \mathbb{N}$.

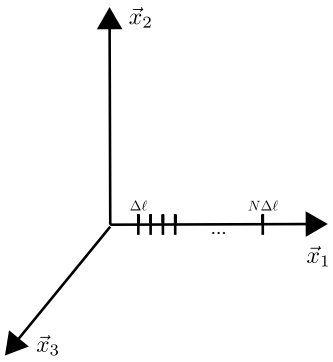

$$\begin{cases} x_1 = j_1\Delta\ell,\ j_1 \in \mathbb{Z} \\ x_2 = j_2\Delta\ell, j_2 \in \mathbb{Z} \\ x_3 = j_3\Delta\ell, j_3 \in \mathbb{Z} \end{cases}$$

Figure 1.2. Definition of the coordinates' discretization.

1.2.2 Ray-tracing methods

Ray-tracing models are based on a plane wave high-frequency approximation, *e.g.* when the wavelengths considered are small compared to the modeled obstacles ($\lambda \ll size_{\text{obj}}$) [115]. They consist in looking for solutions of Eq. (1.2) under this complex pressure form:

$$P_c = \sum_{m=1}^{N_{\text{rays}}} A_m \exp(i\phi_m) \tag{1.27}$$

with N_{rays} the number of considered rays, A_m their amplitudes, and ϕ_m their phases.

Simplifications of this model are widely implemented in engineering software and use geometric acoustic rays combined with empirical coefficients to simulate emission and sound propagation. In Europe, one of these methods has been standardized under '*Common Noise Assessment Methods*' (CNOSSOS-EU) [49], widely inspired by the NMPB-2008 [46]. Other methods have been developed in Denmark (Nord2000 [89]), the UK (TRANEX [68]) and the US (FHWA [11, 69]) with respective specificities in their implementation. Several comparisons of these models have been performed and showed that, depending on the application cases, discrepancies in the sound pressure level predictions appear (*e.g.* [86]). However, geometrical acoustics models imply simplifications. Thus, phenomena such as multiple scattering or frequency-dependent ground effects are not taken into account or approximated [124, 80].

Available open-sources codes.

- NoiseModelling. Open source library able to produce noise maps [17]. Available on https://github.com/Universite-Gustave-Eiffel/NoiseModelling
- ITAGeometricalAcoustics. Collection of C++ libraries to compute sound propagation based on the geometrical acoustics (GA) approach [116]. Available on https://git.rwth-aachen.de/ita/ITAGeometricalAcoustics.

The following sections present numerical methods that solve PDEs, which are more computationally demanding but include a wider range of physical phenomena.

1.2.3 Finite differences in time domain (FDTD)

The finite differences method theory relies on an application of the Taylor series expansion. For first-order derivatives modeled by a centered scheme, it can be generalized as [18]:

$$\begin{cases} \frac{\partial u(x_\ell)}{\partial x} + \mathcal{O}\left(\Delta\ell^{2M}\right) = \frac{1}{\Delta\ell} \sum_{m=-M}^{M} a_m u(x_\ell + m\Delta\ell), \\ k^*\Delta\ell = \sum_{m=1}^{M} a_m \sin(mk\Delta\ell), \end{cases} \tag{1.28}$$

where u is the quantity whose derivative is discretized and approximated to the order $2M$. The chosen coefficients $a_{-m} = -a_m$ and $a_0 = 0$ available in the literature [18] and the big $\mathcal{O}$ notation used to specify the approximation order of the method. This discretization process is usually used to solve the Linearized Euler Equations (LEE) (*i.e.* the wave equation as a system of two equations on acoustic pressure and particle velocity) [106, 40]. Optimized versions of these schemes exist in the literature and provide low-dispersion characteristics [122, 18]. The same generalization can be applied to second-order derivatives modeled by centered schemes, giving the following expression:

$$\begin{cases} \frac{\partial^2 u(x_\ell)}{\partial x^2} + \mathcal{O}\left(\Delta\ell^{2M}\right) = \frac{1}{\Delta\ell^2} \sum_{m=-M}^{M} a_m u(x_\ell + m\Delta\ell), \\ -k^{*2}\Delta\ell^2 = \sum_{m=1}^{M} \left[a_0 + 2a_m \cos(mk\Delta\ell)\right], \end{cases} \tag{1.29}$$

with $a_{-m} = a_m$ and $a_0 \neq 0$. Eq. (1.29) can be used to approximate the second-order partial derivatives in time and space of the scalar wave equation (Eq. (1.1)). Eqs. (1.28) and (1.29) represent $2M$-order schemes and the coefficients a_m can be calculated easily to cancel non-wanted Taylor terms. The second lines of Eqs. (1.28) and (1.29) represent the effective spatial dispersion equations with k^* the numerical effective wave number. They allow to understand the finite difference schemes under a dispersion-focused perspective. Fig. 1.3 shows a graphic representation of these equations compared to the non-approximated dispersion equation (*i.e.* $y = x$ in this case).

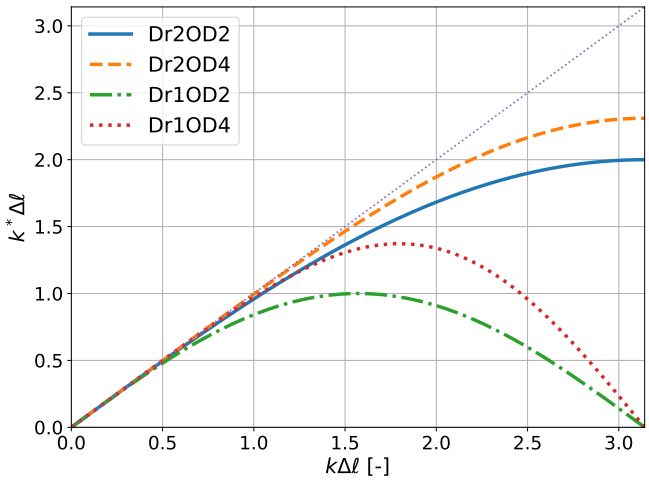

Figure 1.3. Normalized effective wave number for FDTD schemes, "Dr1OD2": first-order derivative, discretized at order two. "Dr1OD4", "Dr2OD2" and "Dr2OD4" designations follow the same logic.

Considering Fig. 1.3, the main conclusion is that applying finite differences to second-order derivatives leads to less dispersion than for first-order derivatives. To characterize this effect on approximated numerical speeds, the numerical dispersion relations for the second and fourth order are written. The one related to the second-order scheme is presented below:

$$\sin^2\left(\frac{\omega\Delta t}{2}\right) = \left(\frac{c\Delta t}{\Delta\ell}\right)^2 \sin^2\left(\frac{k\Delta\ell}{2}\right). \tag{1.30}$$

Then, the numerical phase speed $c_{\text{ph}} = \omega/k$, the velocity at which the phase of every frequency component of the wave travels, can be written as follows:

$$c_{\text{ph}} = \frac{2c_0 N_{\text{ppw}}}{\pi\sqrt{2}} \arcsin\left(\sqrt{\frac{1}{2}\sin^2\left(\frac{\pi}{N_{\text{ppw}}}\right)}\right), \tag{1.31}$$

with N_{ppw} the number of points per wavelength, a fundamental spatial discretization parameter thoroughly defined and used in Chapter 2. Conventionally, $C = \frac{c\Delta t}{\Delta\ell}$ is called the Courant number (from the convergence condition by Courant-Friedrichs-Lewy) [30]. For better comparison purposes with the TLM method, it is set to $\frac{\sqrt{2}}{2}$. Using this, the numerical dispersion relation related to the fourth-order scheme can be written:

$$\sin^2\left(\frac{\omega\Delta t}{2}\right) = C^2\sin^2\left(\frac{k\Delta\ell}{2}\right) + \frac{C^2(1-C^2)}{3}\sin^4\left(\frac{k\Delta\ell}{2}\right) \tag{1.32}$$

Available open-sources codes. Because of its intuitive approach to solving PDEs, the FDTD method is widely used and open-source initiatives are available. Below, two projects (usable and maintained at the time of writing this document) are listed:

- Pretty Fast FDTD (PFFDTD). Parallelized and GPU accelerated fast version of the FDTD for room acoustics available on https://github.com/bsxfun/pffdtd.
- SimSonic. Parallelized fast FDTD applied to the elastodynamic equations [19]. It is mostly used for research in ultrasound propagation in bones, it is freely available on http://www.simsonic.fr/.

1.2.4 Parabolic equation (PE) method

In this part, the theory relative to the 2D parabolic equation method is briefly presented as more details are available in the literature [115]. PE methods are based on the transformation of the hyperbolic form of the Helmholtz equation (Eq. (1.2)) into an approximated parabolic form. Among different PE formulations, the wide-angle parabolic equation (WAPE) can be expressed in Cartesian coordinates:

$$\left(\frac{\partial^2}{\partial x^2} + \frac{\partial^2}{\partial y^2} + \frac{\partial^2}{\partial z^2} + k^2(x,y,z)\right)\Psi(x,y,z) = 0, \tag{1.33}$$

with Ψ the complex acoustic pressure, $k(x,y,z) = \omega/c(x,y,z)$ the spatially dependent wavenumber and $c(x,y,z)$ the sound speed, traducing inhomogeneities in the propagation medium. The axisymmetric approximation around the z-axis leads to the parabolic form by allowing the assumption of a 2D $(\vec{x},\vec{z})$ plane of propagation invariant in the y-direction. Writing $q(x,z) = \Psi\sqrt{x}$ to isolate the geometric spreading effect, Eq. (1.33) becomes:

$$\left(\frac{\partial^2}{\partial x^2} + \frac{\partial^2}{\partial z^2} + k^2\right)q = 0. \tag{1.34}$$

The refractive index is assumed to vary weakly with distance so that variations in the k with respect to x are negligible over a computational step. The wavenumber k is then solely dependent on z. By introducing the operator $\mathcal{Q}^2 = \frac{\partial^2}{\partial z^2} + k^2(z)$ representing the dependence on z, and factoring the Eq. (1.34), it gives:

$$\left(\frac{\partial}{\partial x} + i\mathcal{Q}\right)\left(\frac{\partial}{\partial x} - i\mathcal{Q}\right)q = 0, \tag{1.35}$$

where the two factors represent the propagation in the positive and negative x directions respectively. A solution such as $q_s = \phi(x,z)e^{-i(k_0 x)}$ allows to solve this parabolic equation in the forward direction. The exponential term represents a 'carrier' wave and ϕ is a varying envelope in space, which modulates the carrier. Introducing q_s in the one-way version of Eq. (1.35) for the positive x direction leads to the WAPE formulation of the parabolic equation method:

$$\frac{\partial\phi}{\partial x} = i\left(1-\mathcal{Q}\right)\phi. \tag{1.36}$$

Numerous methods to solve this equation, even in its 3D form, are available and detailed in the literature, *e.g.* [31, 105, 104, 85]. However, it is a one-way equation that ignores back scattered propagation, making it hard to model inner forest sound fields. Its main advantages are its ability to take into account inhomogeneous media, complex terrain and long-range propagation.

PE applications to forests acoustics. Crank-Nicolson parabolic equation (CNPE [56]) and Green's function parabolic equation (GFPE [115]) have been used to model sound propagation through forests [121, 107]. Thus, the parabolic equation-based methods are well-suited when the atmospheric one-way sound field through and over the forest is of interest. Many studies use them, for example, to evaluate the noise reduction of tree belts [134, 9]. In the literature, the GFPE shows reasonable agreement with short-range measurements up to 4200 Hz [121]. Coupling this numerical method with the propagation in complex media theory [103] allows to model the drag effect of sound propagation through a forest quite accurately.

The main forest factors known to affect sound propagation are the canopy's microclimate, the multiple scattering by the trunks and stems and the ground absorption [121, 4]. Their effects are observable on the simulated sound pressure level field displayed on Fig. 1.4.

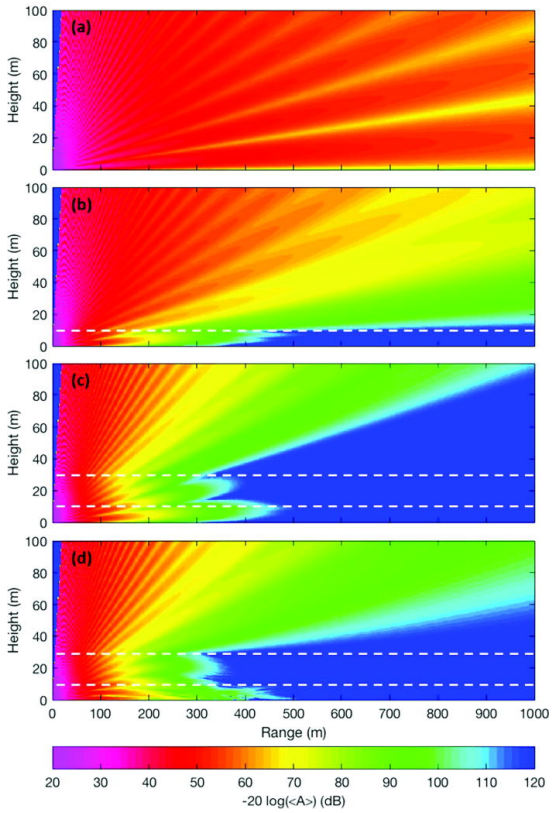

Figure 1.4. Complex amplitude of the mean sound pressure for different geometries of sound propagation: (a) a point source above an impedance ground in a homogeneous atmosphere; (b) a 10 m high trunk layer added to the previous case; (c) a 20 m high canopy layer added to the previous geometry; and (d) a downward-refracting atmosphere included within the trunk and canopy layers of the previous case. Dashed horizontal lines indicate the trunk and canopy layers. The modeling frequency is 2 kHz. Reproduced from [103], with the permission of the Acoustical Society of America.

It is important to remember that this realization does not take into account the backscattered field which is not integrated in the PE model. Consequently, it is not suitable for inner forest sound propagation modeling.

1.2.5 Time-domain discontinuous Galerkin (TD-DG) method

The nodal discontinuous Galerkin method theory is derived from the finite element method (FEM) theory, however, better suited to solve partial differential equations modeling wave

propagation. One of its advantages, common with FEM, is to use triangular (2D) or tetrahedral (3D) meshes, canceling the undesired effect of Cartesian meshes to privilege horizontal and vertical directions. The theory of the method is thoroughly detailed in the literature [132, 131]. It consists in developing a weak formulation of the LEE thanks to a projection on a well-chosen test basis function. To get a global overview, the LEE for a homogeneous and motionless medium are:

$$\frac{\partial \vec{v}}{\partial t} + \frac{1}{\rho}\vec{\nabla} p = \vec{0} \tag{1.37a}$$

$$\frac{\partial p}{\partial t} + \rho c^2 \vec{\nabla} \cdot \vec{v} = 0. \tag{1.37b}$$

Taking Eq. (1.37) as a starting point, the details about the spatial and time discretization are available in the literature [71]. The implementation of time-domain boundary conditions has been investigated and validated and Perfectly Matched Layers (PML) formulation has been written for this method [5, 45]. The specificities mentioned above make this method another potential candidate for modeling sound propagation inside forests.

Available open-sources codes.

- DGFEM-Acoustic. TD-DG method applied to the linearized Euler equations and the acoustic perturbation equations. The theory is also well described in the report associated with the code. Available on `https://github.com/povanberg/DGFEM-Acoustic`.
- Exasim. Project about DG and its use to solve PDEs in general. Available on `https://github.com/exapde/Exasim`.

1.2.6 Pseudo-spectral time domain methods (PSTD)

The concept of these methods is to approximate the spatial derivatives of Eq. (1.37) by projecting the functions to derive on a chosen basis of smooth functions [41]. The most common pseudo-spectral methods are called Fourier or Chebyshev according to the chosen function basis (Fourier transforms or Chebyshev polynomials respectively). An example is given below for the Fourier PSTD method:

$$p(x) \approx \sum_{n=0}^{N} U_n \exp\left(ik_n x\right), \tag{1.38}$$

with $k_n = -N/2 + n$ and the U_n well-chosen coefficients to approximate the function [41]. Approximating the derivative of this function at specific points x_j gives:

$$\frac{\partial p}{\partial x}(x_j) = \sum_{n=1}^{N-1} ik_n U_n \exp\left(ik_n x_j\right). \tag{1.39}$$

An extended formulation of this method has been used for modeling outdoor sound propagation, with a sound speed profile and a rigid ground, showing consistent agreement with an analytical solution and other numerical methods. The advantage of this method is that the spatial discretization method only requires two points per wavelength, making it computationally efficient [76].

However, for non-harmonic sources and medium discontinuities, Fourier PSTD shows problems of Gibbs oscillations [41]. In the context of modeling sound propagation in forests, this method has been used for modeling sound scattering by one tree [74]. One of the studied approaches consisted in modeling trees as air density inhomogeneities, which is consistent with

the sound in complex media theory presented in Section 1.1. Modeling an entire forest with this method could be investigated, even if it represents theoretical and computational challenges. An open-source example of this method implementation can be found in this repository [73]: https://github.com/openPSTD/openPSTD.

1.2.7 Transmission Line Matrix model

Historically, the method was used to model high-frequency electromagnetic fields and the proper name 'TLM' and the formalism used nowadays appeared only in 1971 [82, 81]. More recently, this method has been studied for outdoor sound propagation modeling application [61, 10], and some similarities with FDTD methods have been pointed out [72].

The TLM method's applicability to forests has been studied previously by applying it to arrangements of perfectly reflective cylinders above a perfectly reflective plane (and an impedance plane, only for one cylinder) up to 1000 Hz [26, 29, 28]. For these setups, it has been validated thanks to a comparison with measurements made on a scale model in a semi-anechoic room. Again, in the perspective of modeling outdoor sound propagation, the TLM method has also been validated thanks to comparisons to a FDTD reference code (sixth-order in space and fourth-order Runge-Kutta in time) in the case of impedance boundary conditions including ground with rugosity profiles [51].

The method presents inherent anisotropy (*i.e.* Cartesian grid effect) which, although being described in the literature [24], needs further investigation to quantify this effect on simulation results. Efforts to characterize the TLM method stability and numerical dispersion exist and mesh adaptations, as the "tetrahedral TLM" are available [94]. However, the tetrahedral TLM method is not a version of the method applied to unstructured tetrahedral meshes and therefore presents privileged directions as for a Cartesian mesh. Thus, for the author, the implementation complexity brought by the structured mesh modification is not worth the gain in accuracy. In Chapter 2, a thorough review of the method is proposed, oriented toward outdoor sound propagation in forests, from a numerical stability analysis perspective.

1.2.8 Qualitative comparison of presented methods

The synthetic overview proposed in Table 1.1 qualitatively compares the advantages and limitations of the methods for solving PDEs presented above. The analysis is made in terms of numerical costs, wave phenomena integration (denoted as "*wave-based*"), capacity to simulate in the time-domain, and *modularity*. The latter is proposed as a feature for numerical methods, as their "proximity" to the wave equation (or LEE) and the ease they present when an additional term needs to be added in the solved PDE to integrate an additional physical phenomenon.

	Ray-tracing	FDTD	PE	DG	PSTD	TLM
Numerical Costs	+++	−	+	+	++	−
Wave-based	−	+++	++	+++	+++	+++
Time-domain	− − −	+++	− (one-way)	+++	+++	+++
Modularity	+++	+++	+	+	−	−

Table 1.1. Summary of the advantages and limitations of numerical methods for modeling sound propagation in complex outdoor environments. + represents a degree of advantage and − a degree of limitation.

Finally, it is challenging to definitively state whether one method is the most suitable to model sound propagation within forests, as each method demonstrates strong performances in

modeling phenomena related to sound propagation. Hybrid solvers have thus been investigated as viable alternatives for tackling high-complexity scenarios, such as broadband frequency-domain modeling in 3D outdoor environments [130, 87]. In addition, properly benchmarking outdoor numerical methods represents a significant contribution to the research community, as it helps to choose between numerical methods according to the required simulation [75].

1.3 Sound propagation phenomena in lower atmosphere

1.3.1 Atmospheric absorption

An ISO standard has been developed to address sound attenuation during outdoor propagation [2, 78, 1]. In the case of wave-based models, the literature extensively covers the theory of sound attenuation [13, 12, 112]. To enhance the clarity of this document, this section provides a few details about this phenomenon and its underlying principles.

The classical description of atmospheric attenuation is based on the introduction of an exponential decay of the sound wave amplitudes as a function of the propagation distance, such as:

$$|p(x)| = |p(0)|\, e^{-\alpha_{\text{atm}} x}, \tag{1.40}$$

with α_{atm} a frequency-dependent coefficient, accounting for the heat conduction, the shear viscosity and the molecular relaxation in the air. It also depends on the air humidity, temperature and pressure [112]. To get an idea of the phenomenon magnitude in the lower atmosphere, with 70% of humidity, at 20°C and a frequency of 1000 Hz, $\alpha_{\text{dB}} \approx 8.686\alpha_{\text{atm}} \approx 0.005$ dB.m^{-1}.

1.3.2 Dynamic micrometeorological effects

Within the surface layer - the lower part of the meteorological boundary layer - vertical sound velocity gradients lead to refraction effects that change the way sound propagates. [115, 112, 8]. This effect on the sound speed is directly related to vertical gradients of temperature and wind speed, which are micrometeorological factors ruled mostly by the day/night and seasonal cycles. Under a forest canopy, these gradients are known to be smoothed and can be neglected [26, 128, 50]. Thus, they are described very briefly in this section.

To introduce these meteorological effects, a parallel to optical refraction is usually made, since the vertical variation of sound speed can be assimilated as a stratified atmosphere with different layers, each characterized by an acoustic refraction index n such as:

$$n = \frac{c(z)}{c_0} \tag{1.41}$$

where c_0 is a reference sound speed and $c(z)$ the sound speed as a function of altitude. The refraction effect can then be explained using the Snell-Descartes law and the geometrical acoustic analogy. In the following, only two typical cases of atmospheric conditions are presented, since the phenomena governing the sound velocity in the surface layer are stochastic and thus time-varying and complex.

Downward conditions. In this case, the wind is favorable to the sound propagation direction and/or the vertical gradient of temperature is positive. Thus, the refraction index n increases with the altitude, and the acoustic rays are bent toward the ground, resulting in additional sound energy in the surface layer. In addition, interferences can appear between the direct field, the ground reflection and the refracted field. Fig. 1.4 shows an example of a simulation including such conditions, using the GFPE method.

Upward conditions. Contrary to the previous example, the wind is unfavorable to the sound propagation direction and/or the vertical gradient of temperature is negative. $c(z)$, hence n increase with altitude and the acoustic rays are refracted away from the ground, sometimes leading to shadow zones.

Other meteorological phenomena that occur in the lower atmosphere are turbulent eddies. Indeed, the wind is not always a laminar flow and whirls appear in the surface layer. They tend to mitigate the refraction effect and smooth the interferences between waves [115, 8].

1.3.3 Foliage attenuation

Data about foliage attenuation mostly comes from experimental studies [26]. Even so, an approximation is detailed in the ISO-9613-2:1996 [78] for engineering frequency methods and the relative methodology to take it into account can be found in [80]. According to the literature entry [26], foliage is shown to have a significant influence and emit sounds around 4000 Hz, which is consistent with a wavelength of ≈ 8.6 cm, the order of magnitude of a leaf size [35].

In Sections 1.1.6 and 1.2.4 a theoretical model that has been proposed for stems and leaves has been presented. It would be interesting to apply this theory at a smaller scale to assimilate volumes filled by vegetation to homogenized domains characterized by effective values of density and sound speed $(\rho_{\text{eff}}, c_{\text{eff}})$ calculated from statistical data.

As mentioned in various studies, the key factor to consider when modeling sound propagation in forests is the ground effect [121, 9]. Therefore, special attention is dedicated to this phenomenon, which is described by boundary conditions in numerical methods.

1.4 Boundary conditions

In this section, the theoretical and general case of an acoustic boundary condition is addressed. Fig. 1.5 schematizes the considered problem and places it in a 3D coordinate system. For now, vectors will also be denoted with an *underbar* (*i.e:* $\underline{\mathrm{r}}$) for the readability of the equations.

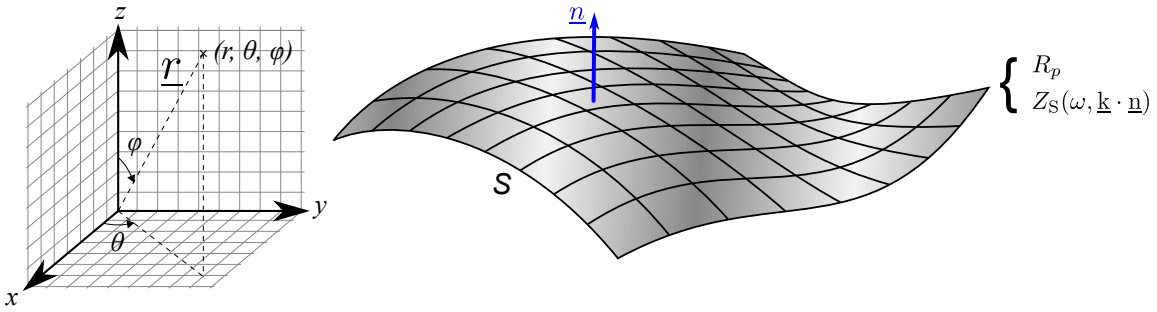

Figure 1.5. Scheme of a boundary with surface equation $\mathfrak{s}(\underline{\mathrm{r}}) = 0$ having either a pressure reflection coefficient or an impedance value.

1.4.1 Pressure reflection coefficient

The sound pressure reflection coefficient of a plane wave, generally referred to as R_p, is an amplitude ratio that quantifies the fraction of incident pressure reflected at an interface between two media. It is a function of the angle of incidence of the plane wave and the impedances of the media. Using this coefficient to describe reflections is convenient as it only implies a product, but it is limited as it is not frequency-dependent. R_p is commonly used and widely detailed in the literature [115, 112], therefore the present study emphasizes on frequency-dependent acoustic impedance boundary conditions and their integration in time-domain numerical methods.

1.4.2 Acoustic impedance condition

For a boundary condition described by a surface equation $\mathcal{s}(\underline{\mathrm{r}}) = 0$ and governed by an impedance relation, the physical behavior of acoustic waves at the fluid-material interface is described by a frequency-dependent relation. This boundary condition, valid in the plane wave approximation, is written as:

$$\hat{p}(\omega, \underline{\mathrm{k}}, \mathcal{s}(\underline{\mathrm{r}}) = 0) = Z_{\mathrm{S}}(\omega, \underline{\mathrm{k}} \cdot \underline{\mathrm{n}}) \hat{v}_n(\omega, \underline{\mathrm{k}}, \mathcal{s}(\underline{\mathrm{r}}) = 0), \tag{1.42}$$

where Z_S, the surface impedance, describes the internal acoustic behavior of the modeled material, $\hat{p}$ and $\hat{v_n}$ represent the Fourier transform of the pressure and the particle velocity normal to the boundary, respectively. Using this relation in numerical methods is valid, as long as the spatial discretization of the boundary is considered small compared to the minimal modeled wavelength ($\Delta\ell \ll \lambda_{\min}$). Note that the use of a capital letter for impedance is not due to a numerical approximation, but rather follows the usual convention. Furthermore, reference [37] justifies that within the framework of the local approximation, Eq. (1.42) does not depend on the incidence angle of the plane wave, and therefore on $\underline{\mathrm{k}}$.

The acoustic impedance is expressed as a complex number and can be decomposed as follows:

$$Z_{\mathrm{S}}(\omega) = X(\omega) + iY(\omega). \tag{1.43}$$

The resistive real part $X(\omega)$ represents the radiative and thermo-viscous mechanisms in the boundary medium, while $Y(\omega)$ translates the elastic and inertial behavior inside of it. The issue with impedance models in time-domain numerical schemes arises from the transformation of Eq. (1.42) into the time domain, which involves a convolution product:

$$p(t, \mathcal{s}(\underline{\mathrm{r}}) = 0) = z_{\mathrm{S}}(t) * v_n(t, \mathcal{s}(\underline{\mathrm{r}}) = 0) = \int_{-\infty}^{+\infty} z_{\mathrm{S}}(t - t') v_n(t', \mathcal{s}(\underline{\mathrm{r}}) = 0) dt', \tag{1.44}$$

where $p(t, \mathcal{s}(\underline{\mathrm{r}}) = 0)$ and $z_{\mathrm{S}}(t)$ are the inverse Fourier transform of $\hat{p}(\omega, \mathcal{s}(\underline{\mathrm{r}}) = 0)$ and $Z_{\mathrm{S}}(\omega)$, respectively. For the pressure, it is defined as:

$$p(t, \underline{\mathrm{r}}) = \frac{1}{2\pi} \int_{-\infty}^{+\infty} \hat{p}(\omega, \underline{\mathrm{r}}) e^{-i\omega t} d\omega. \tag{1.45}$$

Within the scope of time-domain numerical methods, the numerical computation of this convolution product would require storing v_n at all time steps, which is costly in terms of computational resources. Therefore, approximate formulations of this convolution product have been proposed for its computation, such as the recursive convolution method [37]. However, it is necessary to verify that the impedance formulation is physically admissible. For this purpose, three conditions are mandatory [37, 110, 95]:

- **Reality**: p and v_n are real quantities, Eq. (1.44) implies that $z_{\mathrm{S}}(t)$ must be real, thus $Z_{\mathrm{S}}^*(\omega) = Z_{\mathrm{S}}(-\omega)$.
- **Passivity**: the intensity through the boundary $I = \mathrm{Re}(Z_{\mathrm{S}}(\omega)) \left|\hat{v_n}\right|^2 / 2$ must be greater or equal to zero: $\mathrm{Re}(Z_{\mathrm{S}}(\omega)) \geq 0$.
- **Causality**: Eq. (1.44) implies that $p(t, \mathcal{s}(\underline{\mathrm{r}}) = 0)$ can not be defined for $t' > t$. $Z(\omega)$ must then be an analytical function in $\mathrm{Im}(\omega) \geq 0$, $|Z_{\mathrm{S}}|$ must be square-integrable on ω and $\exists t_0$ as $Z_{\mathrm{S}}(\omega) e^{-\mathrm{i}t_0} \to 0$ for $|\omega| \to \infty$ in $\mathrm{Im}(\omega) \geq 0$.

Reminding that in the complex settings, analytical functions are the functions that are complex-differentiable at every point.

1.4.3 Recursive convolution

The recursive convolution method [109], allows bypassing the computation of the integral (1.44) by approximating $Z(\omega)$ up to order M. Z_{S}^{M} can then be written as a sum of N first-order functions and T second-order functions [37]:

$$Z_{\mathrm{S}}(\omega) \approx Z_{\mathrm{S}}^{M}(\omega) = Z_{\mathrm{S}}^{\infty} + \sum_{k=1}^{K} Z_k(\omega) + \sum_{l=1}^{T} Z_l(\omega), \tag{1.46}$$

where $M = K + 2T$. The first and second-order functions, as well as their inverse Fourier transforms, are given by:

$$\begin{cases} Z_k(\omega) &= \frac{A_k}{\lambda_k - i\omega}, \\ z_k(t) &= A_k e^{-\lambda_k t} H(t), \end{cases} \qquad \lambda_k \geq 0 \tag{1.47a}$$

$$\begin{cases} Z_l(\omega) &= \frac{A_l}{\lambda_l - i\omega} + \frac{A_l^*}{\lambda_l^* - i\omega} = \frac{B_l + iC_l}{\alpha_l + i\beta_l - i\omega} + \frac{B_l - iC_l}{\alpha_l - i\beta_l - i\omega}, \\ z_l(t) &= 2\left[B_l \cos(\beta_l t) + C_l \sin(\beta_l t)\right] e^{-\alpha_l t} H(t), \end{cases} \qquad \alpha_l \geq 0. \tag{1.47b}$$

λ and A are usually referred to as poles and coefficients, respectively. $\mathrm{Re}(\lambda) \geq 0$ is mandatory to satisfy the causality condition and the reality condition is fulfilled since both A and λ are either real or complex conjugates (denoted *). Furthermore, according to Eq. (1.44), $z_{\mathrm{S}}(t)$ can be interpreted as the impulse response of the boundary medium to be modeled, and its approximation $z_{\mathrm{S}}^{M}(t)$ can be written as:

$$z_{\mathrm{S}}(t)^{M} = Z_{\mathrm{S}}^{\infty}\delta(t) + \sum_{k=1}^{K} z_k(t) + \sum_{l=1}^{T} z_l(t). \tag{1.48}$$

It is possible to interpret the physical meaning of this impulse response: the zeroth-order term corresponds to the instantaneous reaction of the boundary medium, the first-order term represents a relaxation with exponential decay, and the second-order term is associated with the behavior of a damped oscillator. Then, by inserting Eq. (1.48) into Eq. (1.44), the time-domain impedance boundary condition becomes:

$$p(t, \mathfrak{s}(\underline{\mathrm{r}}) = 0) = Z_{\mathrm{S}}^{\infty} v_n(t, \mathfrak{s}(\underline{\mathrm{r}}) = 0) + \int_{-\infty}^{+\infty} \left(\sum_{k=1}^{K} z_k(t - t') + \sum_{l=1}^{T} z_l(t - t') \right) v_n(t', \mathfrak{s}(\underline{\mathrm{r}}) = 0) dt'. \tag{1.49}$$

Substituting Eq. (1.47a) in Eq. (1.49) leads to:

$$p(t, \mathfrak{s}(\underline{\mathrm{r}}) = 0) = Z_{\mathrm{S}}^{\infty} v_n(t, \mathfrak{s}(\underline{\mathrm{r}}) = 0) + \sum_{k=1}^{K} A_k \psi_k(t) + \sum_{l=1}^{T} 2\left[B_l \psi_l^{(1)}(t) + C_l \psi_l^{(2)}(t)\right], \tag{1.50}$$

defining $\psi_l = \psi_l^{(1)} + i\psi_l^{(2)}$ to introduce the concept of accumulators in the time domain:

$$\psi_k(t) = \int_{-\infty}^{+\infty} v_n(t', \mathfrak{s}(\underline{\mathrm{r}}) = 0) e^{-\lambda_k (t - t')} \, dt', \tag{1.51a}$$

$$\psi_l^{(1)}(t) = \int_{-\infty}^{+\infty} v_n(t', \mathfrak{s}(\underline{\mathrm{r}}) = 0) e^{-\alpha_l (t - t')} \cos\left(\beta_l (t - t')\right) \, dt', \tag{1.51b}$$

$$\psi_l^{(2)}(t) = \int_{-\infty}^{+\infty} v_n(t', \mathfrak{s}(\underline{\mathrm{r}}) = 0) e^{-\alpha_l (t - t')} \sin\left(\beta_l (t - t')\right) \, dt'. \tag{1.51c}$$

Differentiating equations Eq. (1.51), leads to first-order differential equations. Solving them using a numerical scheme is a way of performing the convolution product known as the *auxiliary differential equation* (ADE) method [38, 126]. For recursive convolution methods, two approaches are commonly found in the literature for formulating these methods [109, 38]. The more direct approach [38] involves discretizing one of the equations (Eq. (1.51a) is taken as an example) and integrating it over a time step to obtain:

$$ {}_{n+1}\psi_k = e^{-\lambda_k \Delta t}\, {}_n\psi_k + e^{-\lambda_k \Delta t} \int_0^{\Delta t} e^{-\lambda_k t'} v_n(t' + n\Delta t, \jmath(\underline{\mathrm{r}}) = 0) dt'. \tag{1.52} $$

The hypothesis of a constant normal particle velocity over a time step:

$$ v_n(t' + n\Delta t, \jmath(\underline{\mathrm{r}}) = 0) = {}_{n+1}V_b, \tag{1.53} $$

leads to the method *Piecewise Constant Recursive Convolution* (PCRC). The discretized accumulators are then:

$$ {}_n\psi_k = {}_nV_b \frac{1 - e^{-\lambda_k \Delta t}}{\lambda_k} + {}_{n-1}\psi_k e^{-\lambda_k \Delta t}, \tag{1.54} $$

$$ {}_n\psi_l = {}_nV_b \frac{1 - e^{-(\alpha_l - i\beta_l)\Delta t}}{\alpha_l - i\beta_l} + {}_{n-1}\psi_l e^{-(\alpha_l - i\beta_l)\Delta t}. \tag{1.55} $$

The discretized Eq. (1.50) then becomes:

$$ {}_nP_b = Z_{\mathrm{S}}^{\infty}\, {}_nV_b + \sum_{k=1}^{K} {}_n\psi_k A_k + 2 \sum_{l=1}^{T} \left[B_l \mathrm{Re}({}_n\psi_l) + C_l \mathrm{Im}({}_n\psi_l) \right]. \tag{1.56} $$

Depending on the boundary position, subscript b can take the following values:

- $b = \left(j_1 \pm \frac{1}{2}, j_2, j_3\right)$: boundary orthogonal to $\vec{x}_1$-axis.
- $b = \left(j_1, j_2 \pm \frac{1}{2}, j_3\right)$: boundary orthogonal to $\vec{x}_2$-axis.
- $b = \left(j_1, j_2, j_3 \pm \frac{1}{2}\right)$: boundary orthogonal to $\vec{x}_3$-axis.

However, the PCRC method is only first-order accurate in time [38]. Then, using a first-order Taylor-Young decomposition, a linear approximation of the particle velocity can be written:

$$ v_n(t' + n\Delta t, \jmath(\underline{\mathrm{r}}) = 0) = {}_{n+1}V_b + \frac{{}_{n+1}V_b - {}_nV_b}{\Delta t}(t' - \Delta t). \tag{1.57} $$

It is called *Piecewise Linear Recursive Convolution* and leads to the following discretization of the accumulators:

$$ {}_n\psi_k = {}_nV_b \frac{1 - e^{-\lambda_k \Delta t}}{\lambda_k} + ({}_{n-1}V_b - {}_nV_b) \frac{1 + e^{-\lambda_k \Delta t}(-\lambda_k \Delta t - 1)}{\lambda_k^2 \Delta t} + {}_{n-1}\psi_k e^{-\lambda_k \Delta t}, \tag{1.58} $$

$$ {}_n\psi_l = {}_nV_b \frac{1 - e^{-\lambda_l^* \Delta t}}{\lambda_l^*} + ({}_{n-1}V_b - {}_nV_b) \frac{1 + e^{-\lambda_l^* \Delta t}(-\lambda_l^* \Delta t - 1)}{(\lambda_l^*)^2 \Delta t} + {}_{n-1}\psi_k e^{-\lambda_l^* \Delta t}. \tag{1.59} $$

These formulations are ready to be adapted at the boundaries of a given numerical method. However, $Z(\omega)$ the value approximated by $Z_{\mathrm{S}}^{\mathrm{M}}$ is yet to be determined.

1.4.4 Impedance models for forest grounds and barks

As briefly mentioned in the previous section, acoustic impedance models can be used to characterize the internal behavior of a material without having to explicitly model the sound propagation within the solid. To do this, it is useful to know the physical parameters of materials, since measuring their impedance in situ in an outdoor environment can be technically difficult [62]. However, materials as complex as soil or tree bark can be characterized by numerous parameters, depending on the precision required. The most commonly used parameters are introduced below:

- σ_0, the airflow resistivity, commonly expressed in $kPa.s.m^{-2}$ is linked to Darcy's law, which characterizes the flow in a porous medium;
- $\Omega = \dfrac{V_{\text{air}}}{V_{\text{sample}}}$, the material porosity, $\in [0, 1]$. With V_{air} the air volume within V_{sample} the material volume;
- $q = \dfrac{1}{\cos(\phi)}$, the material tortuosity, with ϕ the angle of inclination of the pores with respect to the normal to the material surface;
- $\text{Pr} = \dfrac{\nu}{\alpha_{\text{th}}}$, the Prandtl number, with ν the kinematic viscosity and α_{th} the thermal diffusivity.
- $\gamma = \dfrac{C_p}{C_v}$, the ratio of thermal mass capacities.

1.4.4.a Non-exhaustive listing of models

Two cases are generally considered [6, 39], with their respective formulation of the surface impedance $Z_{\text{S}}(\omega)$:

- semi-infinite formulation:
$$Z_{\text{S},\infty} = Z_c, \tag{1.60}$$
with Z_c the characteristic impedance of the medium.
- formulation for a material layer on an infinite rigidly backed layer:
$$Z_{\text{S},e} = Z_c \coth(-\text{i}k_c e), \tag{1.61}$$
with k_c the wave number in the medium and e [m] the thickness of the layer placed on a semi-infinite rigid support.

More complex models than those expressed above exist, such as multi-layered materials, but they are limited by soil characterization capabilities in outdoor environments. Following these definitions, it is necessary to specify that a fourth admissibility condition [88] must be added to the ones stated in Eq. (1.4.2) for each impedance model. The complex effective density of a medium described by an impedance condition is defined as:

$$\rho'(\omega) = \frac{Z_c k_c}{\omega}. \tag{1.62}$$

For the impedance to be physically admissible, the natural condition $\text{Re}(\rho') \geq 0$ for $\omega > 0$ must be respected. Beyond the consideration of a single layer or infinite scenario, a variety of formulations for the parameters k_c and Z_c are available [6], and three different model families are presented hereafter.

1.4.4.b Square-root impedance models

Some existing impedance models can be formulated as a product of square-root functions:

$$Z_c = \alpha \frac{\rho_0 c_0 q}{\Omega} \left(1 + \frac{\omega_1}{-i\omega}\right)^{1/2} \left(1 + \frac{\omega_2}{-i\omega}\right)^{1/2} \left(1 + \frac{\omega_3}{-i\omega}\right)^{-1/2} = \alpha \frac{\rho_0 c_0 q}{\Omega} \left[\frac{(\omega_1 - iw)(\omega_2 - iw)}{-i\omega(\omega_3 - iw)}\right]^{1/2}, \tag{1.63a}$$

$$k_c = \beta \frac{\omega q}{c_0} \left(1 + \frac{\omega_1}{-i\omega}\right)^{1/2} \left(1 + \frac{\omega_2}{-i\omega}\right)^{-1/2} \left(1 + \frac{\omega_3}{-i\omega}\right)^{1/2} = \beta \frac{\omega q}{c_0} \left[\frac{(\omega_1 - iw)(\omega_3 - iw)}{-i\omega(\omega_2 - iw)}\right]^{1/2}, \tag{1.63b}$$

with α, β, ω_1, ω_2, $\omega_3 \in \mathbb{R}^+$. These parameters are detailed in Table 1.2 for different models and are specific to the materials they model [39].

Impedance model	α	β	ω_1	ω_2	ω_3
Zwikker & Kosten [137]	1	1	$\sigma_0\Omega/(\rho_0 q^2)$	0	0
Modified Zwikker & Kosten [101]	1	$\emptyset$	$\sigma_0\Omega/(\rho_0 q^2\gamma^2)$	0	0
Taraldsen & Jonasson [123]	$\gamma^{-1/2}$	$\gamma^{1/2}$	$\sigma_0\Omega/(\rho_0 q^2)$	0	0
Hamet & Bérengier [16]	1	1	$\sigma_0\Omega/(\rho_0 q^2\gamma^2)$	$\gamma\sigma_0/(\rho_0 \mathrm{Pr})$	$\sigma_0/(\rho_0 \mathrm{Pr})$

Table 1.2. Parameters α,β, ω_1, ω_2 and ω_3 for different square-root models. The input parameter σ_0 is expressed in [Pa.s.m^{-2}] here.

1.4.4.c Polynomial impedance models

Polynomial-type models are the most used as they enable the characterization of material impedance with a reduced number of parameters. However, they imply the use of a more simplifying hypothesis, namely that of materials whose porosity is close to 1 (*i.e.* very porous materials). The general formulation of these models is written:

$$Z_c = \rho_0 c_0 \left[1 + a\left(\frac{\sigma}{\rho_0\omega}\right)^b + \mathrm{i}c\left(\frac{\sigma}{\rho_0\omega}\right)^d\right], \tag{1.64a}$$

$$k_c = \frac{\omega}{c_0}\left[1 + p\left(\frac{\sigma}{\rho_0\omega}\right)^q + \mathrm{i}r\left(\frac{\sigma}{\rho_0\omega}\right)^s\right], \tag{1.64b}$$

with a, b, c, d, p, q, r, $s \in \mathbb{R}^+$. These parameters are detailed in Table 1.3 and are specific to the materials they model.

Impedance model	a	c	b	d	p	r	q	s
Delany & Bazley [34]	0.232	0.336	0.75	0.73	0.353	0.576	0.70	0.59
Miki [93]	0.251	0.384	0.632		0.380	0.557	0.618	
Modified Miki [39]	0.251	0.384	0.632		0.351	0.539	0.632	

Table 1.3. Coefficients a, b, c, d, p, q, r, s for different polynomial models, with $\rho_0 = 1.2$ kg.m^{-3}.

According to the literature [38, 88], the usage of such models within the framework of time-domain numerical methods is not recommended as the Delany & Bazley model can not

be both causal and real [39]. Moreover, for an infinite rigidly-backed layer, this family of models is inadvisable as they allow the writing of complex effective density whose real part is negative [88, 38].

1.4.4.d Slit-pore model

The Slit-pore model has been reformulated and studied for modeling forest ground impedance conditions [38]. It is derived from the 'identical tortuous pore' analytical model in the case where the pores are considered identical parallel slits [6]. Under this hypothesis, k_c and Z_c can be written:

$$Z_c = Z_\infty \left[f_1\left(\sqrt{\frac{-\mathrm{i}\omega}{\omega_1}}\right) f_2\left(\sqrt{\frac{-\mathrm{i}\omega}{\omega_2}}\right)\right]^{-1/2}, \tag{1.65a}$$

$$k_c = \frac{\omega}{c_0}\sqrt{q}\left[f_2\left(\sqrt{\frac{-\mathrm{i}\omega}{\omega_2}}\right) \Big/ f_1\left(\sqrt{\frac{-\mathrm{i}\omega}{\omega_1}}\right)\right]^{1/2}, \tag{1.65b}$$

where f_1 and f_2 stand for the functions:

$$f_1(z) = 1 - \frac{\tanh(z)}{z},\ z \in \mathbb{C}, \tag{1.66a}$$

$$f_2(z) = 1 + (\gamma - 1)\frac{\tanh(z)}{z},\ z \in \mathbb{C}. \tag{1.66b}$$

Additional simplifications, $Z_\infty = \dfrac{\rho_0 c_0 \sqrt{q}}{\Omega}$, $\omega_1 = \dfrac{\Omega\sigma}{3\rho_0 q}$ and $\omega_2 = \dfrac{\Omega\sigma}{3\rho_0 q \mathrm{Pr}}$, lead to a model which takes three input parameters: Ω, σ and q. At last, taking $q = \dfrac{1}{\sqrt{\Omega}}$ enables reducing the number of input parameters to only two. This version of the model is used throughout this doctoral work and will be referred to as TWO-PARAMETER SLIT-PORE MODEL. Comparisons between numerical results and measurements [6, 38] have demonstrated that this model is the most reliable to describe forest grounds. Reducing the number of input parameters required improves the practicality of the model since in-situ measurements of these parameters are difficult (space and time variability, metrological and meteorological uncertainties).

1.4.5 Perfectly (or Adapted) Matched Layer - PML

To simulate an 'open' boundary in numerical methods, an absorbing layer or PML (*Perfectly Matched Layer*) is commonly used. Usually, this is an alternative to enlarging the computational domain to optimize numerical cost. This technique consists in modifying the equations solved at the edge of the computational domain to simulate a transformation of the incident wave into an evanescent wave, without introducing an impedance break. A sudden break in impedance would result in the generation of spurious reflected waves (case $R_p = 0$).

The formulation of these layers for the TLM model is addressed in Chapter 2.

1.5 Chapter summary

This chapter presented a literature review of some analytical and numerical methods for modeling outdoor sound propagation. A particular emphasis has been placed on providing an overview of the underlying theory for each modeling technique to enable readers to grasp the principles and originalities of each method. The chapter discussed the effective wavenumber method and showed its application within the parabolic equation method applied to forest environments. An adaptation of this model to time-domain methods would be promising to integrate homogenized "stems-foliage" environments in simulations. A comparative table of the mentioned numerical methods has been provided, leading to the conclusion that hybrid solvers, including coupled methods, hold promise for adapting to complex scenarios. Finally, this chapter focused on boundary conditions and impedance models, providing a detailed explanation of the necessary theoretical foundations for implementation and demonstrating the diverse formulations available in the literature.

In the subsequent chapter, the study will investigate the applicability of the Transmission Line Matrix (TLM) method for modeling sound propagation in forest environments. This time-domain method, previously employed at the UMRAE laboratory and anticipated for forest modeling in a prior Ph.D. thesis [27], will be further investigated. Indeed, this method allows the simulation of long-range sound propagation phenomena in complex 3D geometries, including frequency-dependent boundary conditions, making it a legitimate candidate for exploring forest acoustic modeling.

Chapter 2

Transmission Line Matrix model (TLM)

This chapter focuses on the transmission line matrix model (TLM), a method implemented and used by the UMRAE laboratory over the last decades [66, 60, 67, 61, 63, 10, 27, 28]. As introduced in Section 1.2.7, the applicability of the method to different cases has been assessed, and this chapter aims to pursue this approach toward modeling sound propagation in long-distance forest scenarios. Indeed, considering the possibility of simulating birdsongs in hundreds of meters of forest implies computing a high ratio of distance to the minimum acoustic wavelength (distance/$\lambda_{\min}$).

To this end, the general formalism of the method is reviewed, and new formulations are introduced to perform stability analyses. The approach is then applied to homogeneous non-dissipative and inhomogeneous dissipative media. Finally, the source definition and boundary conditions are theoretically challenged and partially renewed compared to previous TLM formulations.

Throughout the chapter, newly introduced or adapted formulas will be indicated by underlined equation numbers for ease of reading, *e.g.* ($\underline{4.2^*}$).

2.1 Overall formalism

Unlike most numerical methods, the TLM is not initially derived from the conservative first-order equations. It is based on the Huygens-Fresnel principle for wave propagation and on an electro-acoustical analogy [83]. The property of a wavefront to be recursively discretizable in the form of punctual secondary sources is exploited and applied to a Cartesian mesh. The sound propagation is then modeled as pressure pulses propagating along transmission lines. Fig. 2.1 illustrates the application of the Huygens-Fresnel principle in a single point source case for one time step. This decomposition of the propagation mechanism is the TLM basis. It allows the analogy between the progression of a sound wave and the diffusion of acoustic pressure pulses between the nodes of a mesh.

In the following, a d-dimension spatial generalization inspired by previous works is described [61]. The spatial locations of nodes on the grid are then represented by the vector of indices: $\mathbf{r} = (j_1, \ldots, j_d)$. The core of the model is that each node in the volume under consideration receives and emits incident and scattered pulses instantaneously and simultaneously, at each time step n. These pressure pulses are traveling along links between the nodes, named transmission lines m. The formalism for this representation is given as follows: ${}_nI^m_{\mathbf{r}}$ represents the incident pressure pulse to the node $\mathbf{r}$ along line m at time step n, while ${}_nS^m_{\mathbf{r}}$ denotes the instantaneously scattered pulse along its corresponding line m. Fig. 2.1b represents these mechanisms in the 2D case of an incident pulse to a node from a single transmission line.

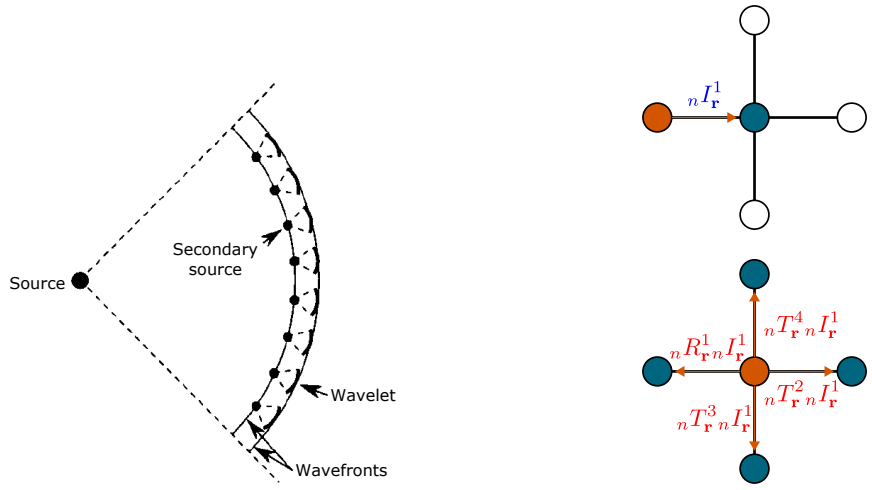

Figure 2.1. (a) Illustration of Huygens-Fresnel principle. (b) Simplified case: Huygens-Fresnel principle applied to a Cartesian mesh at the same time step (top: incident pulse, bottom: scattered pulses).

2.2 Scattering matrix

Expressing this mechanism in d dimensions leads to the main asset of the TLM method: the scattered pulses are calculated only with the matrix relation:

$$_n\underline{\mathrm{S}}_{\mathbf{r}} = {}_n\underline{\underline{D}}_{\mathbf{r}} \cdot {}_n\underline{\mathrm{I}}_{\mathbf{r}}, \tag{2.1}$$

with $_n\underline{\mathrm{S}}_{\mathbf{r}}$ and $_n\underline{\mathrm{I}}_{\mathbf{r}}$ the scattered and incident pulses vectors and $_n\underline{\underline{D}}_{\mathbf{r}}$ the $M \times M$ diffusion matrix:

$$_n\underline{\underline{D}}_{\mathbf{r}} = {}_n\begin{bmatrix} R^1_{\mathbf{r}} & T^2_{\mathbf{r}} & \cdots & \cdots & T^M_{\mathbf{r}} \\ T^1_{\mathbf{r}} & R^2_{\mathbf{r}} & T^m_{\mathbf{r}} & \cdots & \vdots \\ \vdots & T^2_{\mathbf{r}} & \ddots & T^m_{\mathbf{r}} & \vdots \\ \vdots & \vdots & T^m_{\mathbf{r}} & R^m_{\mathbf{r}} & T^M_{\mathbf{r}} \\ T^1_{\mathbf{r}} & \cdots & \cdots & T^m_{\mathbf{r}} & R^M_{\mathbf{r}} \end{bmatrix}_{\mathbf{r}}, \tag{2.2}$$

with $m \in \{1, \ldots, M\}$, M being the number of lines around a node. The matrix is populated with the pressure reflection and transmission coefficients, representing the behavior of pressure pulses encountering impedance discontinuities at a node, leading to reflections in the incident transmission lines and 'scattering' in the others, whose impedance values are formulated as $Z^m_{L_{\mathbf{r}}}$. $Z^m_{T_{\mathbf{r}}}$ is the acoustic impedance of the equivalent medium after the node discontinuity, as illustrated by Fig. 2.2. The general expressions of the coefficients are [33, 60]:

$$R_{\mathbf{r}}^m = \frac{Z_{T_\mathbf{r}}^m - Z_{L_\mathbf{r}}^m}{Z_{T_\mathbf{r}}^m + Z_{L_\mathbf{r}}^m}, \tag{2.3a}$$

$$T_{\mathbf{r}}^m = 1 + R_{\mathbf{r}}^m. \tag{2.3b}$$

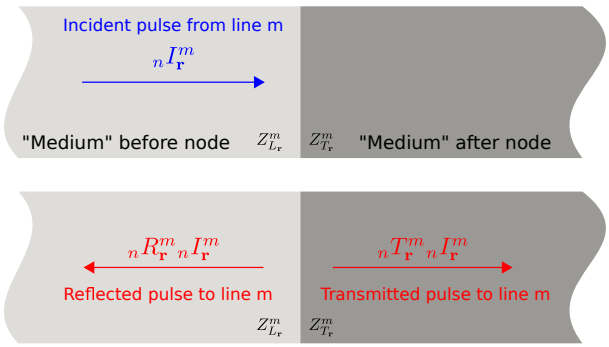

Figure 2.2. Phenomenological representation of an incident pulse reaching a node as a medium discontinuity. $R_\mathbf{r}^m$ and $T_\mathbf{r}^m$ are the reflection and transmission coefficients, respectively.

2.3 Connection laws

To complete the method, connection laws describing the temporal relation between the scattered pulses at instant t_n and incident pulses at instant t_{n+1} are needed. A d-dimension generalization of these laws can be written as:

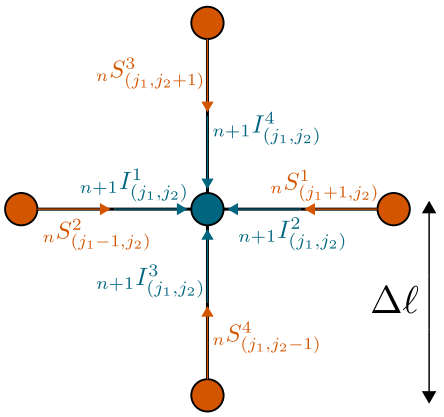

$$\text{for } k \in \{1,\dots,d\}\text{:} \quad \begin{cases} {}_{n+1}I^{2k-1}_{(j_1,\dots,j_d)} = {}_nS^{2k}_{(j_1-\delta_{k1},\dots,j_d-\delta_{kd})} \\ {}_{n+1}I^{2k}_{(j_1,\dots,j_d)} = {}_nS^{2k-1}_{(j_1+\delta_{k1},\dots,j_d+\delta_{kd})}. \end{cases} \tag{1*}$$

Figure 2.3. Representation of the 2D connection laws at the local node $\vec{r} = (j_1,\ j_2)$. Scattered pulses 'S' (orange) at time step n become incident pulses 'I' (blue) at step $n+1$. Δ_ℓ is the length between two nodes of the mesh grid.

The δ symbol is used here as the Kronecker delta[1]. A 2D example of these laws is illustrated by Fig. 2.3. They can also be expressed under the following form, by changing the indexes:

$$\text{for } k \in \{1,\dots,d\}\text{:} \quad \begin{cases} {}_nI^{2k-1}_{(j_1+\delta_{k1},\dots,j_d+\delta_{kd})} = {}_{n-1}S^{2k}_{(j_1,\dots,j_d)} \\ {}_nI^{2k}_{(j_1-\delta_{k1},\dots,j_d-\delta_{kd})} = {}_{n-1}S^{2k-1}_{(j_1,\dots,j_d)}, \end{cases} \tag{2*}$$

Eqs. (2.1) to (2*) are essential to describe and implement the TLM model. The link between them and the wave equation will be demonstrated in Section 2.4.1 and Section 2.5.4 in order to legitimize the resolution method. To do so, a general expression of Eq. (2.1) for each line is needed:

$$_nS_\mathbf{r}^m = {}_nR_\mathbf{r}^m\ {}_nI_\mathbf{r}^m + \sum_{m=1}^{M} {}_nT_\mathbf{r}^m\ {}_nI_\mathbf{r}^m - T_\mathbf{r}^m\ {}_nI_\mathbf{r}^m,\ m \in \{1,\dots,M\}.$$

[1] $\delta_{ij} = 0$ for $i \neq j$ and $\delta_{ij} = 1$ for $i = j$

Introducing the discrete pressure at the nodes as the sum of the neighboring nodes' contributions: ${}_nP_{\mathbf{r}} = \sum_{m=1}^{M} T_{\mathbf{r}}^m {}_nI_{\mathbf{r}}^m$ leads to:

$$ {}_n S_{\mathbf{r}}^m = {}_nP_{\mathbf{r}} - {}_nI_{\mathbf{r}}^m, \ \forall m \ \in \{1, \dots, M\}. \tag{2.5} $$

The following sections detail the numerical scheme for homogeneous and inhomogeneous media and show that Eq. (2.5) and the discrete pressure expression are valid in both cases.

2.4 Scheme for homogeneous non-dissipative media

This version of the model has been validated for room acoustics or short-range outdoor propagation [83, 60]. In this case, the number of transmission lines $m \in \{1, \dots, M = 2 \times d\}$, as two nodes are linked to the local node in each spatial direction. The $2d$ size scattered and incident pulses vectors are expressed, respectively:

$$ {}_n\underline{\mathrm{I}}_{\mathbf{r}} = {}_n \left[I^1; \ \dots \ ; I^{2d} \right]_{\mathbf{r}}^{\mathrm{T}}, \tag{2.6a} $$

$$ {}_n\underline{\mathrm{S}}_{\mathbf{r}} = {}_n \left[S^1; \ \dots \ ; S^{2d} \right]_{\mathbf{r}}^{\mathrm{T}}. \tag{2.6b} $$

Thanks to an electro-acoustical analogy [117] illustrated on Fig. 2.4, the reflection and transmission coefficients of the pressure at each node can be expressed by inserting $Z_{L_{\mathbf{r}}}^m = Z$ and $Z_{T_{\mathbf{r}}}^m = \dfrac{Z}{2d-1}$ in Eq. (2.3):

$$ R_{\mathbf{r}}^m = \frac{1-d}{d}, \tag{2.7a} $$

$$ T_{\mathbf{r}}^m = \frac{1}{d}. \tag{2.7b} $$

It is as if the incident pressure pulse was encountering a discontinuity between a medium of impedance $Z_{L_{\mathbf{r}}}^m = Z$ to another one of impedance $Z_{T_{\mathbf{r}}}^m = \dfrac{Z}{2d-1}$, with Z a given impedance which can vary depending on the fluid to model.

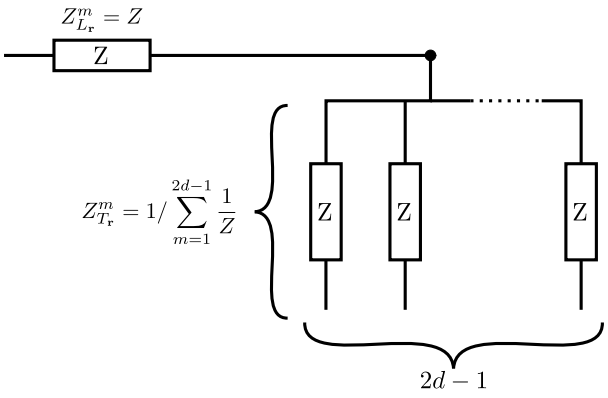

Figure 2.4. Electrical analogy scheme along one transmission line in the case of a homogeneous non-dissipative medium.

2.4.1 Link with the wave equation

In order to show that the TLM method for homogeneous non-dissipative media is consistent with the wave equation, the discrete pressure at the nodes ${}_nP_{\mathbf{r}}$ can be expressed using the Millman's theorem [33]:

$${}_nP_{\mathbf{r}} = \frac{\sum_{m=1}^{2d} \frac{2\,{}_nI_{\mathbf{r}}^m}{Z_{L_{\mathbf{r}}}^m}}{\sum_{m=1}^{2d} \frac{1}{Z_{L_{\mathbf{r}}}^n}}, \tag{2.8}$$

$${}_nP_{\mathbf{r}} = \frac{1}{d}\sum_{m=1}^{2d} {}_nI_{\mathbf{r}}^m = \sum_{m=1}^{2d} T_{\mathbf{r}}^m I_{\mathbf{r}}^m. \tag{2.9}$$

Writing the expression 2.9 at the time step $n+1$ and applying twice Eq. (1*) and Eq. (2.5) leads to [72]:

$$\begin{aligned}
{}_{n+1}P_{\mathbf{r}} &= \frac{1}{d}\sum_{m=1}^{d}\left[{}_nS^{2m}_{(j_1-\delta_{m1},\ldots,j_d-\delta_{md})} + {}_nS^{2m-1}_{(j_1+\delta_{m1},\ldots,j_d+\delta_{md})}\right],\\
{}_{n+1}P_{\mathbf{r}} &= \frac{1}{d}\left(\sum_{m=1}^{d}\left[{}_nP_{(j_1+\delta_{m1},\ldots,j_d+\delta_{md})} + {}_nP_{(j_1-\delta_{m1},\ldots,j_d-\delta_{md})}\right]\right.\\
&\qquad\left. - \sum_{m=1}^{d}\left[{}_nI^{2m}_{(j_1-\delta_{m1},\ldots,j_d-\delta_{md})} + {}_nI^{2m-1}_{(j_1+\delta_{m1},\ldots,j_d+\delta_{md})}\right]\right),\\
{}_{n+1}P_{\mathbf{r}} &= \frac{1}{d}\left(\sum_{m=1}^{d}\left[{}_nP_{(j_1+\delta_{m1},\ldots,j_d+\delta_{md})} + {}_nP_{(j_1-\delta_{m1},\ldots,j_d-\delta_{md})}\right] - \sum_{m=1}^{2d} {}_{n-1}S_{\mathbf{r}}^m\right),\\
{}_{n+1}P_{\mathbf{r}} &= \frac{1}{d}\left(\sum_{m=1}^{d}\left[{}_nP_{(j_1+\delta_{m1},\ldots,j_d+\delta_{md})} + {}_nP_{(j_1-\delta_{m1},\ldots,j_d-\delta_{md})}\right] - 2d\times {}_{n-1}P_{\mathbf{r}} + \sum_{m=1}^{2d} {}_{n-1}I_{\mathbf{r}}^m\right),
\end{aligned}$$

and finally to:

$${}_{n+1}P_{\mathbf{r}} + {}_{n-1}P_{\mathbf{r}} = \frac{1}{d}\sum_{m=1}^{d}\left[{}_nP_{(j_1+\delta_{m1},\ldots,j_d+\delta_{md})} + {}_nP_{(j_1-\delta_{m1},\ldots,j_d-\delta_{md})}\right]. \tag{3*}$$

To know the approximation order of this scheme, and to retrieve the wave equation, Taylor expansions can be used [83, 30]. It is important to point out that ${}_nP_{(j_1,\ldots,j_d)}$ is an approximated value of the exact pressure $p(x_1,\ldots,x_d,t_n)$ taken at the point $\mathbf{x_r} = (x_1,\ldots,x_d)$ at time t_n. The Taylor expansions are given below for convenience:

$${}_{n\pm1}P_{\mathbf{r}} = {}_nP_{\mathbf{r}} \pm \Delta t\frac{\partial p}{\partial t}(\mathbf{x_r},t_n) + \frac{\Delta t^2}{2}\frac{\partial^2 p}{\partial t^2}(\mathbf{x_r},t_n) \pm \frac{\Delta t^3}{6}\frac{\partial^3 p}{\partial t^3}(\mathbf{x_r},t_n) + \mathcal{O}\left(\Delta t^4\right), \tag{2.11a}$$

$$\begin{aligned}
{}_nP_{(j_1\pm\delta_{m1},\ldots,j_d\pm\delta_{md})} = {}_nP_{\mathbf{r}} &\pm \Delta\ell\sum_{k=1}^{d}\frac{\partial p}{\partial x_k}(\mathbf{x_r},t_n)\,\delta_{mk} + \frac{\Delta\ell^2}{2}\sum_{k=1}^{d}\frac{\partial^2 p}{\partial x_k^2}(\mathbf{x_r},t_n)\,\delta_{mk}\\
&\pm \frac{\Delta\ell^3}{6}\sum_{k=1}^{d}\frac{\partial^3 p}{\partial x_k^3}(\mathbf{x_r},t_n)\,\delta_{mk} + \mathcal{O}\left(\Delta\ell^4\right), \quad \text{for m } \in\{1,\ldots,d\}.
\end{aligned} \tag{2.11b}$$

Using Eq. (2.11b), the left side of Eq. (3*) (relative to time discretization) can be reformulated:

$$ {}_{n+1}P_{\mathbf{r}} + {}_{n-1}P_{\mathbf{r}} = 2{}_nP_{\mathbf{r}} + \Delta t^2 \frac{\partial^2 p}{\partial t^2}(\mathbf{x_r}, t_n) + \mathcal{O}\left(\Delta t^4\right). \tag{2.12} $$

Then, reminding that, $\sum_{m=1}^{d}\sum_{k=1}^{d}\frac{\partial^2 p}{\partial x_k^2}\delta_{mk} = \nabla^2 p$, the right side of Eq. (3*) (relative to spatial discretization) becomes:

$$ \sum_{m=1}^{d}\left[{}_nP_{(j_1+\delta_{m1},\ldots,j_d+\delta_{md})} + {}_nP_{(j_1-\delta_{m1},\ldots,j_d-\delta_{md})}\right] = 2d{}_nP_{\mathbf{r}} + \Delta\ell^2\nabla^2 p(\mathbf{x_r}, t_n) + \mathcal{O}\left(\Delta\ell^4\right), \tag{2.13} $$

and Eq. (3*) is expressed as the equivalent equation of the scheme:

$$ \frac{\partial^2 p}{\partial t^2} - c_{\text{TLM}}^2\nabla^2 p = \mathcal{O}\left(\Delta t^2\right) + \mathcal{O}\left(\frac{\Delta\ell^4}{\Delta t^2}\right), \tag{4*} $$

with $c_{\text{TLM}} = \dfrac{\Delta\ell}{\sqrt{d}\Delta t}$. It is now possible to identify the wave equation and to observe that the TLM model is a second-order approximation method in time and space. Another interesting observation is that the TLM solves the wave equation only if the condition $c_{\text{TLM}}^2 = c_0^2$ is fulfilled. Developing this condition gives:

$$ \frac{c_0\Delta t}{\Delta\ell} = \frac{1}{\sqrt{d}}, \tag{2.14} $$

which corresponds with the Courant-Friedrichs-Lewy (CFL) condition [115] of the so-called finite difference Leap-Frog scheme [30]. However, the approximations of the time and space second-order derivative are not exactly as the ones in the Leap-Frog scheme. Indeed, a zero-order error term $2{}_nP_{\mathbf{r}}$ appears systematically in the equivalent equations of the space and time schemes (2.13, 2.12). It is only when Eq. (2.13) and Eq. (2.12) are taken together in Eq. (3*) that the errors compensate each other.

2.4.2 Stability analysis

To evaluate the model stability, the numerical dispersion relation of the method can be written by inserting the formulation of a discretized plane wave ${}_nP_{\mathbf{r}} = A\exp\left(i\left[\sum_{l=1}^{d}k_{x_l}j_l\Delta\ell - \omega n\Delta t\right]\right)$, ($i^2 = -1$) in Eq. (3*). The time discretization (left side) becomes:

$$ {}_{n+1}P_{\mathbf{r}} + {}_{n-1}P_{\mathbf{r}} = Aexp\left(i\left[\sum_{l=1}^{d}k_{x_l}j_l\Delta\ell - \omega(n+1)\Delta t\right]\right) + Aexp\left(i\left[\sum_{l=1}^{d}k_{x_l}j_l\Delta\ell - \omega(n-1)\Delta t\right]\right) $$

$$ {}_{n+1}P_{\mathbf{r}} + {}_{n-1}P_{\mathbf{r}} = {}_nP_{\mathbf{r}}\left(e^{-iw\Delta t} + e^{iw\Delta t}\right) $$

$$ {}_{n+1}P_{\mathbf{r}} + {}_{n-1}P_{\mathbf{r}} = 2{}_nP_{\mathbf{r}}\cos(\omega\Delta t), $$

and the spatial integration (right side):

$$\sum_{m=1}^{d} \left[{}_nP_{(j_1+\delta_{m1},\ldots,j_d+\delta_{md})} + {}_nP_{(j_1-\delta_{m1},\ldots,j_d-\delta_{md})} \right] =$$

$$A \sum_{m=1}^{d} \left[\exp\left(i \left[\sum_{l=1}^{d} k_{x_l}(j_l + \delta_{ml})\Delta\ell - \omega n \Delta t \right] \right) + \exp\left(i \left[\sum_{l=1}^{d} k_{x_l}(j_l - \delta_{ml})\Delta\ell - \omega n \Delta t \right] \right) \right] =$$

$${}_nP_{\mathbf{r}} \sum_{m=1}^{d} \left[\exp\left(i \left[\sum_{l=1}^{d} k_{x_l}\delta_{ml}\Delta\ell \right] \right) + \exp\left(-i \left[\sum_{l=1}^{d} k_{x_l}\delta_{ml}\Delta\ell \right] \right) \right] =$$

$${}_nP_{\mathbf{r}} \sum_{m=1}^{d} \left[e^{ik_{x_m}\Delta\ell} + e^{-ik_{x_m}\Delta\ell} \right] =$$

$$2{}_nP_{\mathbf{r}} \sum_{m=1}^{d} \cos(k_{x_m}\Delta\ell).$$

In the end, Eq. (3*) becomes:

$$\cos(\omega\Delta t) = \frac{1}{d} \sum_{m=1}^{d} \cos(k_{x_m}\Delta\ell), \ \forall\Delta t, \ \forall\Delta\ell. \tag{5*}$$

This equation implies that the TLM method is unconditionally stable in the homogeneous non-dissipative case [57]. However, this relation also shows that the model presents numerical dispersion in the main directions of the grid (for instance in the 2D case, at angles $\theta = \beta\frac{\pi}{2}$, $\beta \in \mathbb{Z}$). To illustrate this phenomenon, the dispersion error is represented on Fig. 2.5 as a function of the angle θ between the plane wave vector and the horizontal direction of the mesh. Three cases of grid discretization along the Cartesian directions are displayed. These plots show that the relative dispersion error is below 5% when the number of points per minimal modeled wavelength $N_{\text{ppw}} = \lambda_{\min}/\Delta\ell$, $N_{\text{ppw}} \in \mathbb{N}$, is greater than 5 and that the numerical dispersion relation (5*) is exact if $\theta = \frac{\pi}{4} + \beta\frac{\pi}{2}$, $\beta \in \mathbb{Z}$. To get a better understanding, the expression of the phase speed c_{ph} is given by:

$$c_{\text{ph}} = \frac{1}{k\Delta t} \arccos\left[\frac{1}{2} \left(\cos(k\cos(\theta)\Delta\ell) + \cos(k\sin(\theta)\Delta\ell) \right) \right]. \tag{2.17}$$

For the highest dispersion error (on the horizontal or vertical here), $\theta = \beta\frac{\pi}{2}$ and $\beta \in \mathbb{Z}$, c_{ph} can be expressed as a function of N_{ppw}:

$$c_{\text{ph}} = c\,\frac{N_{\text{ppw}}}{\pi\sqrt{2}} \arccos\left[\frac{1}{2} \left(\cos\left(\frac{2\pi}{N_{\text{ppw}}} \right) + 1 \right) \right], \tag{2.18}$$

with c being the sound speed of reference in the propagation medium ($c = c_0 \approx 340 m.s^{-1}$ in the air at 20 °C).

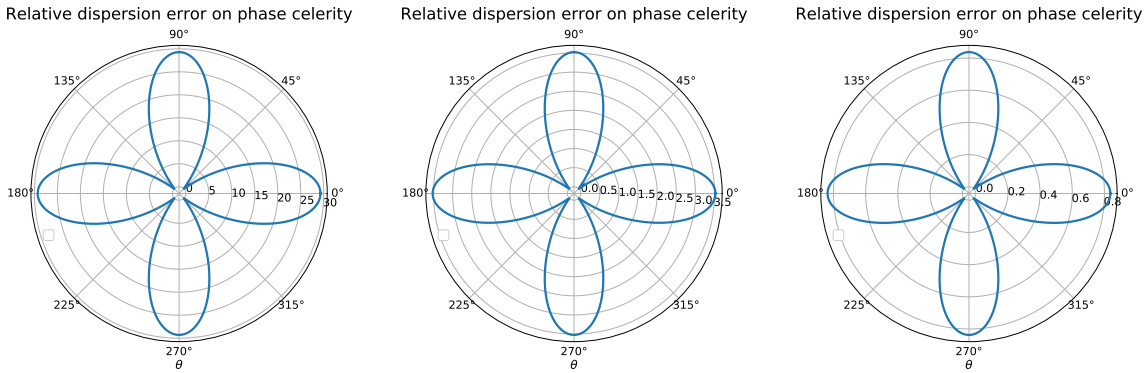

(a) $N = 2$ **(b)** $N = 5$ **(c)** $N = 10$

Figure 2.5. Relative errors on the phase speed [%] related to the model anisotropy depending on the number of points per wavelength N_{ppw}: (a) $N_{\text{ppw}} = 2$, (b) $N_{\text{ppw}} = 5$ and (c) $N_{\text{ppw}} = 10$.

2.4.3 Consequence on the group speed

From Eq. (2.18), the relation between the TLM effective group speed C_{g} and N_{ppw} is derivable. The group speed of a wave packet, characterizing the traveling speed of the signal envelope, is defined as:

$$C_{\text{g}} = \frac{\partial \omega}{\partial k}, \tag{2.19}$$

reminding that ω is the angular frequency and k is the wave number.

Since the FDTD is the closest numerical method to the TLM in terms of discretization of partial differential equations, it seems relevant to compare the error on the modeled axial sound speeds from the two models. As highlighted by the stability analysis of the TLM model, the numerical dispersion is maximal along the main directions of the mesh (Section 2.4.2). Thus, the numerical group speed C_{g} in a 2D Cartesian grid can be expressed as a function of N_{ppw} on the main directions of the mesh ($\theta = \beta\frac{\pi}{2}$, $\beta \in \mathbb{Z}$), as:

$$C_{\text{g}}(N_{\text{ppw}}) = c\,\frac{\sin\left(\frac{2\pi}{N_{\text{ppw}}}\right)}{\sqrt{2 - 0.5\left(1 + \cos\left(\frac{2\pi}{N_{\text{ppw}}}\right)\right)^2}}. \tag{2.20}$$

Similar expressions can be formulated for the group speed, for 3D cases or other 'Taylor-expansions based' numerical methods [125]. On Fig. 2.6, the phase and group speeds associated with centered finite difference schemes are compared with the ones related to the TLM method. From these figures, it is straightforward that increasing the method order reduces the dispersion errors and that the phenomenon is stronger on the group speed. For instance, more than 30 points per wavelength would be needed for the TLM to get the accuracy that the fourth-order FDTD scheme has at $N_{\text{ppw}} = 10$.

From Eq. (1.31), Eq. (2.20) and Fig. 2.6, it is straightforward that the TLM and the second-order FDTD numerical phase speeds are completely equivalents. Hence, the same conclusion is applied to the numerical group speed. These results confirm that for in-volume modeling, the TLM method is not the most performant method for universal applications. However, this statement can be moderated by the fact that a lower-order scheme implies less implementation complexity on the boundary conditions. Thus, when numerous scatterers are considered (*e.g.* in forests), second-order schemes could be attractive for their lower computational costs.

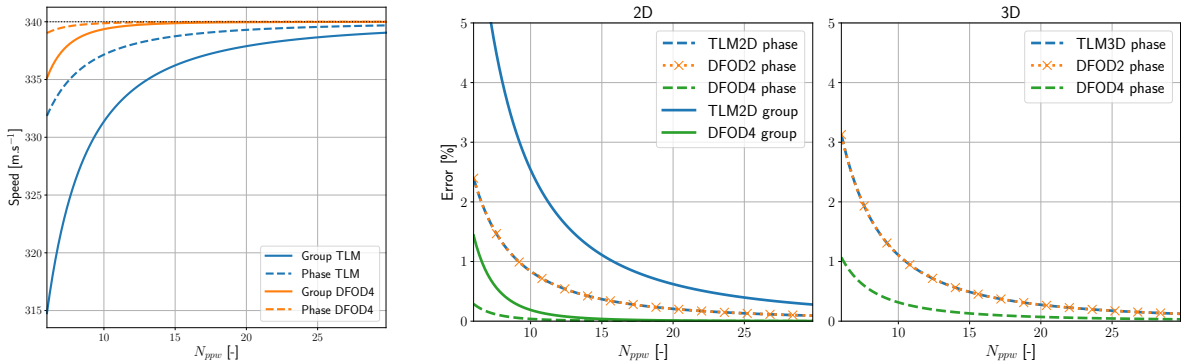

(a) **(b)**

Figure 2.6. (a) Effective speeds compared to the physical constant; (b) Relative errors on the phase and group velocities [%] related to the model anisotropy depending on the number N_{ppw}. 'DFOD2' and 'DFOD4' stand for the second and fourth-order centered finite difference schemes respectively.

2.5 Scheme for inhomogeneous dissipative media

In order to adapt the TLM model to realistic outdoor scenarios, the inhomogeneous sound velocity and the atmospheric absorption [112] are modeled by adding two specific transmission lines [84, 61]. Their impedance can vary in both space and time thanks to additional parameters η and ζ defined later in the text (see Section 2.5.2 to Section 2.5.3). A 2D example of the environment around one node is exposed on Fig. 2.7. The main differences with the homogeneous and non-dissipative medium case (Section 2.4) lie in the reflection and transmission coefficients in the diffusion matrix ${}_n\underline{\underline{D}}_{\mathbf{r}}$ and the introduction of an additional connection law that are successively detailed in the three following subsections.

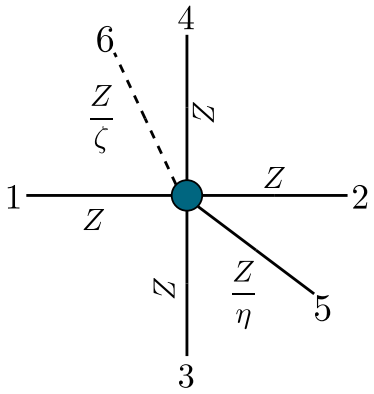

Figure 2.7. Node transmission lines diagram for a 2D inhomogeneous and dissipative medium.

2.5.1 Scheme along a regular line

The lines which superscripts $m \in \{1, \ldots, 2d\}$ have identical behaviors than those presented in Section 2.4 for a homogeneous non-dissipative medium. Their impedance depends only on the medium to model. However, as exposed on Fig. 2.8, the appearance of two additional lines changes the equivalent impedance encountered by the pulses at the corresponding nodes and

leads to the two following expressions of the diffusion matrix coefficients (Eq. (2.2)):

$$ {}_nZ^m_{T_\mathbf{r}} = \frac{Z}{{}_n\eta_\mathbf{r} + {}_n\zeta_\mathbf{r} + 2d - 1}, \tag{2.21a} $$

$$ {}_nR^m_\mathbf{r} = -\frac{{}_n\eta_\mathbf{r} + {}_n\zeta_\mathbf{r} + 2\,(d-1)}{{}_t\eta_\mathbf{r} + {}_n\zeta_\mathbf{r} + 2d}, \tag{2.21b} $$

$$ {}_nT^m_\mathbf{r} = \frac{2}{{}_n\eta_\mathbf{r} + {}_n\zeta_\mathbf{r} + 2d}. \tag{2.21c} $$

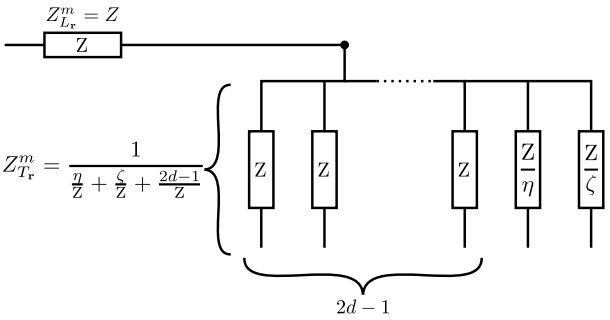

Figure 2.8. Electrical analogy scheme along regular transmission lines in the case of an inhomogeneous dissipative medium.

2.5.2 Scheme along a modified impedance line

In order to model local heterogeneity in the sound propagation velocity such as induced by wind or temperature vertical gradients, a transmission line with a reflective termination of length $\Delta\ell/2$ is introduced, with superscript $m = 2d+1$. The impedance of this branch is set as $Z^{2d+1}_\mathbf{r} = Z/\eta$, with η a parameter related to the local effective celerity [61]. As illustrated on Fig. 2.9, this line is not linked to any other node and is introduced to simulate a volume variation at the node leading to its impedance value and the following modified expressions of the diffusion matrix coefficients [84]:

$$ {}_nZ^{2d+1}_{T_\mathbf{r}} = \frac{Z}{{}_n\zeta_\mathbf{r} + 2d}, \tag{2.22a} $$

$$ {}_nR^{2d+1}_\mathbf{r} = -\frac{{}_n\eta_\mathbf{r} - {}_n\zeta_\mathbf{r} - 2d}{{}_n\eta_\mathbf{r} + {}_n\zeta_\mathbf{r} + 2d}, \tag{2.22b} $$

$$ {}_nT^{2d+1}_\mathbf{r} = \frac{2_n\,\eta_\mathbf{r}}{{}_n\eta_\mathbf{r} + {}_n\zeta_\mathbf{r} + 2d}. \tag{2.22c} $$

This extra branch at the node implies an additional connection law compared to the homogeneous and non-dissipative medium case (Eq. (1*)) that differs slightly from the usual ones since the scattered pulses are reflected back to the node of origin of the pulse, *i.e*:

$$ {}_{n+1}I^{2d+1}_\mathbf{r} = {}_nS^{2d+1}_\mathbf{r}. \tag{2.23} $$

2.5.3 Scheme along an anechoic transmission line

One method to include atmospheric absorption in the TLM model without increasing significantly computational costs consists in inserting an anechoic branch of superscript $m = 2d+2$

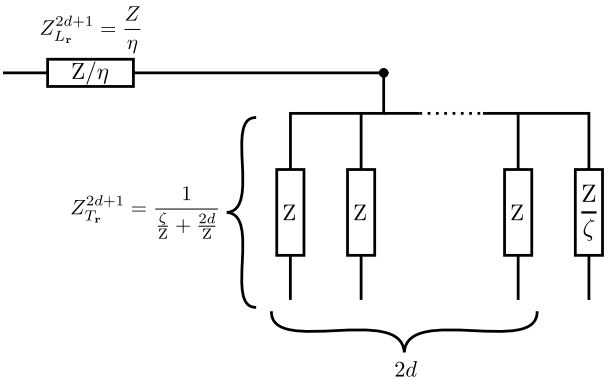

Figure 2.9. Electrical analogy scheme along the transmission line $2d+1$ in the case of an inhomogeneous dissipative medium.

and impedance $Z_{\mathbf{r}}^{2d+2} = Z/\zeta$ [83]. The parameter ζ is calculated from the atmospheric absorption coefficient α [m^{-1}]. It must be pointed out that, as the α coefficient, the ζ parameter should be frequency-dependent. This is the first limitation of this anechoic branch because it assumes a constant absorption coefficient for the frequency range of the simulation.

There is no reflection nor transmission on this line because its purpose is to simulate an amplitude loss of the pressure wave. It is then straightforward to express the reflection and the transmission coefficients as:

$$ {}_nR_{\mathbf{r}}^{2d+2} = {}_nT_{\mathbf{r}}^{2d+2} = 0. \tag{2.24}$$

Thanks to these previous developments, the matrix equation and its coefficients are set. In this case, the $(2d+1)$-dimension scattered and incident pulses vectors are expressed, respectively:

$$ {}_n\underline{\mathrm{I}}_{\mathbf{r}} = {}_n\left[I^1; \ldots; I^{2d}; I^{2d+1}\right]_{\mathbf{r}}^{\mathrm{T}}, \tag{2.25a}$$

$$ {}_n\underline{\mathrm{S}}_{\mathbf{r}} = {}_n\left[S^1; \ldots; S^{2d}; S^{2d+1}\right]_{\mathbf{r}}^{\mathrm{T}}, \tag{2.25b}$$

and ${}_n\underline{\underline{D}}_{\mathbf{r}}$ becomes a $(2d+1) \times (2d+1)$ diffusion matrix as:

$$ {}_n\underline{\underline{D}}_{\mathbf{r}} = \frac{2}{\eta_{\mathbf{r}} + \zeta_{\mathbf{r}} + 2d} \, {}_n\begin{bmatrix} a & 1 & \ldots & \ldots & \eta \\ 1 & a & 1 & \vdots & \vdots \\ \vdots & 1 & \ddots & 1 & \vdots \\ \vdots & \ldots & 1 & a & \eta \\ 1 & \ldots & \ldots & 1 & b \end{bmatrix}_{\mathbf{r}}, \tag{2.26}$$

with

$$ {}_na_{\mathbf{r}} = -\frac{{}_n\eta_{\mathbf{r}} + {}_n\zeta_{\mathbf{r}} + 2(d-1)}{2}, \tag{2.27a}$$

$$ {}_nb_{\mathbf{r}} = \frac{{}_n\eta_{\mathbf{r}} - {}_n\zeta_{\mathbf{r}} - 2d}{2}. \tag{2.27b}$$

2.5.4 Link with the wave equation

As done in the homogeneous and non-dissipative case (see Section 2.4), the discrete nodal pressure is expressed on the basis of Millman's theorem [33]:

$$ {}_n p_{\mathbf{r}} = \frac{\sum_{m=1}^{2d} \frac{2\,{}_n I_{\mathbf{r}}^m}{Z_{L_{\mathbf{r}}}^m} + \frac{2\,{}_n I_{\mathbf{r}}^{2d+1}}{Z_{L_{\mathbf{r}}}^{2d+1}}}{\sum_{m=1}^{2d} \frac{1}{Z_{L_{\mathbf{r}}}^m} + \frac{1}{Z_{L_{\mathbf{r}}}^{2d+1}} + \frac{1}{Z_{L_{\mathbf{r}}}^{2d+2}}}, $$

replacing the lines' impedance by their respective values:

$$ {}_n p_{\mathbf{r}} = \frac{2}{2d+\eta+\zeta} \left(\sum_{m=1}^{2d} {}_n I_{\mathbf{r}}^m + \eta_n I_{\mathbf{r}}^{2d+1} \right), \tag{2.28} $$

finally:

$$ {}_n p_{\mathbf{r}} = \sum_{m=1}^{2d} {}_n T_{\mathbf{r}}^m \, {}_n I_{\mathbf{r}}^m + {}_n T_{\mathbf{r}}^{2d+1} \, {}_n I_{\mathbf{r}}^{2d+1} = \sum_{m=1}^{2d+1} {}_n T_{\mathbf{r}}^m \, {}_n I_{\mathbf{r}}^m. \tag{6*} $$

It is then possible to generalize from Eq. (2.26):

$$ {}_n S_{\mathbf{r}}^m = {}_n R_{\mathbf{r}}^m \, {}_n I_{\mathbf{r}}^m + \sum_{m=1}^{2d+1} {}_n T_{\mathbf{r}}^m \, {}_n I_{\mathbf{r}}^m - T_{\mathbf{r}}^m \, {}_n I_{\mathbf{r}}^m, \ m \in \{1, \dots, 2d+1\}, $$
$$ {}_n S_{\mathbf{r}}^m = {}_n p_{\mathbf{r}} + ({}_n R_{\mathbf{r}}^m - {}_n T_{\mathbf{r}}^m) {}_n I_{\mathbf{r}}^m, \ m \in \{1, \dots, 2d+1\}, $$

so:

$$ {}_n S_{\mathbf{r}}^m = {}_n P_{\mathbf{r}} - {}_n I_{\mathbf{r}}^m, \ \forall m \ \in \{1, \dots, 2d+1\}. $$

It is interesting to point out that as well in this case, Eq. (2.5) is verified in the inhomogeneous dissipative case $\forall m \ \in \{1, \dots, 2d+1\}$.

For this demonstration, the vertical velocity gradient and the atmospheric absorption loss are considered as time-independent. Thus, the development to retrieve the equivalent wave equation starts by writing Eq. (2.28) at the time step $n+1$:

$$ \frac{2d+\eta+\zeta}{2} {}_{n+1} p_{\mathbf{r}} = \sum_{m=1}^{2d} {}_{n+1} I_{\mathbf{r}}^m + \eta_{n+1} I_{\mathbf{r}}^{2d+1}, $$
$$ \frac{2d+\eta+\zeta}{2} {}_{n+1} p_{\mathbf{r}} = \sum_{m=1}^{d} \left[{}_n S^{2m}_{(j_1-\delta_{m1}, \dots, j_d-\delta_{md})} + {}_n S^{2m-1}_{(j_1+\delta_{m1}, \dots, j_d+\delta_{md})} \right] + \eta_n S_{\mathbf{r}}^{2d+1}, $$

then applying Eq. (2.5):

$$ \begin{aligned} \frac{2d+\eta+\zeta}{2} {}_{n+1} p_{\mathbf{r}} = & \sum_{m=1}^{d} \left[{}_n P_{(j_1+\delta_{m1}, \dots, j_d+\delta_{md})} + {}_n P_{(j_1-\delta_{m1}, \dots, j_d-\delta_{md})} \right] \\ & - \sum_{m=1}^{d} \left[{}_n I^{2m}_{(j_1-\delta_{m1}, \dots, j_d-\delta_{md})} + {}_n I^{2m-1}_{(j_1+\delta_{m1}, \dots, j_d+\delta_{md})} \right] \\ & + \eta \left({}_n P_{\mathbf{r}} - {}_n I_{\mathbf{r}}^{2d+1} \right), \end{aligned} $$

$$ \begin{aligned} \frac{2d+\eta+\zeta}{2} {}_{n+1} p_{\mathbf{r}} = & \sum_{m=1}^{d} \left[{}_n P_{(j_1+\delta_{m1}, \dots, j_d+\delta_{md})} + {}_n P_{(j_1-\delta_{m1}, \dots, j_d-\delta_{md})} \right] \\ & - \sum_{m=1}^{2d} {}_{n-1} S_{\mathbf{r}}^m + \eta \left({}_n P_{\mathbf{r}} - {}_{n-1} S_{\mathbf{r}}^{2d+1} \right), \end{aligned} $$

$$\begin{aligned}
\frac{2d+\eta+\zeta}{2}{}_{n+1}p_{\mathbf{r}} &= \sum_{m=1}^{d}\left[{}_{n}P_{(j_1+\delta_{m1},\ldots,j_d+\delta_{md})}+{}_{n}P_{(j_1-\delta_{m1},\ldots,j_d-\delta_{md})}\right]-2d\times{}_{n-1}P_{\mathbf{r}}+\sum_{m=1}^{2d}{}_{n-1}I_{\mathbf{r}}^{m}\\
&\quad+\eta\left({}_{n}P_{\mathbf{r}}-{}_{n-1}P_{\mathbf{r}}+{}_{n-1}I_{\mathbf{r}}^{2d+1}\right),\\
\frac{2d+\eta+\zeta}{2}{}_{n+1}p_{\mathbf{r}} &= \sum_{m=1}^{d}\left[{}_{n}P_{(j_1+\delta_{m1},\ldots,j_d+\delta_{md})}+{}_{n}P_{(j_1-\delta_{m1},\ldots,j_d-\delta_{md})}\right]-(2d+\eta){}_{n-1}P_{\mathbf{r}}+\eta_{n}P_{\mathbf{r}}\\
&\quad+\sum_{m=1}^{2d}{}_{n-1}I_{\mathbf{r}}^{m}+\eta_{n-1}I_{\mathbf{r}}^{2d+1},\\
\frac{2d+\eta+\zeta}{2}{}_{n+1}p_{\mathbf{r}} &= \sum_{m=1}^{d}\left[{}_{n}P_{(j_1+\delta_{m1},\ldots,j_d+\delta_{md})}+{}_{n}P_{(j_1-\delta_{m1},\ldots,j_d-\delta_{md})}\right]-(2d+\eta){}_{n-1}P_{\mathbf{r}}+\eta_{n}P_{\mathbf{r}}\\
&\quad+\frac{2d+\eta+\zeta}{2}{}_{n-1}p_{\mathbf{r}}.
\end{aligned}$$

Finally, the pressure scheme is expressed as:

$$\frac{2d+\eta+\zeta}{2}{}_{n+1}p_{\mathbf{r}}+\frac{2d+\eta-\zeta}{2}{}_{n-1}p_{\mathbf{r}}=\sum_{m=1}^{d}\left[{}_{n}P_{(j_1+\delta_{m1},\ldots,j_d+\delta_{md})}+{}_{n}P_{(j_1-\delta_{m1},\ldots,j_d-\delta_{md})}\right]+\eta_{n}P_{\mathbf{r}}. \tag{7*}$$

Using Taylor expansions (as before for the homogeneous case), the terms multiplied by ζ complete the schemes presented in Eq. (2.12) and Eq. (2.13). They approximate the first-order derivative of the pressure:

$${}_{n+1}p_{\mathbf{r}}-{}_{n-1}p_{\mathbf{r}}=2\Delta t\frac{\partial p}{\partial t}\left(\mathbf{x}_{\mathbf{r}},t_n\right)+\mathcal{O}\left(\Delta t^3\right) \tag{2.34}$$

and the equivalent wave equation solved by the TLM model in a dissipative inhomogeneous medium is then:

$$\frac{1}{c_{\mathrm{TLM}}^2}\frac{\partial^2 p}{\partial t^2}-\nabla^2 p+\frac{\zeta_{(j_1,j_2)}}{2\Delta\ell^2}\left(2\Delta t\frac{\partial p}{\partial t}\right)=\mathcal{O}\left(\frac{\Delta t^4}{\Delta\ell^2}\right)+\mathcal{O}\left(\frac{\Delta t^3}{\Delta\ell^2}\right)+\mathcal{O}\left(\Delta\ell^2\right), \tag{8*}$$

with
$$c_{\mathrm{TLM}}\left(\mathbf{x}_{\mathbf{r}}\right)=\sqrt{\frac{2}{\eta_{\mathbf{r}}+2d}}\frac{\Delta\ell}{\Delta t}. \tag{2.35}$$

The meteorological effects are therefore modeled by defining an effective sound velocity c_{eff} given by [115]:

$$c_{\mathrm{eff}}=\sqrt{\gamma RT}+\underline{\mathsf{w}}.\underline{u}, \tag{2.36}$$

with γ the heat capacity ratio, R the gas constant for the considered medium, T the temperature in Kelvin, $\underline{\mathsf{w}}$ the horizontal wind speed vector and $\underline{u}$ the unit vector of the direction of sound propagation. Since the condition $c_{\mathrm{TLM}}=c_{\mathrm{eff}}$ must be fulfilled to model the acoustic wave equation, the parameter η is expressed as:

$$\sqrt{\frac{2}{\eta_{\mathbf{r}}+2d}}\frac{\Delta\ell}{\Delta t}=\sqrt{\gamma RT}+\underline{\mathsf{w}}.\underline{u}, \tag{2.37}$$

$$\eta_{\mathbf{r}}=\frac{2\Delta\ell^2}{\Delta t^2\left(\sqrt{\gamma RT}+\underline{\mathsf{w}}.\underline{u}\right)^2}-2d. \tag{2.38}$$

2.5.5 Stability analysis

The introduction of a plane wave solution of the form

$$P = A \exp\left(i\left[\sum_{l=1}^{d} k_l x_l - \omega t\right]\right)$$

in Eq. (8*) allows to express the norm of the wave vector $\underline{k} = [k_1, \ldots, k_d]^T$ as:

$$\|\underline{k}\|^2 = \frac{\omega^2}{c_{\text{TLM}}^2}\left(1 + i\frac{2\zeta}{(\eta + 2d)\omega\Delta t}\right),$$

which can be reformulated using a first-order Taylor expansion:

$$\begin{aligned} \|\underline{k}\| &\approx \frac{\omega}{c_{\text{TLM}}}\left(1 + i\frac{\zeta}{(\eta + 2d)\omega\Delta t}\right) + \mathcal{O}(\zeta^2), \\ \|\underline{k}\| &\approx k_{0\text{TLM}} + i\alpha_{\text{TLM}} + \mathcal{O}(\zeta^2), \end{aligned} \tag{2.39}$$

with $k_{0\text{TLM}} = \dfrac{\omega}{c_{\text{TLM}}}$ the norm of the wave vector in the non-dissipative case and

$$\alpha_{\text{TLM}} = \frac{\zeta}{\sqrt{2(\eta + 2d)}\Delta\ell}. \tag{9*}$$

From Eq. (2.39), it can be observed that the solution of Eq. (8*) is an attenuated wave because its amplitude decreases with the distance. However, the dependence of the absorption coefficient α_{TLM} on the parameter η shows that there is a coupling between the heterogeneity and the atmospheric absorption models. This relation is critical for the validity of the method because the atmospheric absorption effect modeled by the TLM method will then be affected by the wind and temperature conditions, which should not be the case.

Furthermore, as mentioned in [127], the theoretical absorption coefficient α is frequency-dependent whereas α_{TLM} is not. Hence, this modeling technique for atmospheric absorption is not suitable for broadband sound prediction in outdoor environments. However, post-filtering the numerical results in order to artificially apply the atmospheric absorption is still possible to compensate for this missing feature in the TLM model.

If only the heterogeneity of the sound velocity is considered ($i.e\ \zeta = 0$), the insertion of a discretized plane wave in Eq. (7*) leads to:

$$(\eta_{\mathbf{r}} + 2d)\cos(\omega\Delta t) = 2\sum_{m=1}^{d}\cos(k_{x_m}\Delta\ell) + \eta_{\mathbf{r}}. \tag{10*}$$

Rewriting the previous expression gives the dispersion equation:

$$\omega = \frac{1}{\Delta t}\arccos\left(\frac{2\sum_{m=1}^{d}\cos(k_{x_m}\Delta\ell) + \eta_{\mathbf{r}}}{\eta_{\mathbf{r}} + 2d}\right). \tag{11*}$$

According to Eq. (11*), the condition for the scheme to be stable is that the argument of the arccosine $\in [-1, 1]$, which is met only if $\eta \geq 0$ because the solution $\eta \leq -2d$ is unacceptable. The presence of the $\eta_{\mathbf{r}}$ coefficient in Eq. (11*) also shows that the scheme is dispersive. In order to characterize and quantity this dispersion, it is necessary to estimate the range of values taken by $\eta_{\mathbf{r}}$.

For a given simulation with valid results until a maximal frequency $f_{\max}$, the spatial discretization should be taken as:

$$\Delta\ell = \frac{\lambda_{\min}}{N_{\text{ppw}}} = \frac{c_{\min}}{f_{\max} N_{\text{ppw}}},$$

with $c_{\min} = \min\left(c_{\text{eff}}(z)\right),\ z \in [z_{\min},\ z_{\max}]$, the minimal sound velocity in the propagation medium. Then, in order to satisfy the stability condition:

$$\begin{aligned} \eta &\geq 0, \\ \frac{\sqrt{2}\Delta\ell}{\Delta t c_{\text{eff}}} &\geq \sqrt{2d}, \end{aligned}$$

taking $c_{\max} = \max\left(c_{\text{eff}}(z)\right)$ as the maximal sound velocity in the propagation medium to respect the stability condition in the worst case:

$$\Delta t = \frac{\Delta\ell}{\sqrt{d} c_{\max}}, \qquad (\underline{12}^*)$$

As in Ref. [61], linear vertical gradients of temperature ($\partial T/\partial z = \pm\, 0,35\ ^\circ\text{C.m}^{-1}$) and wind speed ($\partial \mathsf{w}/\partial z = \pm\, 0,2\ \text{s}^{-1}$) are assumed for the theoretical evaluation. Here the altitude z=0 is just an artifact to set $T(z{=}0) = 20\ \text{C}^o$ and $\mathsf{w}(z{=}\,0) = 0\ \text{m.s}^{-1}$, there is no ground effect considered in the stability analysis. More realistic profiles, such as linear-logarithmic [115] (called generally 'lin-log') vertical sound speed profiles could be used. However, given the height considered, the minimum and maximum values are roughly the same as the ones resulting from the linear profiles and they do not make a significant difference in the results. Then, the values of η are calculated for downward (*i.e* downwind and/or a positive temperature vertical gradient) and upward (*i.e* upwind and/or a negative temperature vertical gradient) refraction conditions. These examples are the worst-case scenarios since they present the widest ranges of values for c_{eff}. These situations give that $\eta \in [0; 4.82 \times 10^{-1}]$ for downward atmospheric conditions and $\eta \in [0; 5.22 \times 10^{-1}]$ for upward atmospheric conditions.

Figs. 2.10 and 2.11 show that the dispersion error is maximal when η is maximal (*i.e*, $c_{\text{TLM}} = c_{\min}$). The main difference with the homogeneous case is that, for $\theta = \frac{\pi}{4} + \beta\frac{\pi}{2}$ ($\beta \in \mathbb{Z}$), the scheme presents a dispersion error ($\approx 0,4\%$ for $N_{\text{ppw}} = 5$). However, these plots also highlight that this formulation of the TLM model for inhomogeneous media leads to a maximal dispersion error at the bottom part of the grid in the downward case and at the upper part of the grid in the upward case. For long-range sound propagation simulation, it is important to keep in mind these limitations of the TLM model.

Table 2.1 displays the minimum and maximum relative dispersion errors for the downward case, which correspond to the errors in the diagonal and the axial direction of the mesh, respectively. The values show that the local errors are acceptable ($< 5\%$) for $N_{\text{ppw}} = 5$ and negligible for $N_{\text{ppw}} = 10$, and they are close to those obtained in the upward case. However, these are local errors around a node, and it is necessary to study their impact at a larger space scale to observe the propagation of the dispersion error. Moreover, it is known that dispersion affects the group speed more than the phase speed does [125]. The objective of Chapter 3 is to investigate these effects quantitatively by conducting a long-range numerical propagation experiment.

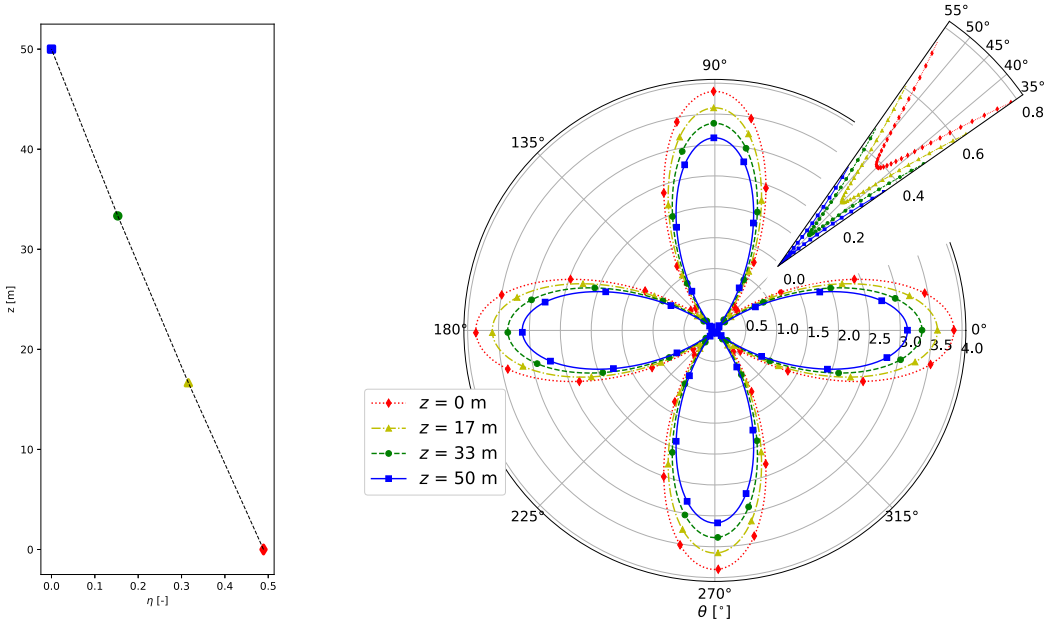

(a) **(b)**

Figure 2.10. Modeling of downward refraction conditions for $N_{\text{ppw}} = 5$: (a) evolution of η according to the height z; (b) relative errors on the phase speed [%] according to z and θ.

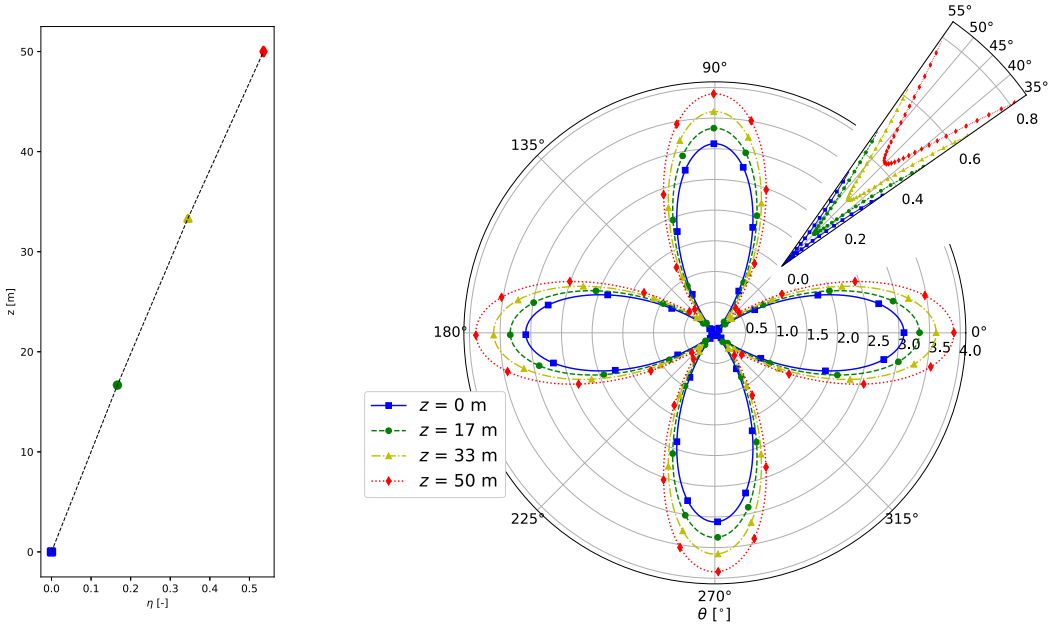

(a) **(b)**

Figure 2.11. Modeling of upward refraction conditions for $N_{\text{ppw}} = 5$: (a) evolution of η according to the height z; (b) relative errors on the phase speed [%] according to z and θ.

η \ N_{ppw}	2		5		10	
	min [%]	max [%]	min [%]	max [%]	min [%]	max [%]
4.89e-01	3.85e+00	3.03e+01	3.85e-01	3.87e+00	9.12e-02	9.26e-01
3.16e-01	2.52e+00	2.86e+01	2.49e-01	3.60e+00	5.89e-02	8.61e-01
1.53e-01	1.24e+00	2.70e+01	1.21e-01	3.35e+00	2.85e-02	8.01e-01
0.00e+00	1.56e-04	2.55e+01	1.74e-05	3.12e+00	4.18e-06	7.44e-01

Table 2.1. Minimum and maximum values of the relative error on phase speed for various (η, N_{ppw}) configurations. Values for upward and downward cases are similar.

2.6 Source definition and numerical implementation

In the original implementation of the TLM for sound propagation made by the UMRAE laboratory, sound sources are defined as punctual sources with time-varying support. The source signal mainly used in previous works [60] is an omnidirectional point sound source with Gaussian time support:

$$S(\underline{\mathrm{r}}_s, n) = A \exp\left(-\pi^2 \left(f_c n \Delta t - 1\right)^2\right), \tag{2.40}$$

where A is the source amplitude. However, implementing a source with this method should be done carefully because it does not guarantee that the pressure at the point source is forced to this value. Indeed, the value at the source point is impacted by the connection laws Eq. (1*) when $n > 0$. The formalism describing the implemented source is the following:

- For $n = 0$:

  ${}_0I^m_{\underline{\mathrm{r}}_s} = \dfrac{S(\underline{\mathrm{r}}_s, 0)}{2}$, which gives, in the homogeneous non-dissipative case:

  $$ {}_0P_{\underline{\mathrm{r}}_s} = \frac{1}{d} \sum_{m=1}^{2d} \frac{S(\underline{\mathrm{r}}_s, 0)}{2} = S(\underline{\mathrm{r}}_s, 0), \tag{2.41}$$

  which corresponds to the wanted pressure condition at the node.

- For $n > 0$:

  In this case, the connection laws must be applied:

  $$\text{for } k \in \{1, \ldots, d\} : \begin{cases} {}_nI^{2k-1}_{\underline{\mathrm{r}}_s} = \frac{S(\underline{\mathrm{r}}_s, n)}{2} + {}_{n-1}S^{2k}_{(j_1-\delta_{k1},\ldots,j_d-\delta_{kd})} \\ {}_nI^{2k}_{\underline{\mathrm{r}}_s} = \frac{S(\underline{\mathrm{r}}_s, n)}{2} + {}_{n-1}S^{2k-1}_{(j_1+\delta_{k1},\ldots,j_d+\delta_{kd})}. \end{cases} \tag{13*}$$

  Rewriting the pressure (Eq. (2.9)) leads to:

  $$ {}_nP_{\underline{\mathrm{r}}_s} = \frac{1}{d}\left(\sum_{m=1}^{2d} \frac{S(\underline{\mathrm{r}}_s, n)}{2} + \sum_{m=1}^{d} \left[{}_{n-1}S^{2m}_{(j_1-\delta_{k1},\ldots,j_d-\delta_{kd})} + {}_{n-1}S^{2m-1}_{(j_1+\delta_{k1},\ldots,j_d+\delta_{kd})}\right]\right). \tag{14*}$$

In the end, the pressure at the source node is given by:

$$ {}_nP_{\underline{\mathrm{r}}_s} = S(\underline{\mathrm{r}}_s, n) + H_{\mathrm{TLM}}\{S(\underline{\mathrm{r}}_s, n)\}, \tag{15*} $$

with H_{TLM} the transfer function of the TLM model at the source node. The pressure condition is then:

$$ p_a(\underline{r} = \underline{r}_s) = S_g(t) + h_{\mathrm{TLM}} * S_g(t) \tag{16*} $$

with h_{TLM} the 'impulse response' of the TLM model at the source node.

This specificity of the implementation must be taken into account when using the method, especially when comparing analytical solutions or measurements with quantitative source amplitude definition. In most cases, considering relative sound pressure levels or pressure normalization are solutions to tackle with this source formulation.

After establishing the theoretical specifications for free-field sound wave modeling, attention must now be directed toward detailing the modeling of boundary conditions for accurate representations of outdoor scenarios.

2.7 Specular reflection condition

In order to model a simple specular interaction of a sound wave with a reflective boundary, the TLM model uses a plane wave pressure reflection coefficient [67], as introduced in Section 1.4.1. Compared to the free-field connection laws from Eq. (1*), the formula governing the pulses along the transmission line between a boundary and the nearest node (Fig. 2.12) is modified as described in Eq. (2.42). Moreover, Fig. 2.12 shows that the considered node is located at distance $\Delta\ell/2$ from the boundary. This specificity ensures synchronization between the arrival of pulses reflected from a boundary and the regular pulses traveling along transmission lines of length $\Delta\ell$.

$$ {}_{n+1}I^1_{(j_1,j_2)} = R_1 \times {}_nS^1_{(j_1,j_2)}, \tag{2.42a} $$
$$ {}_{n+1}I^2_{(j_1,j_2)} = {}_nS^1_{(j_1+1,j_2)}, \tag{2.42b} $$
$$ {}_{n+1}I^3_{(j_1,j_2)} = {}_nS^4_{(j_1,j_2-1)}, \tag{2.42c} $$
$$ {}_{n+1}I^4_{(j_1,j_2)} = {}_nS^3_{(j_1,j_2+1)}. \tag{2.42d} $$

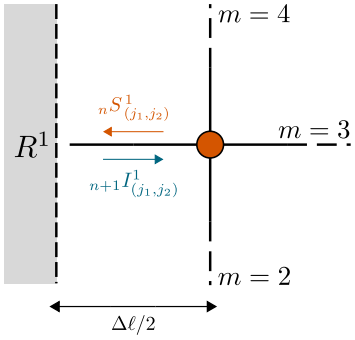

Figure 2.12. Representation of the 2D simple boundary reflection at the local node $\vec{r} = (j_1,\ j_2)$ close to a boundary. On the line $m = 1$, scattered pulse "S" (orange) at time step n becomes a reflected incident pulse "I" (blue) at next step $n + 1$.

The energetic absorption coefficient α_{abs} for the boundary is written as:

$$ \alpha_{\mathrm{abs}} = 1 - |R_m|^2, \tag{2.43} $$

where R_m corresponds to the plane wave reflection coefficient assigned to the boundary perpendicular to the branch m. The condition $R_m = 1$ describes an infinitely rigid boundary (zero particle velocity), while $R_m = -1$ accounts for a free boundary (zero acoustic pressure) and

$R_m = 0$ for a completely absorbing boundary. This type of condition is an approximation of the reflection phenomenon and does not integrate any frequency dependence. For this, impedance boundary condition, as described in Section 1.4.2, are used. They are derived hereafter for the TLM model.

2.8 TLM model implementation of impedance boundary conditions

The implementation of the boundary condition detailed in Section 1.4.2 and Section 1.4.3 is discussed below. In the TLM case, the implementation formulation does not allow to easily integrate an equation other than the wave equation, which is why the so-called recursive convolution methods are chosen over the ADE method (see Section 1.4.3).

Based on the existing literature, the coefficients A_l from Eq. (1.47) are assumed to be null [51, 60]. This initial approach limits the approximation of the complex impedance to first-order functions. For the spatial discretization, Fig. 2.13 shows that the boundary condition is located half-way between an in-volume node and an external node. The external node is then considered as a source of pulses retransmitting the behavior of the modeled boundary material. The 'instantaneous' nature of the pulses along the transmission lines implies that to write the pressure and velocity on the wall, a fictive half-step of time must be introduced. This allows for the continuous application of the electro-acoustical analogy, thereby enabling the formulation of Eqs. (2.44a) and (2.44b):

$$ {}_{n+\frac{1}{2}}P_b = {}_nS^3_{(j_1,j_2)} + {}_nS^4_{(j_1,j_2-1)}, \tag{2.44a} $$

$$ {}_{n+\frac{1}{2}}V_b = \frac{{}_nS^3_{(j_1,j_2)} - {}_nS^4_{(j_1,j_2-1)}}{Z_{\mathrm{TL}}}. \tag{2.44b} $$

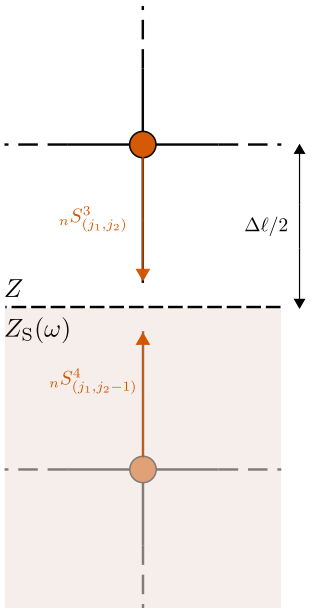

Figure 2.13. Impedance boundary condition representation at the local node $\vec{r} = (j_1,\ j_2)$ close to a boundary. Both real (opaque) and fictive (transparent) nodes emit scattered pulses "S" (orange). On the line $m = 4$ coming from the fictive node, the scattered pulse is computed from the complex acoustic impedance $Z_{\mathrm{S}}(\omega)$.

Using Eqs. (2.5) and (2.9), the pressure scheme on the boundary can be written:

$$ {}_{n+\frac{1}{2}}P_b + {}_{n-\frac{1}{2}}P_b = {}_nP_{(j_1,j_2)} + {}_nP_{(j_1,j_2-1)}, \tag{2.45a} $$

$$ {}_{n+\frac{1}{2}}V_b - {}_{n-\frac{1}{2}}V_b = \frac{{}_nP_{(j_1,j_2)} - {}_nP_{(j_1,j_2-1)}}{Z_{\mathrm{TL}}}. \tag{2.45b} $$

Replacing by Taylor expansions, a classical formulation of an acoustic impedance boundary condition is retrieved [115, 112]:

$$\frac{\partial v}{\partial t} - \frac{\sqrt{2}c_{\text{tlm}}}{Z_{\text{TL}}}\frac{\partial p}{\partial n_\perp} = \mathcal{O}(\Delta t^2) + \mathcal{O}(\Delta l^2), \tag{17*}$$

with $n_\perp$ the normal direction to the boundary surface.

For the node (j_1, j_2) to receive the appropriate incident pulse every time step, the scattered pulse ${}_nS^4_{(j_1,j_2-1)}$ must be determined (superscript 4 is consistent with the example of Fig. 2.13). To do so, Eq. (1.51) is replaced in Eq. (1.56). The PCRC case, available in the literature [67] and the PLRC case proposed below must be distinguished.

2.8.0.a Piecewise constant recursive convolution (PCRC)

$$\begin{aligned} {}_nP_b = {}_nV_b \Bigg(Z_{\text{S}}^{\infty} + \sum_{k=1}^{K} A_k \frac{1-e^{-\lambda_k \Delta t}}{\lambda_k} + 2\sum_{l=1}^{T} \left[B_l \text{Re}\left(\frac{1-e^{-\lambda_l^* \Delta t}}{\lambda_l^*} \right) + C_l \text{Im}\left(\frac{1-e^{-\lambda_l^* \Delta t}}{\lambda_l^*} \right) \right] \Bigg) \\ + \sum_{k=1}^{K} {}_{(n-1)}\psi_k A_k e^{-\lambda_k \Delta t} + 2\sum_{l=1}^{T} \left[B_l \text{Re}\left({}_{n-1}\psi_l e^{-\lambda_l^* \Delta t} \right) + C_l \text{Im}\left({}_{n-1}\psi_l e^{-\lambda_l^* \Delta t} \right) \right]. \end{aligned} \tag{2.46}$$

Writing Eq. (2.46) at time step $n + \frac{1}{2}$ and using Eq. (2.44), the scattered pulse formulation becomes:

$${}_nS^4_{(j_1,j_2-1)} = {}_nS^3_{(j_1,j_2)} \frac{\Lambda - 1}{\Lambda + 1} + \frac{{}_{n-\frac{1}{2}}\Psi}{\Lambda + 1}, \tag{2.47a}$$

$$Z_{\text{TL}}\Lambda = Z_{\text{S}}^{\infty} + \sum_{k=1}^{K} A_k \frac{1-e^{-\lambda_k \Delta t}}{\lambda_k} + 2\sum_{l=1}^{T} \left[B_l \text{Re}\left(\frac{1-e^{-\lambda_l^* \Delta t}}{\lambda_l^*} \right) + C_l \text{Im}\left(\frac{1-e^{-\lambda_l^* \Delta t}}{\lambda_l^*} \right) \right], \tag{2.47b}$$

$${}_{n-\frac{1}{2}}\Psi = \sum_{k=1}^{K} {}_{n-\frac{1}{2}}\psi_k A_k e^{-\lambda_k \Delta t} + 2\sum_{l=1}^{T} \left[B_l \text{Re}\left({}_{n-\frac{1}{2}}\psi_l e^{-\lambda_l^* \Delta t} \right) + C_l \text{Im}\left({}_{n-\frac{1}{2}}\psi_l e^{-\lambda_l^* \Delta t} \right) \right]. \tag{2.47c}$$

Eq. (2.47) describes the calculation of the scattered pulse by the accumulators at time step n. They are computed according to their values at the previous time step:

$${}_{n-\frac{1}{2}}\psi_k = \left(\frac{{}_{n-1}S^3_{(j_1,j_2)} - {}_{n-1}S^4_{(j_1,j_2-1)}}{Z_{\text{TL}}} \right) \frac{1-e^{-\lambda_k \Delta t}}{\lambda_k} + {}_{n-\frac{3}{2}}\psi_k e^{-\lambda_k \Delta t}, \tag{2.48a}$$

$${}_{n-\frac{1}{2}}\psi_l = \left(\frac{{}_{n-1}S^3_{(j_1,j_2)} - {}_{n-1}S^4_{(j_1,j_2-1)}}{Z_{\text{TL}}} \right) \frac{1-e^{-\lambda_l^* \Delta t}}{\lambda_l^*} + {}_{n-\frac{3}{2}}\psi_l e^{-\lambda_l^* \Delta t}. \tag{2.48b}$$

Fictive half-time steps arise from the instantaneous propagation along a transmission line. This approach offers computational time savings compared to the direct implementation of Eq. (1.44). However, it is important to note that $Z_{\text{TL}} \neq Z$, Z being the impedance of the physical medium (*cf.* Fig. 2.13). Therefore, it is necessary to consider $Z_{\text{TL}} = \rho_0 \frac{\Delta l}{\Delta t}$, which denotes the impedance of the transmission line crossing the domain boundary. The following assumption is then made: the virtual point is situated 'in the fluid' (as if the boundary did not exist), and all the information regarding the material located at the boundary is carried by the quantity $z_{\text{S}}(t)^M$.

2.8.0.b Piecewise linear recursive convolution (PLRC)

$$
\begin{aligned}
{}_nP_b = {}_nV_b \Bigg(& Z_{\mathrm{S}}^{\infty} + \sum_{k=1}^{K} A_k \frac{\lambda_k \Delta t + e^{-\lambda_k \Delta t} - 1}{\lambda_k^2 \Delta t} \\
& + 2 \sum_{l=1}^{T} \left[B_l \mathrm{Re} \left(\frac{\lambda_l^* \Delta t + e^{-\lambda_l^* \Delta t} - 1}{(\lambda_l^*)^2 \Delta t} \right) + C_l \mathrm{Im} \left(\frac{\lambda_l^* \Delta t + e^{-\lambda_l^* \Delta t} - 1}{(\lambda_l^*)^2 \Delta t} \right) \right] \Bigg) \\
& + {}_{n-1}V_b \Bigg(\sum_{k=1}^{K} A_k \frac{1 + e^{-\lambda_k \Delta t}(-\lambda_k \Delta t - 1)}{\lambda_k^2 \Delta t} \\
& + 2 \sum_{l=1}^{T} \left[B_l \mathrm{Re} \left(\frac{1 + e^{-\lambda_l^* \Delta t}(-\lambda_l^* \Delta t - 1)}{(\lambda_l^*)^2 \Delta t} \right) + C_l \mathrm{Im} \left(\frac{1 + e^{-\lambda_l^* \Delta t}(-\lambda_l^* \Delta t - 1)}{(\lambda_l^*)^2 \Delta t} \right) \right] \Bigg) \\
& + \sum_{k=1}^{K} {}_{(n-1)}\psi_k A_k e^{-\lambda_k \Delta t} + 2 \sum_{l=1}^{T} \left[B_l \mathrm{Re} \left({}_{n-1}\psi_l e^{-\lambda_l^* \Delta t} \right) + C_l \mathrm{Im} \left({}_{n-1}\psi_l e^{-\lambda_l^* \Delta t} \right) \right]. \qquad (2.49)
\end{aligned}
$$

Applying the same reasoning as above with the corresponding accumulators (Eq. (1.58)), the scattered pulse becomes:

$$
{}_nS^4_{(j_1,j_2-1)} = {}_nS^3_{(j_1,j_2)} \frac{\Lambda - 1}{\Lambda + 1} + ({}_{n-1}S^3_{(j_1,j_2)} - {}_{n-1}S^4_{(j_1,j_2-1)}) \frac{\Phi}{\Lambda + 1} + \frac{{}_{n-\frac{1}{2}}\Psi}{\Lambda + 1}, \qquad (\underline{18}^*\mathrm{a})
$$

$$
\begin{aligned}
Z_{\mathrm{TL}}\Lambda = & Z_{\mathrm{S}}^{\infty} + \sum_{k=1}^{K} A_k \frac{\lambda_k \Delta t + e^{-\lambda_k \Delta t} - 1}{\lambda_k^2 \Delta t} \\
& + 2 \sum_{l=1}^{T} \left[B_l \mathrm{Re} \left(\frac{\lambda_l^* \Delta t + e^{-\lambda_l^* \Delta t} - 1}{(\lambda_l^*)^2 \Delta t} \right) + C_l \mathrm{Im} \left(\frac{\lambda_l^* \Delta t + e^{-\lambda_l^* \Delta t} - 1}{(\lambda_l^*)^2 \Delta t} \right) \right], \qquad (\underline{18}^*\mathrm{b})
\end{aligned}
$$

$$
\begin{aligned}
Z_{\mathrm{TL}}\Phi = & \sum_{k=1}^{K} A_k \frac{1 + e^{-\lambda_k \Delta t}(-\lambda_k \Delta t - 1)}{\lambda_k^2 \Delta t} \\
& + 2 \sum_{l=1}^{T} \left[B_l \mathrm{Re} \left(\frac{1 + e^{-\lambda_l^* \Delta t}(-\lambda_l^* \Delta t - 1)}{(\lambda_l^*)^2 \Delta t} \right) + C_l \mathrm{Im} \left(\frac{1 + e^{-\lambda_l^* \Delta t}(-\lambda_l^* \Delta t - 1)}{(\lambda_l^*)^2 \Delta t} \right) \right], \qquad (\underline{18}^*\mathrm{c})
\end{aligned}
$$

$$
{}_{n-\frac{1}{2}}\Psi = \sum_{k=1}^{K} {}_{n-\frac{1}{2}}\psi_k A_k e^{-\lambda_k \Delta t} + 2 \sum_{l=1}^{T} \left[B_l \mathrm{Re} \left({}_{n-\frac{1}{2}}\psi_l e^{-\lambda_l^* \Delta t} \right) + C_l \mathrm{Im} \left({}_{n-\frac{1}{2}}\psi_l e^{-\lambda_l^* \Delta t} \right) \right], \qquad (\underline{18}^*\mathrm{d})
$$

compared to the PCRC, an additional term emerges in the expression of the accumulators:

$$
\begin{aligned}
{}_{n-\frac{1}{2}}\psi_k = & \left(\frac{{}_{n-1}S^3_{(j_1,j_2)} - {}_{n-1}S^4_{(j_1,j_2-1)}}{Z_{\mathrm{TL}}} \right) \frac{\lambda_k \Delta t + e^{-\lambda_k \Delta t} - 1}{\lambda_k^2 \Delta t} \\
& + \left(\frac{{}_{n-2}S^3_{(j_1,j_2)} - {}_{n-2}S^4_{(j_1,j_2-1)}}{Z_{\mathrm{TL}}} \right) \frac{1 + e^{-\lambda_k \Delta t}(-\lambda_k \Delta t - 1)}{\lambda_k^2 \Delta t} + {}_{n-\frac{3}{2}}\psi_k e^{-\lambda_k \Delta t}, \qquad (\underline{19}^*\mathrm{a}) \\
{}_{n-\frac{1}{2}}\psi_l = & \left(\frac{{}_{n-1}S^3_{(j_1,j_2)} - {}_{n-1}S^4_{(j_1,j_2-1)}}{Z_{\mathrm{TL}}} \right) \frac{\lambda_l^* \Delta t + e^{-\lambda_l^* \Delta t} - 1}{(\lambda_l^*)^2 \Delta t} \\
& + \left(\frac{{}_{n-2}S^3_{(j_1,j_2)} - {}_{n-2}S^4_{(j_1,j_2-1)}}{Z_{\mathrm{TL}}} \right) \frac{1 + e^{-\lambda_l^* \Delta t}(-\lambda_l^* \Delta t - 1)}{(\lambda_l^*)^2 \Delta t} + {}_{n-\frac{3}{2}}\psi_l e^{-\lambda_l^* \Delta t}. \qquad (\underline{19}^*\mathrm{b})
\end{aligned}
$$

Unlike the PCRC, this approach exhibits a second-order accuracy in time [38], thereby preserving the precision of the TLM model. However, the values of the scattered pulses at an additional time step ($n-2$ in Eq. (19*)) is required. Consequently, the PCRC method must be used at time step $n = 1$ in order to initialize the scheme and the PLRC method can be used afterwards.

2.9 “Adapted Matched Layer” (AML) for TLM

The theory for “PML-like” (see Section 1.4.5) integration in the TLM is detailed in references [26, 27, 60] and [65]. Depending on the computational domain to be modeled, AMLs (Adapted Matched Layers) may or may not be used, as it is sometimes sufficient to expand the domain boundaries to guarantee the absence of spurious reflections in the useful time range of microphone signals. This is mostly for 2D cases, which does not imply a critical number of additional points.

2.10 Chapter summary

In this chapter, the theoretical and methodological aspects of the TLM model were discussed. A revised formulation of d-dimensional connection laws, coupled with Taylor expansions, has allowed for the expression of dispersion equations in both homogeneous non-dissipative and inhomogeneous dissipative cases. The evaluation of numerical phase and group speeds in a Cartesian mesh was then used to investigate the effect of the number of points per wavelength on the method’s accuracy. The performance of the method was compared with a higher-order accuracy finite-difference method. Furthermore, the invalidity of using atmospheric absorption integration through an additional anechoic transmission line has been highlighted. Additionally, a study on the implementation of the TLM effective sound celerity and its impact on numerical dispersion was presented. Finally, the PLRC (Piecewise Linear Recursive Convolution) formulation was introduced for the TLM implementation of impedance boundary conditions, providing a higher level of accuracy for modeling wave propagation in the presence of obstacles.

As the results presented in this chapter are theoretical and local, an additional study is conducted in the following chapter. The objective is to evaluate the impact of numerical dispersion on the modeling of long-range outdoor scenarios and quantify the potential trade-off between the scheme’s lower order of accuracy and its computational efficiency.

Chapter 3

TLM error quantification for long-range scenario modeling

The previous chapter has highlighted the numerical dispersion inherent in the TLM model (see Section 2.4.2). Consequently, the primary objective of this chapter is to investigate and quantify the resulting errors in the model for long-range outdoor scenarios, as a step towards modeling sound propagation in forests. Through the analysis of the errors, the aim is to better estimate the reliability and accuracy of TLM-based simulations for such scenarios.

The chapter begins by discussing the implementation details of the TLM model. Analyses are then performed to understand and validate the model behavior at a source excitation node. Furthermore, the effects of anisotropic dispersion in both free field scenarios and interfering wave fields (above a perfectly reflecting boundary) are investigated through numerical experiments and comparisons with analytical solutions. Additionally, an attempt is made to quantify the errors when a white noise source signal is simulated.

3.1 Implementation

The TLM code implemented by UMRAE members [64] has been used to perform the simulations presented in this document. The architecture is a hybrid Python-OpenCL™ implementation using the PyOpenCL library. This implementation handles parallel computing, treating each operation of the most costly calculation (Eq. (2.1)) as an individual work item in a C99-based language (OpenCL™). It makes efficient use of heterogeneous resources, including central processing units (CPUs) and graphics processing units (GPUs). As described in Fig. 3.1, the FreeCAD API is used to create a triangular mesh from a geometric data file and the boundary materials specifications are managed using the Open3D Python library and Pandas *dataframes* [136].

The voxelization of the 'Stanford Triangle Format'[1] (`.ply`) in a Cartesian mesh is performed using a custom voxelizator optimized to deal with large arrays[2]. Finally, the simulations are launched using multithreading on available OpenCL™ devices (CPUs and GPUs). Depending on the required memory, the simulation domain is subdivided into spatial and temporal blocks, allowing the saving of results only when necessary. The last optimization part is made by 'flattening' d-dimensional arrays into vectors of data and OpenCL™ fastens the process by parallelizing every block operation over each available device. For additional information on the implementation and author's contributions to the code, see Appendix A.

The optimization process described above is fundamental for a time-domain numerical method using Cartesian grids. Indeed, the number of elements to compute for a 3D scene

[1] `PLY` format documentation: http://gamma.cs.unc.edu/POWERPLANT/papers/ply.pdf
[2] Fastvoxel repository: https://github.com/nicolas-f/FastVoxel

is of the order of magnitude:

$$N_{\text{el}} \approx \frac{V_{\text{model}}}{c_0^3} f_{\text{max}}^3 N_{\text{ppw}}^3, \tag{3.1}$$

with $V_{\text{model}} = L_x L_y Lz$ the volume of the modeled scenario. This implies that any increase in frequency validity (f_{max}), accuracy (N_{ppw}) or dimension of the propagation domain leads to additional computational costs.

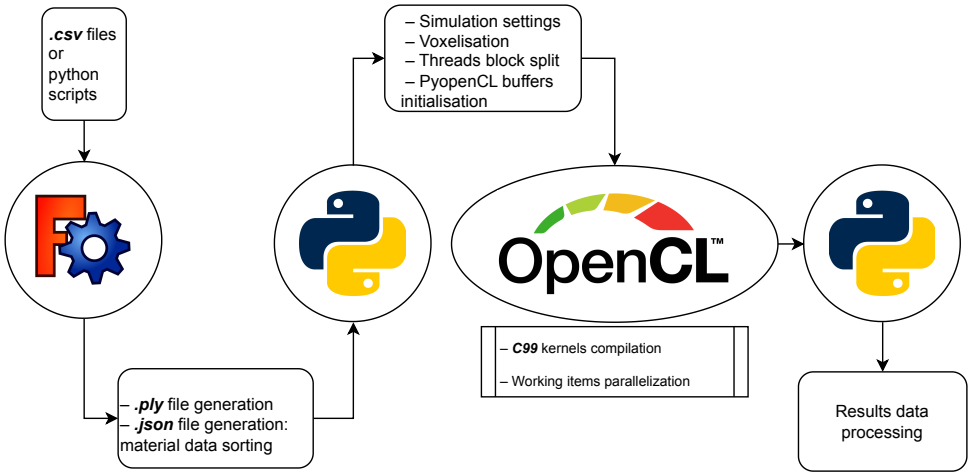

Figure 3.1. TLM code architecture from the generation of the computational domain to the processing of the simulation results.

The simulations were performed locally on an XPS 13 Dell computer under Ubuntu 20.04.6 LTS for low-computational burden simulations and on the High-Performance Computing (HPC) cluster[3] of the Strasbourg University for high-cost calculations.

After presenting the code architecture, the following sections describe the tests and experiments conducted to verify and quantify the theoretical elements discussed in Chapter 2.

3.2 Source validation for the TLM

The following sections describe numerical approximations of sound sources used to analyze behaviors of the TLM model. As introduced in Section 2.6, they are defined as time-dependent excitations generating acoustic pressure at one node of the mesh. Analytically, it is as if the source signals were defined with a Dirac $\delta(\underline{r} - \underline{r}_s)$ spatial support. Four source signals with different spectral characteristics are presented below: a numerical Dirac, a Gaussian pulse, a Ricker wavelet and a windowed sinusoidal source as each of them allows different analyses to be performed.

[3]HPC website: https://hpc.pages.unistra.fr/

3.2.1 Discrete Dirac

The Dirac signal is defined as:

$$\delta[n] = \begin{cases} 1 \text{ if } n = 0 \\ 0 \text{ if } n \neq 0 \end{cases} \quad n \in \mathbb{N}. \tag{3.2}$$

Fig. 3.2 shows the results of using Eq. (3.2) as a source signal. At the first time iteration, the value of the amplitude registered by the microphone at the node source is equal to the amplitude of the source definition. Furthermore, it can be observed that the TLM model exhibits characteristics of a Linear Time-Invariant (LTI) filter. Thus, the discrete signal displayed in red dots is the impulse response of the TLM model at the source node h_{TLM}, for a spatial discretization of five points per wavelength.

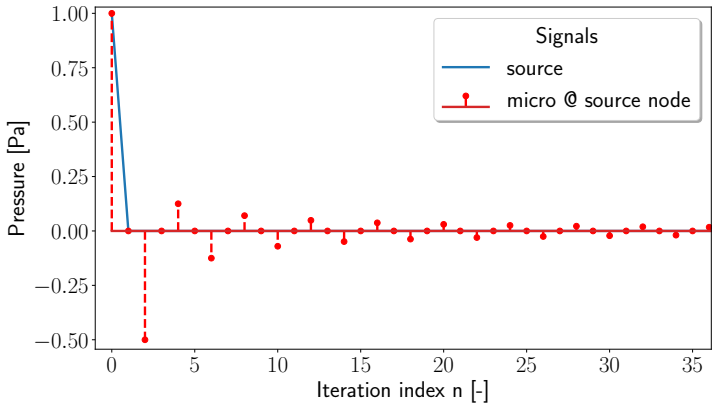

Figure 3.2. Discrete pressure signal registered at the source node in free field (red dots) when using a discrete Dirac source (blue line).

Identifying this impulse response is useful to understand the behavior of the TLM model at the source node, in order to verify that the model behaves similarly for other source signals. From Fig. 3.2, it appears that h_{TLM} is composed of a periodic function and a decaying function such as:

$$h_{\text{TLM}}[n] = \cos\left(\frac{2\pi n}{T}\right) f_{\text{decay}}[n], \tag{3.3}$$

with two versions of the function f_{decay} proposed:

$$f_{\text{decay1}}[n] = \begin{cases} \begin{cases} \exp\left(-\frac{n}{\tau_-}\right) \text{ if } n < 7 \\ \frac{1}{n^{\alpha_-}} \text{ if } n \geq 7 \end{cases} & \text{if } n = 4k+2,\ k \in \mathbb{N}, \\ \begin{cases} \exp\left(-\frac{n}{\tau_+}\right) \text{ if } n < 7 \\ \frac{1}{n^{\alpha_+}} \text{ if } n \geq 7 \end{cases} & \text{if } n = 4k+4,\ k \in \mathbb{N}, \end{cases} \tag{3.4}$$

T, τ_+, τ_-, α_+, α_- being the parameters of this function. T is the cosine period, where $T = 4$ and $n = 7$ represents the time iteration at which the decay function changes from a decreasing exponential to an inverse behavior. Then the α and τ coefficients are calculated by linear regression on the positive part of the impulse response for those with $+$ subscripts and on the negative part for those with $-$ subscripts. Since the decay function exhibits a decreasing exponential behavior that turns into an inverse function, it can also be represented using the following form:

$$f_{\text{decay2}}[n] = \left(1 - e^{-\left(\frac{n}{\tau}\right)^2}\right) \frac{1}{n^{\alpha_\pm}} + e^{-\left(\frac{n}{\tau}\right)^2} e^{-\frac{n}{\tau_\pm}}. \tag{3.5}$$

This formulation, used with $\tau' = 7$ gives approximately the same results as Eq. (3.4) while being more succinct. The control of the iteration 'switch' between the exponential form and the inverse form is made with the additional parameter τ'. The parameters α, τ were obtained by linear regression, and their values are provided in table Table 3.1.

T	τ'	τ_-	τ_+	α_-	α_+
4	7	2.88539	1.9236	1.12608	1.15327

Table 3.1. T, $\tau' = 7$, τ_+, τ_-, α_+ and α_- coefficients for the f_{decay} functions.

3.2.2 Gaussian pulse

The source signal is formulated as in Eq. (2.40). Unlike the discrete Dirac experiment in Section 3.2.1, the Fig. 3.3a shows that the amplitude of the acoustic pressure at the node source is equal to the theoretical source signal only at the first time iteration, and then discrepancies appear. These gap values increase with the iteration index and come from the neighboring nodal reflection coefficients which are applied every time-step to the source node incident pulses, as for any node of the grid (see Section 2.2).

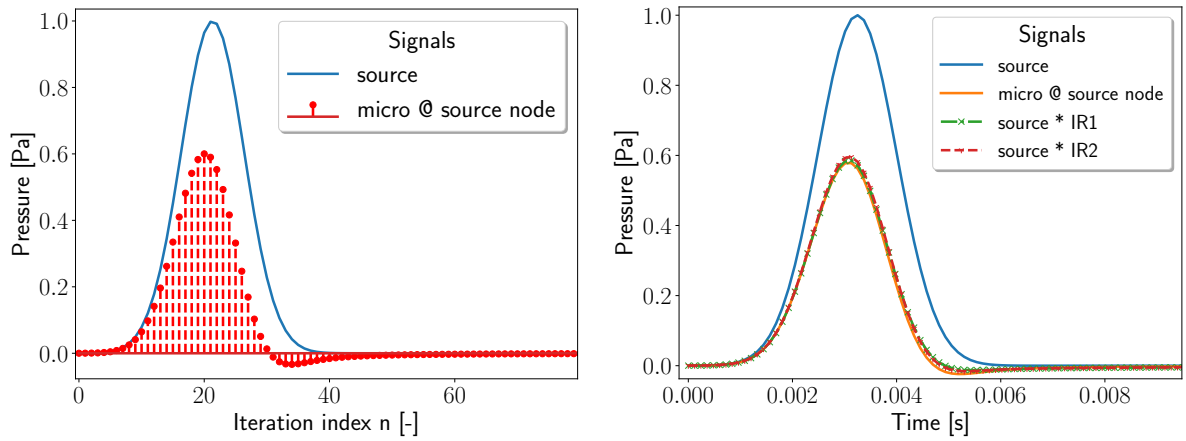

(a) **(b)**

Figure 3.3. Pressure signal registered at the source node in free field when using a Gaussian pulse source (blue line): (a) discrete signal according to iteration index (red dots), (b) convoluted signals according to time, IR1 (dashed-dot green) and IR2 (dashed red) correspond to the function h_{TLM} with f_{decay1} and f_{decay2} respectively.

When the number of points per wavelength N_{ppw} is increasing, the results obtained lead to $\lim_{N_{\text{ppw}} \to +\infty} max\left(\frac{P_{\text{sig\_mic}}}{P_{\text{sig\_source}}}\right) \approx \frac{1}{2}$, where $P_{\text{sig\_mic}}$ and $P_{\text{sig\_source}}$ are the input source signal and the pressure signal observed at the source node, respectively. This relation could be useful for future works if an accurate parametrization of the source power is required.

3.2.3 Ricker wavelet

The Ricker waveform definition used in this document is the following [133]:

$$r[n] = \left(1 - \frac{1}{2}\omega_p^2(n\Delta t)^2\right) \exp\left(-\frac{1}{4}\omega_p^2(n\Delta t)^2\right), \tag{3.6}$$

with $\omega_p = 2\pi f_r$ and f_r the most energetic frequency of the Ricker wavelet spectrum. f_r is set as $f_{\max}/2$ to ensure that all the spectral components of the signal remain below the maximal frequency of validity of the TLM model. The starting iteration has been chosen knowing that the wavelet has minima for $n_{\min} = \frac{1}{\Delta t} \pm \frac{\sqrt{3/2}}{f_r \pi}$. Thus, the signal is delayed at positive time iterations ($t_n \geq 0$).

Fig. 3.4 confirms the conclusions from Fig. 2.5 regarding the dispersion error caused by the anisotropy of the TLM scheme. The dispersion effect on the wavelet form is clearly visible in the Cartesian directions of the mesh whereas it doesn't appear on the diagonals. As mentioned in [125] and visible on Figs. 3.4b and 3.4c, the numerical dispersion affects more the high-frequency components of the wave packets (the mesh anisotropy has a greater impact on the numerical estimation of the group velocity than on the phase velocity).

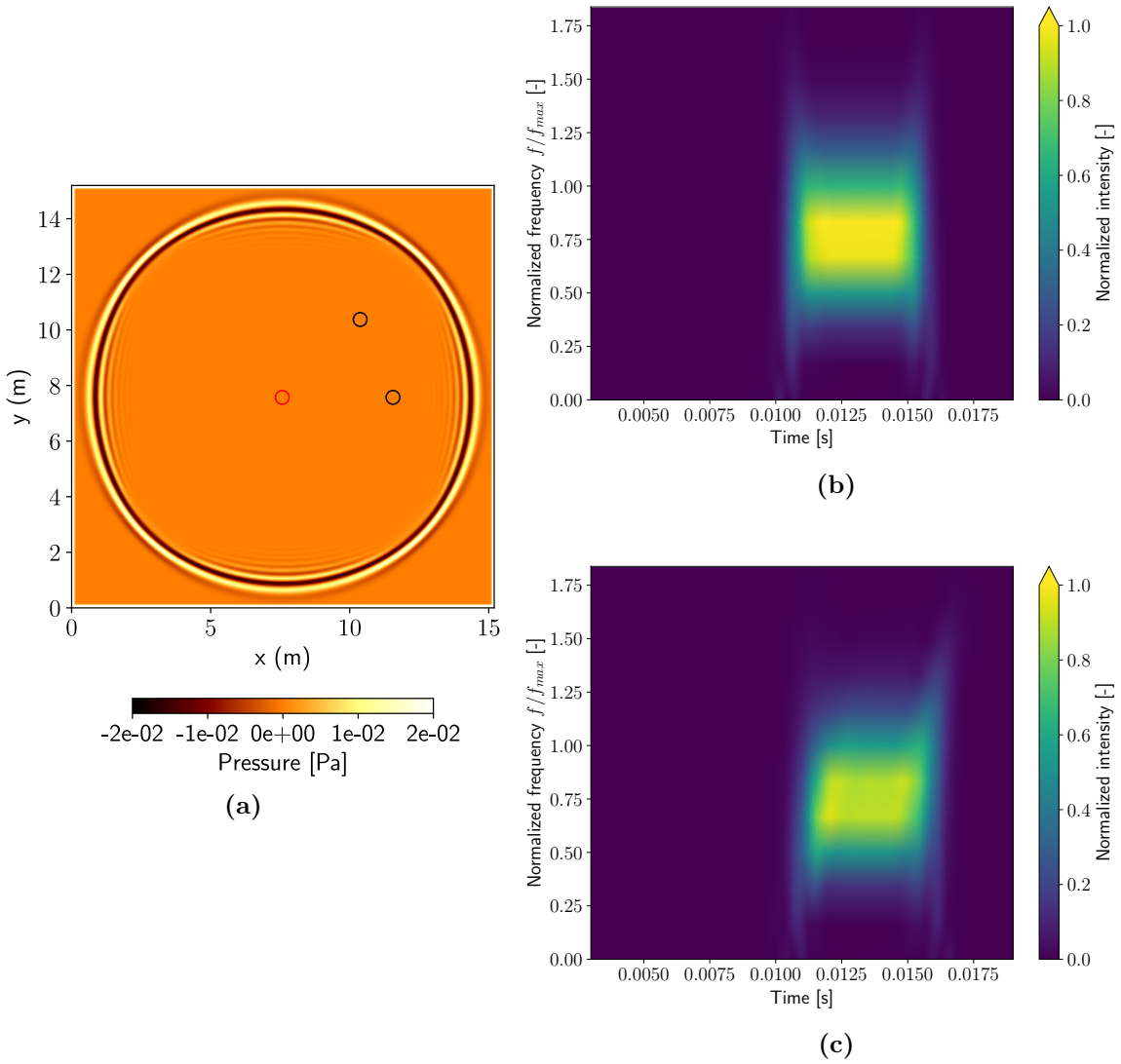

Figure 3.4. (a): 2D pressure field resulting from a central Ricker Wavelet source, with $N_{\text{ppw}} = 7$. Source represented in the center (red circle) and two microphones along the propagation path (black circles). (b) Spectrogram of the diagonal microphone, (c) spectrogram of the horizontal microphone.

3.2.4 Windowed sine

In some cases, the simulation of a harmonic source is required. However, an impulse behavior of the source is mandatory to minimize simulation times and maintain consistency in comparisons. For this, windowing a sinusoidal signal is a compromise to get a pseudo-harmonic source signal, namely:

$$\sin_{\mathrm{w}}[n] = \mathrm{w}_{\mathrm{hann}} \times \sin\left(2\pi f_{\max} n \Delta t\right) \tag{3.7}$$

with $\mathrm{w}_{\mathrm{hann}}$ a Hanning window designed according to the simulation duration and computational domain size.

Defining the sources mentioned in the sections above as space-dependent initial conditions of the simulation could also help to evaluate the behavior of the TLM. However, the spatial source definition depends on the mesh fineness, which becomes problematic for simulations involving sources near the boundaries of the domain. Thus, time-dependent implementations have been used in the numerical simulations presented in the following Sections 3.3 and 3.4.

3.3 Numerical dispersion analysis in free-field

To analyze and quantify the effects of the dispersion highlighted theoretically in Sections 2.4.2 and 2.5.5, a numerical experiment is carried out. Indeed, determining the high-frequency limits of the TLM predictions according to the distance from a sound source is fundamental when considering long-range sound propagation. The evaluation of these limits would enable the characterization of a critical source-receiver distance for a given number of points per wavelength at the maximal frequency. This analysis aims to identify configurations within which the numerical dispersion error on the results could become significant, potentially rendering them less relevant.

3.3.1 Simulation setup

As highlighted by Figs. 2.5, 2.10a and 2.11a, a 2D Cartesian mesh implies a higher dispersion error along the axial directions than along the diagonal directions. To analyze the impacts of this effect in terms of accuracy on sound pressure level predictions, the setup illustrated in Fig. 3.5 has been simulated. It is composed of an omnidirectional point source emitting a signal with Gaussian time support (see Section 2.6 and Eq. (2.40)) surrounded by two lines of eleven receivers located along the horizontal and diagonal ($\theta = \frac{\pi}{4}$) directions of the mesh. The analytic solution for this free field configuration is detailed in Appendix B and is used as reference to evaluate the numerical results from the TLM simulations.

Long-range propagation modeling (*i.e.* large ratios between distance and modeled minimum wavelength $r_{\max}/\lambda_{\min}$) becomes challenging when the frequency of validity increases. The specifications of the configuration used in the following results are given by Table 3.2 to provide an overview of the computing resources needed. To process the approximately 2700 million points to be solved and handle the associated memory load, the parallel implementation presented in Section 3.1 enables the avoidance of storing a 10 Gb matrix and facilitates the completion of the simulation in approximately 3 hours using three Nvidia GeForce GTX 1080 Ti cards.

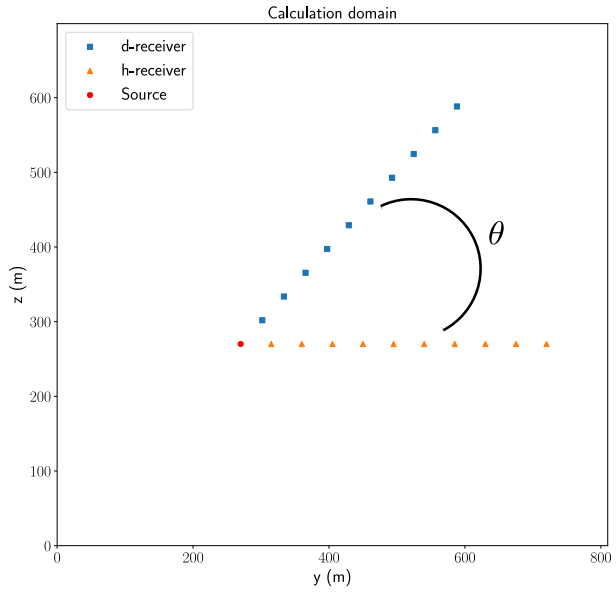

Figure 3.5. Dispersion analysis setup: source at the center (red dot) and receivers positioned along the horizontal (orange triangles) and diagonal (blue squares) directions.

$\Delta\ell$ (m)	Δt (s)	$\Delta\ell_{\text{mic}}$ (m)	$N_y \times N_z$	Memory (GB)	t_{comp} (s)	$r_{\max}/\lambda_{\min}$
1.43e-02	2.95e-05	45	56476 × 48746	10.22	11143	3176

Table 3.2. Configuration example for a 2D setup with $f_{\max} = 2400$ Hz, $N_{\text{ppw}} = 10$ and $r_{\max} = 450$ m. $N_y \times N_z$ are the number of spatial points in the respective axes. The memory usage is given for a float32 numpy array. t_{comp} is the computation time needed for this configuration, distributed over three GPUs (Nvidia GeForce GTX 1080 Ti cards).

Note that a comparison of the computational costs of the TLM model with those of other methods is not straightforward (see Section 2.4.3). Indeed, even though the TLM is equivalent to a 2-point FDTD scheme in space and time, its implementation is not based on an explicit scheme of the form $P^{n+1} = f(P^n)$. The decomposition into $2 \times d$ pulses at each point allows for the division of calculations into parallelizable computational subdomains, as described in [63]. This method significantly reduces the computation time but multiplies by $2 \times d$ the memory usage.

3.3.2 Results

This section aims at analyzing the results of the numerical experiment with a broadband sound source emitting up to $f_{\max} = 2400$ Hz, comparing the cases $N_{\text{ppw}} = 10$ and $N_{\text{ppw}} = 5$ points per wavelength. In Fig. 3.6, the envelope pressure of the signal at the receivers is displayed as a function of the reduced time $(t_n - \frac{r}{c_0})$, which allows the observation of signal flattening along the propagation distance. The effect of the dispersion along the horizontal array of receivers is directly noticeable: the results displayed on Fig. 3.6 show an apparent decrease in the group speed while the propagation distance increases. For a better visualization of this delay, the vertical lines on Fig. 3.6 indicate when 95 % of the signal energy has reached the microphone. Only the case $N_{\text{ppw}} = 10$ is shown below because a coarser grid brings longer delays, but the overall behavior of the pressure envelopes is similar for other values of N_{ppw}.

This phenomenon is confirmed by Figs. 3.7a and 3.7c which show the relative error between

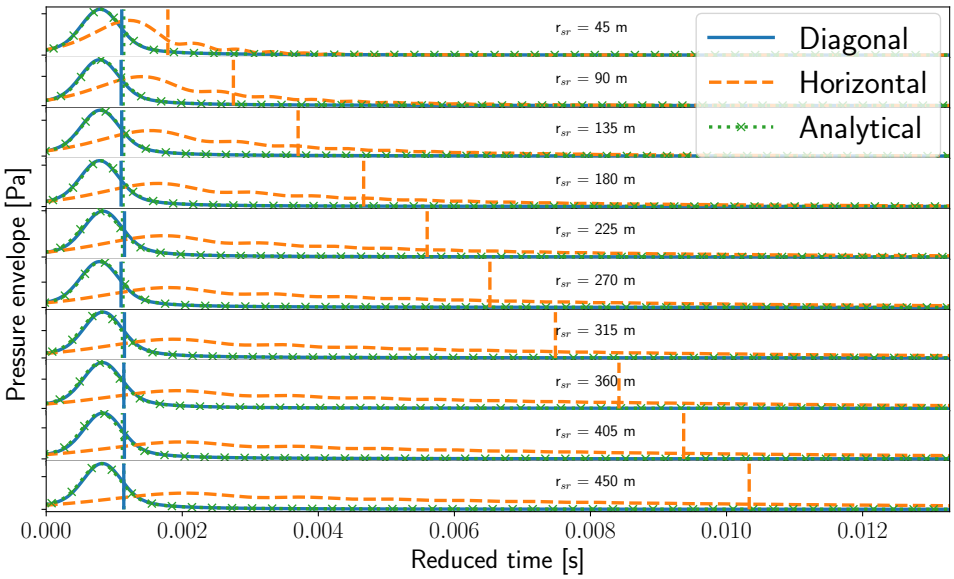

Figure 3.6. Normalized pressure envelope dependence on reduced time at receivers located at increasing distances r_{sr} [m] from the source, for $N_{\text{ppw}} = 10$ grid points per wavelength. Orange dashed vertical lines indicate the arrival of 95 % of the signal energy.

the acoustic pressures calculated by the TLM and those calculated with the analytical solution. Maximal relative errors of 0.7% ($N_{\text{ppw}} = 10$) and 2.9% ($N_{\text{ppw}} = 5$) are observed on the horizontal array of microphones. However, even if the group speed is impacted, Figs. 3.7b and 3.7d show that the calculated equivalent sound pressure levels (L_{eq}) are close to the analytical solution which confirms that the TLM is a dispersive numerical method but not a dissipative one. The simulated L_{eq} are therefore not affected in free-field because they are calculated with windowed integrals, which integrate the whole signal energy over the simulation time $t_{\text{sim}} \in [0\ s,\ 1.57\ s]$.

To better understand the frequency behavior of the numerical dispersion, the relative group speed error was calculated for third-octave frequency bands. The one-third octave band decomposition is achieved with the python module `PyFilterbank`[4] which complies with the IEC 61260-1 standard [77]. The library method applies designed Butterworth band-pass filters to the microphones signals, providing time-domain signals at the desired nominal frequencies (f_{nominal}). After this step, the arrival times of 95 % of the signals energies were computed using a bisection method. The group velocity was finally calculated from these arrival times and the source-receiver distances.

The results of this post-processing are displayed on Figs. 3.8 and 3.9, and they confirm that the high frequency contents are more delayed compared to the analytical solution and to the results from the diagonal array. The difference between the $N_{\text{ppw}} = 5$ and the $N_{\text{ppw}} = 10$ case is significant and shows that the impact of the number of points per wavelength on the error is prevailing on the propagation of the error along the source-receiver distance.

[4] `PyFilterbank` documentation: http://siggigue.github.io/pyfilterbank/

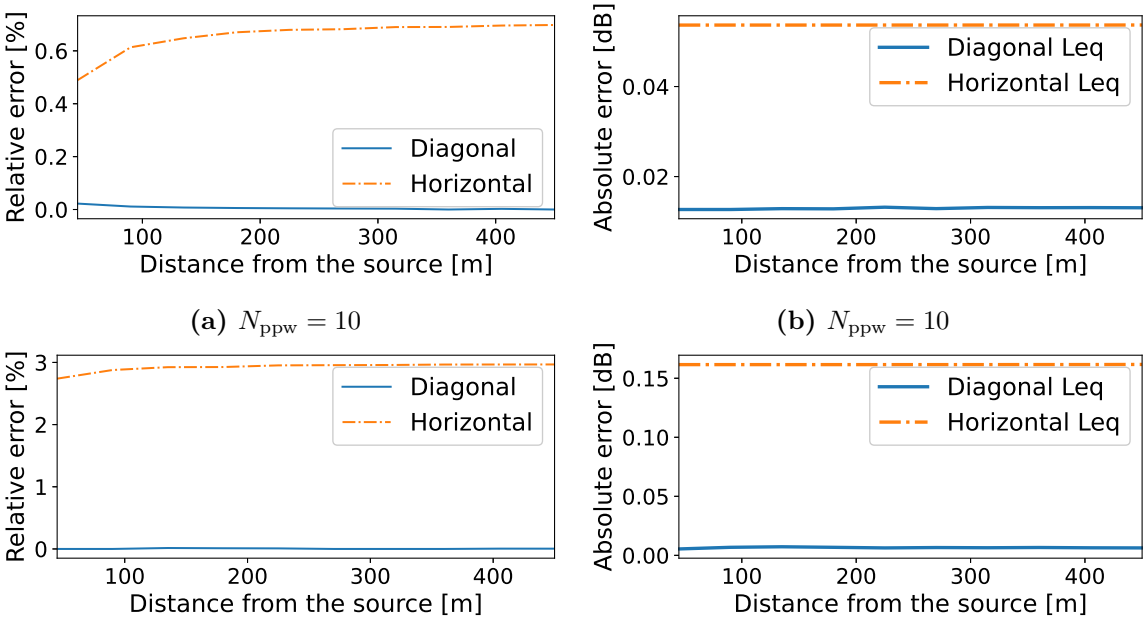

(a) $N_{\text{ppw}} = 10$ **(b)** $N_{\text{ppw}} = 10$

(c) $N_{\text{ppw}} = 5$ **(d)** $N_{\text{ppw}} = 5$

Figure 3.7. Comparison between the signals calculated by TLM and by the analytical solution depending on the propagation distance: (a) & (c) relative errors on the group velocities for $N_{\text{ppw}} = 10$ and $N_{\text{ppw}} = 5$ respectively; (b) & (d) absolute errors on L_{eq} for $N_{\text{ppw}} = 10$ and $N_{\text{ppw}} = 5$ respectively.

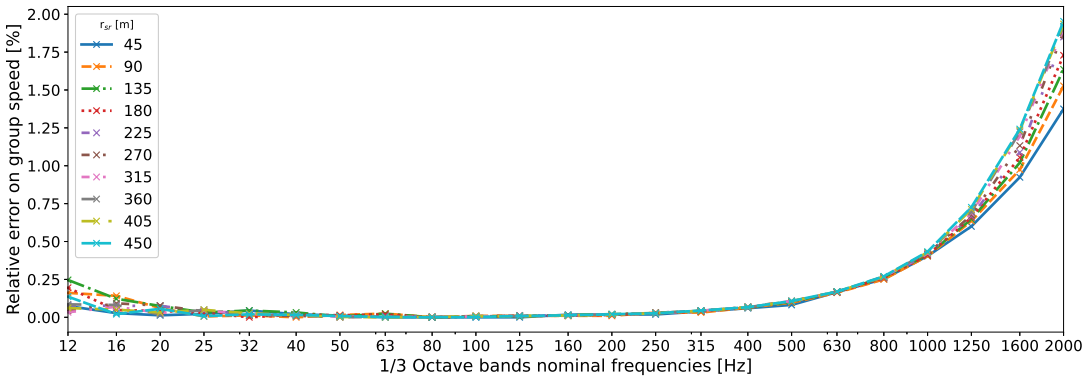

Figure 3.8. Group speed errors according to one-third octave band nominal frequencies and distance to the source for $N_{\text{ppw}} = 10$ at microphones along the horizontal direction.

Figs. 3.8 and 3.9 highlight that the inherent dispersion of the TLM model is impacting free-field long-distance simulation results. Even if the impact on the group speed is below 2% compared to the analytical solution at 450 m and $N_{\text{ppw}} = 10$ for $f_{\text{nominal}} = 2400$ Hz, further investigation is needed to characterize the effect of dispersion in more complex calculation domains. Indeed, if the high-frequency components of the signal are delayed, spurious interference patterns may occur between the direct and the reflected field and consequently impact the energy of the signal received at the microphones. In this case, the TLM dispersion could affect the simulated sound pressure levels which would be critical in the field of sound propagation predictions in outdoor environment.

From the results of this numerical experiment, the conclusion that the TLM results are

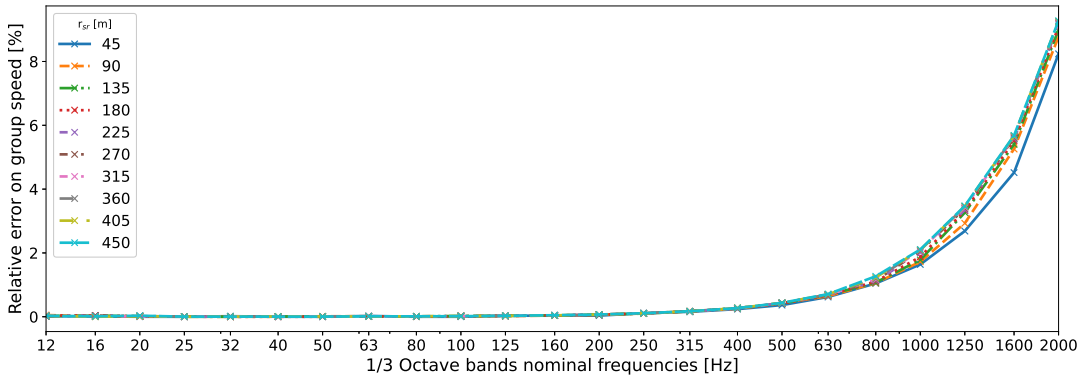

Figure 3.9. Group speed errors according to one-third octave band nominal frequencies and distance to the source for $N_{\text{ppw}} = 5$ at microphones along the horizontal direction.

valid in this configuration can be drawn provided that the number of points per wavelength is chosen large enough to lower the dispersion error. However, if N_{ppw} is too high, it will lead to significant computational costs.

Yet, the observed dispersion effects on the group speed of the test signals in the presence of boundary conditions, such as natural ground, are unknown. Thus, additional work is presented in the next section regarding TLM for modeling realistic sound fields.

3.4 Numerical dispersion analysis for fields with interfering waves

As the necessity to analyze the numerical dispersion effects in the presence of boundary conditions has been highlighted in Section 3.3, another numerical experiment is performed. Here, a reflective surface is introduced, which is more representative of outdoor sound propagation. The boundary has been chosen perfectly reflective to maximize the interference patterns, *i.e.* to study the most remarkable case. The numerical results from the TLM model are compared to the image source formulation of the analytical solution described in Section 2, considered as reference.

3.4.1 Simulation setup

The numerical experiment setup displayed on Fig. 3.10 is implemented to emphasize the two main geometric parameters: the height h_{s} between the ground and the source and the maximal distance r_{max} of the last receiver point from the source. The number of receivers in the array is also determinant since a too coarse matrix can lead to a lack of precision in the detection of the interference patterns. For the following experiments, a polar matrix of 100×100 receivers is used. The most important parameter for the analysis remains the number of points per wavelength N_{ppw} which is set to 10 at the maximal frequency f_{max} of the source emission.

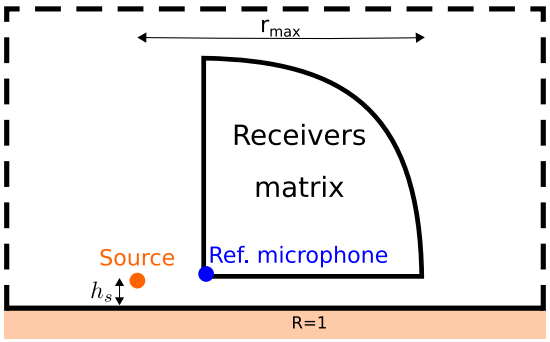

Figure 3.10. Numerical experiment setup for interfering waves analysis: sound source (orange dot) at height h_s above a perfectly reflective boundary (orange rectangle) and reference microphone (blue dot) within a polar matrix of receivers.

3.4.2 Data processing

Various approaches were considered to evaluate the dispersion error. To explain the used method, two third-order tensors ${}_n\mathfrak{n}_{j_1,j_2}$ and ${}_n\mathfrak{a}_{j_1,j_2}$ are introduced to represent numerical (TLM simulations) and analytical (formula from Section 2) results respectively. ${}_n\mathfrak{n}_{j_1,j_2}$ represents the pressure signal at the receiver $\mathbf{r} = (j_1, j_2)$ and at the time step n. Three indicators are presented to characterize the differences between ${}_n\mathfrak{n}_{j_1,j_2}$ and ${}_n\mathfrak{a}_{j_1,j_2}$: the absolute error on sound pressure levels, the mean square error and the relative error on signal energy. The use of these metrics was envisaged and they are detailed below.

3.4.2.a Absolute error on sound pressure level (SPL)

A physical and relevant indicator to evaluate the model is the absolute error on the sound pressure level $\varepsilon_{Lj_1j_2} = |L\mathfrak{a}_{j_1j_2} - L\mathfrak{n}_{j_1j_2}|\ [dB]$. The calculation of sound pressure levels is implemented as follows:

$$L\mathfrak{a}_{j_1j_2} = 10\log_{10}\left(\frac{\frac{1}{N}\sum_{n=0}^{N-1}({}_n\mathfrak{a}_{j_1,j_2})^2}{p_{\text{ref}}^2}\right). \tag{3.8}$$

3.4.2.b Mean square error

This indicator is representative of the global differences between the numerical and analytical signals. It is not an energetic indicator, but it allows the analysis of the dispersion effect on the phase of the signals. It has no real physical meaning, and it is expressed as follows:

$$\varepsilon j_1 j_{2\text{mse}} = \frac{1}{N}\sum_{n=0}^{N-1}\left(|{}_n\mathfrak{a}_{j_1,j_2} - {}_n\mathfrak{n}_{j_1,j_2}|^2\right). \tag{3.9}$$

3.4.2.c Relative error on signal energy

According to signal processing theory (and without physical meaning), the energies of the signals are expressed as $\widetilde{E}_{j_1 j_2}(\mathfrak{a}) = \sum_{n=0}^{N-1} |{}_n\mathfrak{a}_{j_1,j_2}|^2$. Then, the relative error in percent is:

$$\varepsilon j_1 j_{2\text{pct}} = 100 \left| \frac{\widetilde{E}_{j_1 j_2}(\mathfrak{a}) - \widetilde{E}_{j_1 j_2}(\mathfrak{n})}{\widetilde{E}_{j_1 j_2}(\mathfrak{a})} \right| \text{ [\%]}. \tag{3.10}$$

This metric is relevant and helps to understand the absolute error on sound pressure levels from Eq. (3.8) because

$$L\mathfrak{a}_{j_1 j_2} = 10 \log_{10} \left(\widetilde{E}_{j_1 j_2}(\mathfrak{a}) \right) - 10 \log_{10} \left(N p_{\text{ref}}^2 \right). \tag{3.11}$$

3.4.2.d Normalization

According to Section 3.2, it is not straightforward to set the source amplitude of the analytical solution because of the punctual definition of the TLM numerical source. To compare the numerical results with the analytical solution, the signals contained by the results tensors ${}_n\mathfrak{n}_{j_1,j_2}$ and ${}_n\mathfrak{a}_{j_1,j_2}$ are normalized. Three methodologies were envisaged, the following is the one elected:

$${}_n\mathfrak{n}_{j_1,j_2} = \frac{{}_n\mathfrak{n}_{j_1,j_2} \times \sigma({}_n\mathfrak{a}_{00})}{\sigma({}_n\mathfrak{n}_{00})}$$

i.e normalizing all the signals by the ratio of the standard deviations of the closest microphone to the source. This method preserves the amplitude ratio of the signals and does not lead to an error in the energy of the signals because it forces the analytical and numerical signals of the microphones (0,0) to have the same energy. The only condition is that the averages of the signals must be zero.

For a better normalization process, a polar matrix of microphones is a good way to ensure that all the receivers of one column are at the same distance from the source. Yet, it has the drawback of being more precise close to the source as the spatial steps between the receivers increase with the distance. In this case, the results tensors can be written ${}_n\mathfrak{n}_{\theta r}$ and ${}_n\mathfrak{a}_{\theta r}$, for TLM and analytical results respectively. Thus, to minimize the error introduced by the normalization, the time signals ${}_n\mathfrak{a}_{\frac{\pi}{2}0}$ and ${}_n\mathfrak{n}_{\frac{\pi}{2}0}$ are used as reference instead of ${}_n\mathfrak{a}_{00}$ and ${}_n\mathfrak{a}_{00}$ for a rectangular matrix of receivers.

3.4.2.e Attenuation relative to a reference receiver

The SPL attenuation relative to a reference receiver is used to evaluate the errors between the simulated pressure signals and the corresponding analytical solutions. For every line of receivers, the reference receiver is the closest to the source. The SPL attenuation is calculated as:

$$A_{j_1,j_2}({}_n\mathfrak{a}_{j_1,j_2}) = 10 \log_{10} \left(\frac{\sum_{n=0}^{N-1} ({}_n\mathfrak{a}_{j_1,j_2})^2}{\sum_{n=0}^{N-1} ({}_n\mathfrak{a}_{0,j_2})^2} \right). \tag{3.12}$$

To compare the numerical results with the analytical solutions, the following SPL absolute error is used:

$$\varepsilon_{j_1,j_2} = |A_{j_1,j_2}({}_n\mathfrak{a}_{j_1,j_2}) - A_{j_1,j_2}({}_n\mathfrak{n}_{j_1,j_2})| \text{ [dB]}. \tag{3.13}$$

Given all the considerations detailed in the present section about data processing metrics, it is the SPL absolute error on attenuation relative to a reference receiver with a standard deviation normalization that was chosen. It appears as the best data-processing technique to assess the appearance of spurious interference patterns brought by numerical dispersion.

3.4.3 Dispersion analysis results for interfering waves

Since the numerical dispersion affects more the high frequencies during the sound propagation [57], the analysis is performed by comparing different sources signals, regarding distinct spectral distributions. For a better understanding of the results, the number of points per wavelength N_{ppw} is presented for each source type. An overview of one simulation is displayed on Fig. 3.11 for a Gaussian pulse.

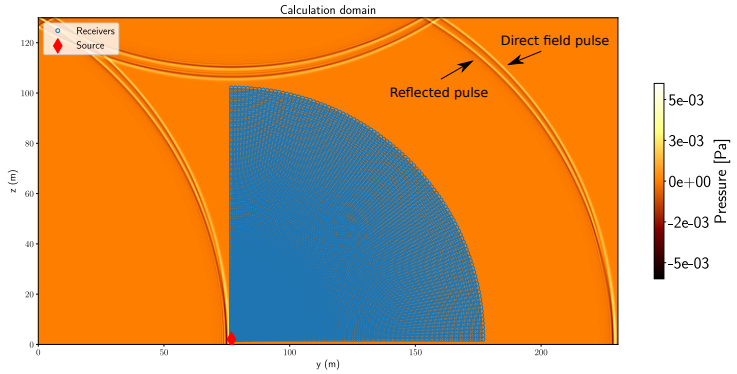

Figure 3.11. Sound pressure field for a Gaussian source at the end of the TLM simulation. The whole calculation domain is represented. At the last iteration of the calculation, reflected and incident waves have passed through all the receivers (blue dots) in the network.

In the following subsections, the absolute errors ε_{j_1,j_2} on the SPL attenuation at each receiver (*cf.* Eq. (3.13)) are displayed. The objective is to determine whether dispersion-induced delayed interferences occur in the receivers' matrix. Indeed, if there is an interference pattern for one of the delayed frequencies at a receiver, a lack of energy compared to the analytical solution will appear in the simulated signals. The following results are presented for $f_{\max} = 500$ Hz and $h_{\text{s}} = 2$ m. The simulation time is $t_{\text{sim}} = 4.19e-01\ s$ with $\Delta\ell = 6.88e-02\ m$ and $\Delta t = 4.14e-04\ s$.

3.4.3.a Gaussian pulse source

As it can be observed on Fig. 3.12, most of the spectral components of the Gaussian pulse source are over-discretized and those corresponding to $f \geq f_{\max}/2$ and $N_{\text{ppw}} \leq 10$ individually contain less than 2 % of the signal energy.

On the vertical and horizontal axes, negligible absolute errors ($\leq$ 0.05 dB) appear between the analytical and the numerical results. In addition, misplaced interference patterns are observable by a "ray" of errors in the areas where the dispersed end of the direct wavefront interacts with its reflection.

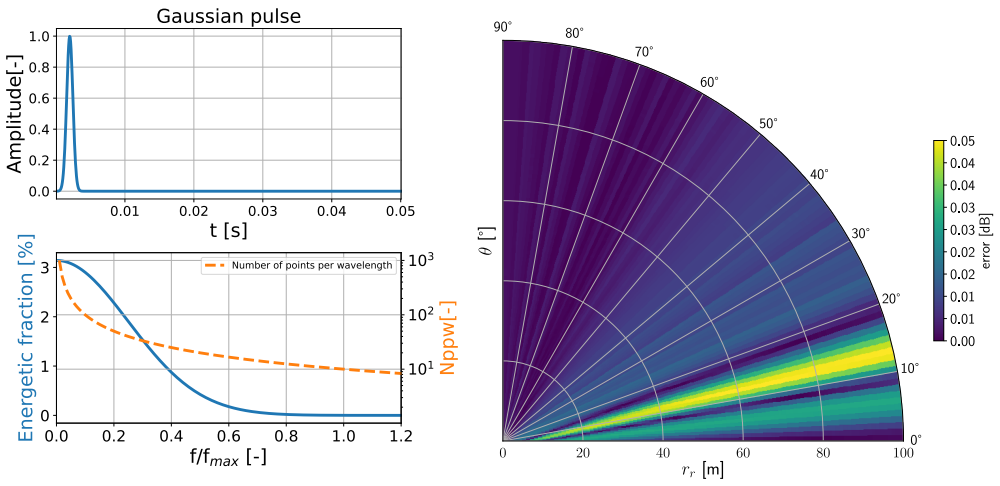

Figure 3.12. (a) Time signal according to time (top) and spectral distribution (bottom) of a Gaussian pulse compared to N_{ppw} (orange dashed line) according to normalized frequency. (b) Polar map of the SPL absolute error ε_{j_1,j_2} (Eq. (3.13)).

On Fig. 3.13, the distribution of the SPL absolute error is represented considering their statistical occurrence within the receivers' matrix. It confirms that for an over-discretized source signal, the error related to numerical dispersion is negligible (95% of the errors are below 0.03 dB).

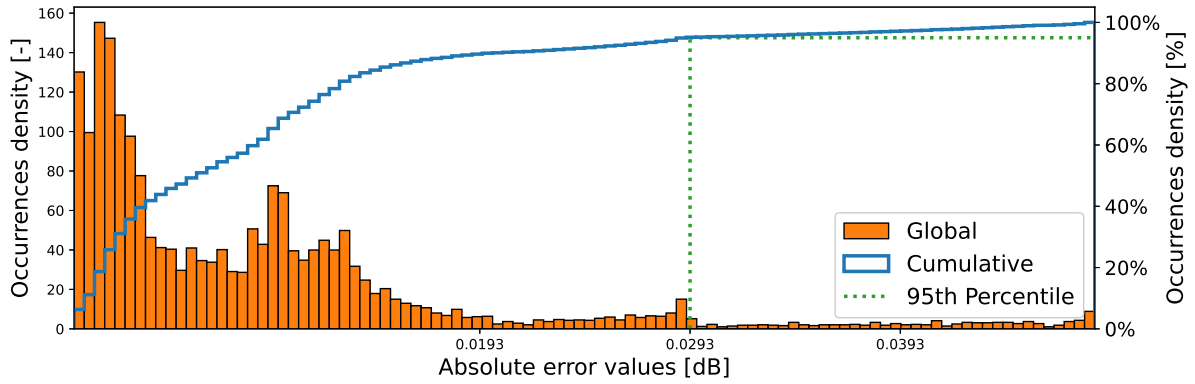

Figure 3.13. Statistical distribution of the absolute errors ε_{j_1,j_2} for the Gaussian pulse case.

3.4.3.b Shifted Gaussian pulse source

As displayed on Fig. 3.14a, the source signal has a broader spectrum than in the previous case. The excitation signal is therefore less over-sampled and the impact on the results is visible on the Fig. 3.14b. The misplaced interference patterns also appear, but the error magnitudes are slightly higher than for the regular Gaussian case because of the lower discretization of the source spectral components.

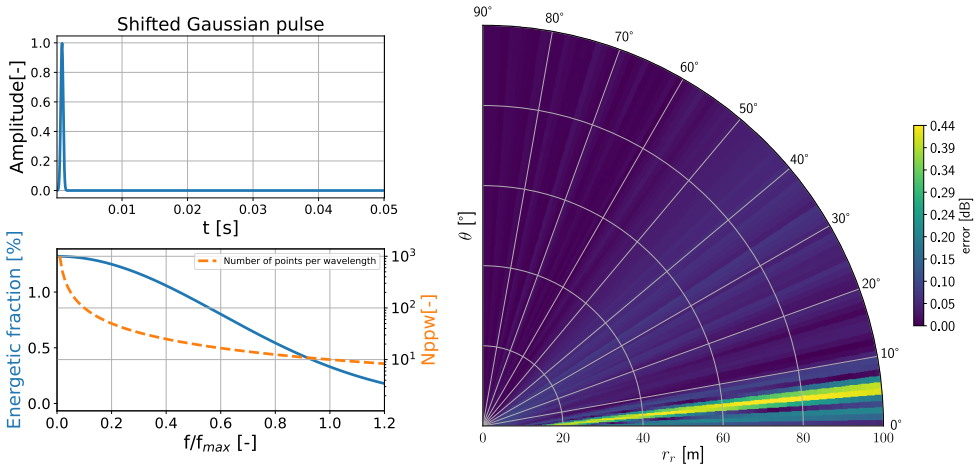

Figure 3.14. (a) Time signal according to time (top) and spectral distribution (bottom) of a shifted Gaussian pulse compared to N_{ppw} (orange dashed line) according to normalized frequency. (b) Map of the SPL absolute error ε_{j_1,j_2}.

The maximal absolute error in the polar array is of 0.44 dB and Fig. 3.15 shows that 95% of errors are below 0.1 dB. This shift of approximately a factor ten in the errors confirms that the discretization of the modeled wave packet influences the numerical dispersion effect on "long-range" results ($r_{\max} \approx 150 \times \lambda_{\min}$ here).

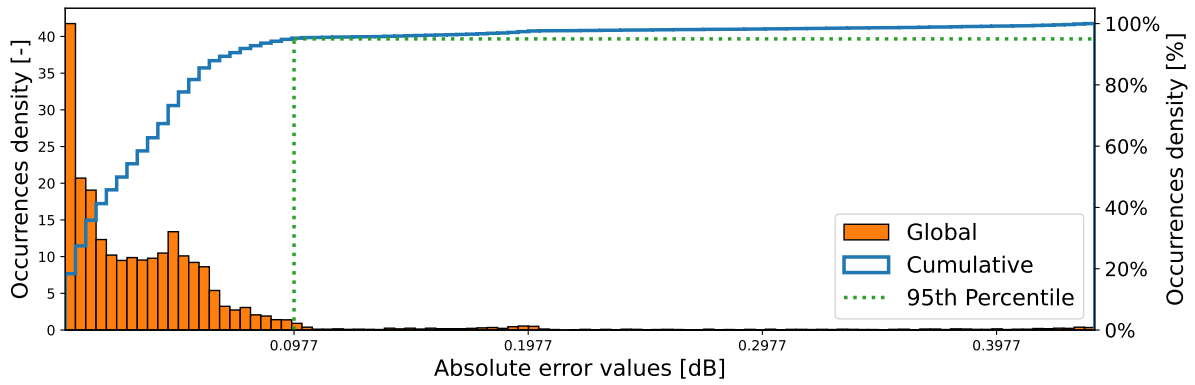

Figure 3.15. Statistical distribution of the absolute errors ε_{j_1,j_2} for the shifted Gaussian pulse case.

3.4.3.c Ricker wavelet source

The Ricker wavelet signal has a spectrum centered on $f_{\max}/2$ and this impacts the results visible on Figs. 3.16 and 3.17. The misplaced interferences pattern still appears, and the error magnitudes are higher than with the Gaussian pulse source because of the lower discretization of the high-frequency spectral components. The observed error values are similar to those with the shifted Gaussian source signal, with a slightly different statistical distribution.

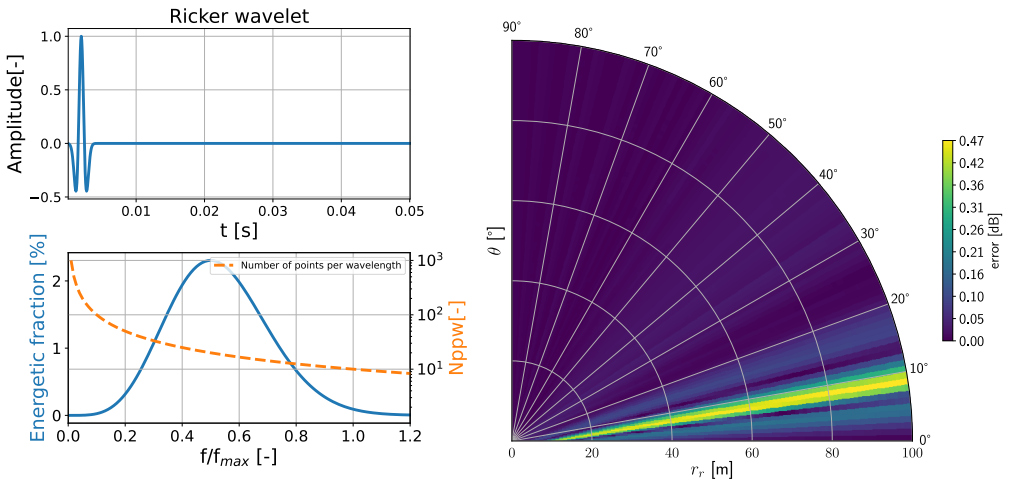

Figure 3.16. (a) Time signal according to time (top) and spectral distribution (bottom) of a Ricker wavelet compared to N_{ppw} (orange dashed line) according to normalized frequency. (b) Polar map of the SPL absolute error ε_{j_1,j_2} (Eq. (3.13)).

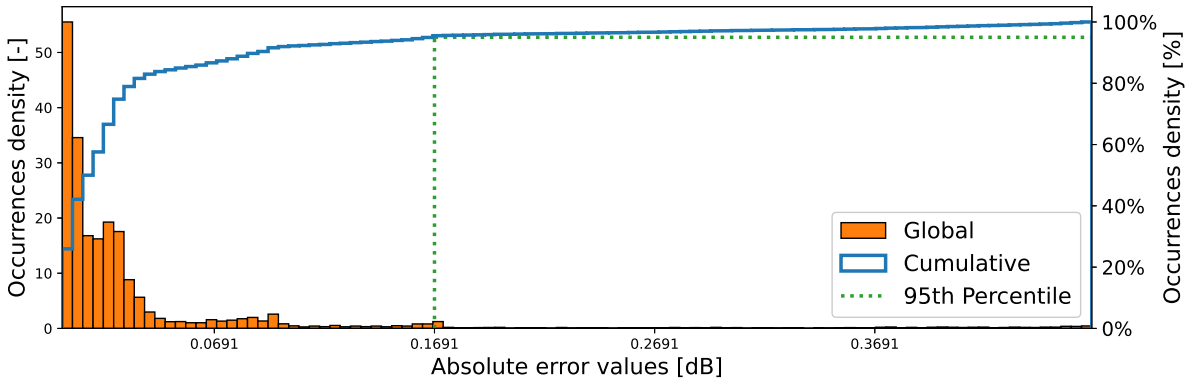

Figure 3.17. Statistical distribution of the absolute errors ε_{j_1,j_2} for the Ricker Wavelet case.

3.4.3.d Sinusoidal source

This is the most revealing case to observe misplaced interference patterns because all the source energy is focused on f_{max} and has a 10-point spatial discretization. With this spectral distribution, significant misplaced interference errors are generated by the numerical dispersion (up to 17 dB) within the polar matrix. Indeed, at some microphones, the energy of the received signal is either increased or lost due to artificial constructive or destructive interference. Comparing this error map to the one obtained with the previous pulse sources also lead to the conclusion that the spectral distribution of the source has an impact on the spatial distribution of the absolute error values: the wider the spectral distribution of the source, the wider the spatial distribution of the error.

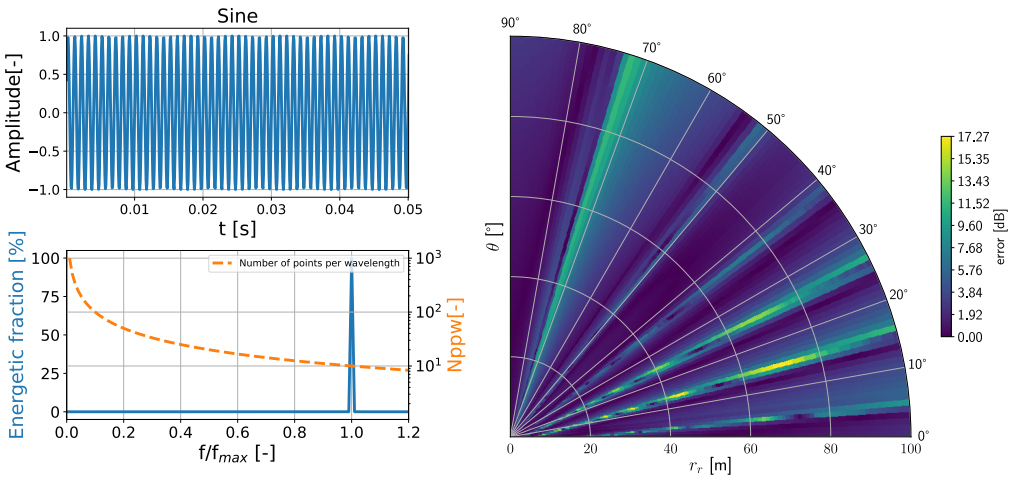

Figure 3.18. (a) Time signal according to time (top) and spectral distribution (bottom) of a sine compared to N_{ppw} (orange dashed line) according to normalized frequency. (b) Polar map of the SPL absolute error ε_{j_1,j_2} (Eq. (3.13)).

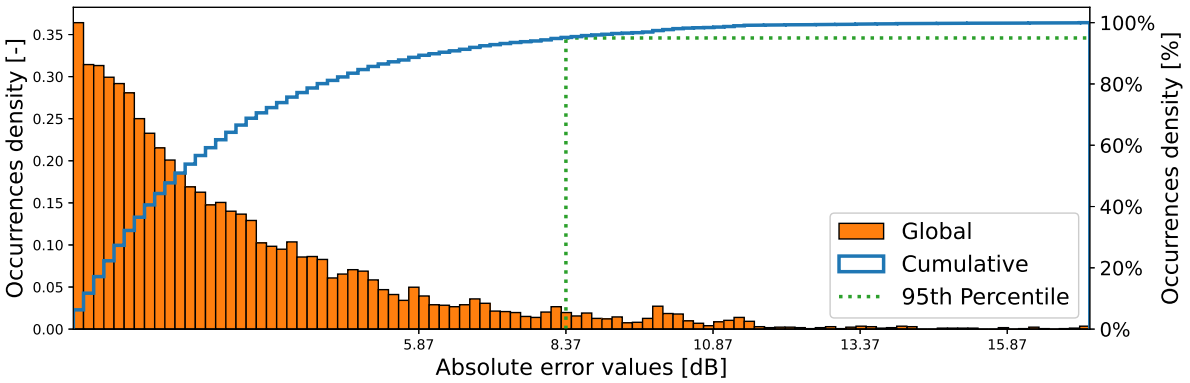

Figure 3.19. Statistical distribution of the absolute errors ε_{j_1,j_2} for the sinusoidal case.

3.4.3.e Windowed sinusoidal source

The three previous pulse cases implied broadband sources and the sine case is mostly theoretical. Now, a windowed sine is used as it is pseudo-harmonic and can be somewhat representative of birdsongs. As shown on Fig. 3.20a, most of the source energy is focused around the frequency $f_{\max}$ and has a 10-point spatial discretization. Thus, the direct wave is more likely to interfere with the reflected one. With this spectral distribution, significant misplaced interference-induced errors are generated by the numerical dispersion (up to 11.06 dB as shown on Fig. 3.20b). Indeed, at some receivers, the energy of the received signal is either increased or lost due to artificial interference patterns induced by the TLM model.

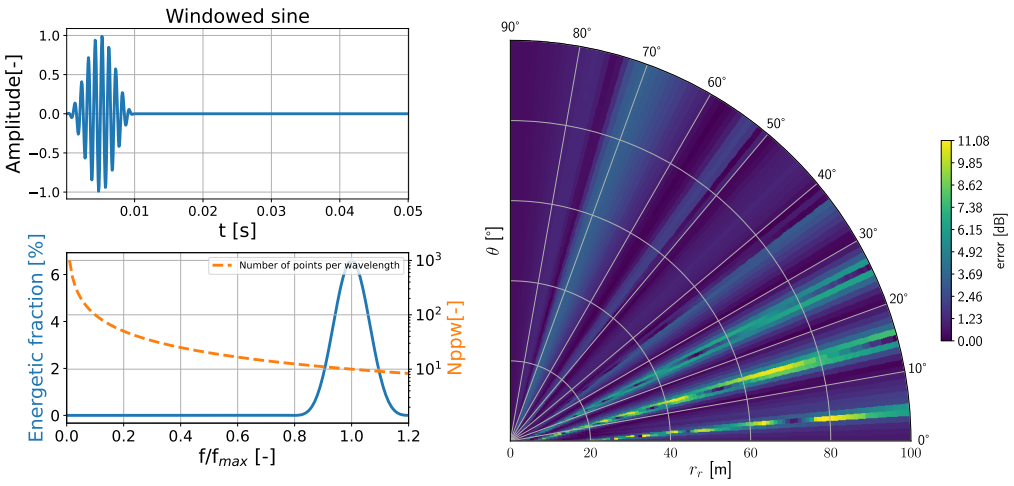

Figure 3.20. (a) Time signal according to time (top) and spectral distribution (bottom) of a windowed sine compared to N_{ppw} (orange dashed line) according to normalized frequency. (b) Polar map of the SPL absolute error ε_{j_1,j_2} (Eq. (3.13)).

In this case, the histogram in Fig. 3.21 presents a broader occurrence distribution of the errors compared to Figs. 3.13, 3.15 and 3.17. The most critical value is that 5 % of the errors are in the interval [5; 11 dB]. This value suggests that more than ten points per wavelength are needed to model the propagation of pseudo-harmonic wave packets with the TLM model, in presence of perfectly reflective boundaries.

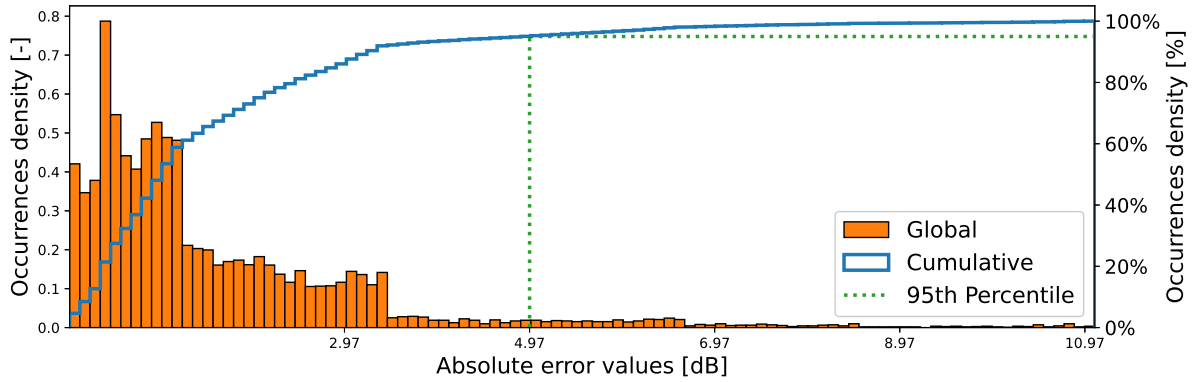

Figure 3.21. Statistical distribution of the absolute errors ε_{j_1,j_2} for the windowed sine case.

3.4.4 Windowed sine source: attenuation along receiver lines

To clarify the concept of misplaced interference patterns presented in the windowed sine case, the SPL attenuations relative to a reference microphone along three receiver lines: $\theta = [4°,\ 10°,\ 15°]$ are detailed. Fig. 3.22 helps to visualize more precisely the lines of receivers and the maxima of errors from the previous color map of Fig. 3.20b.

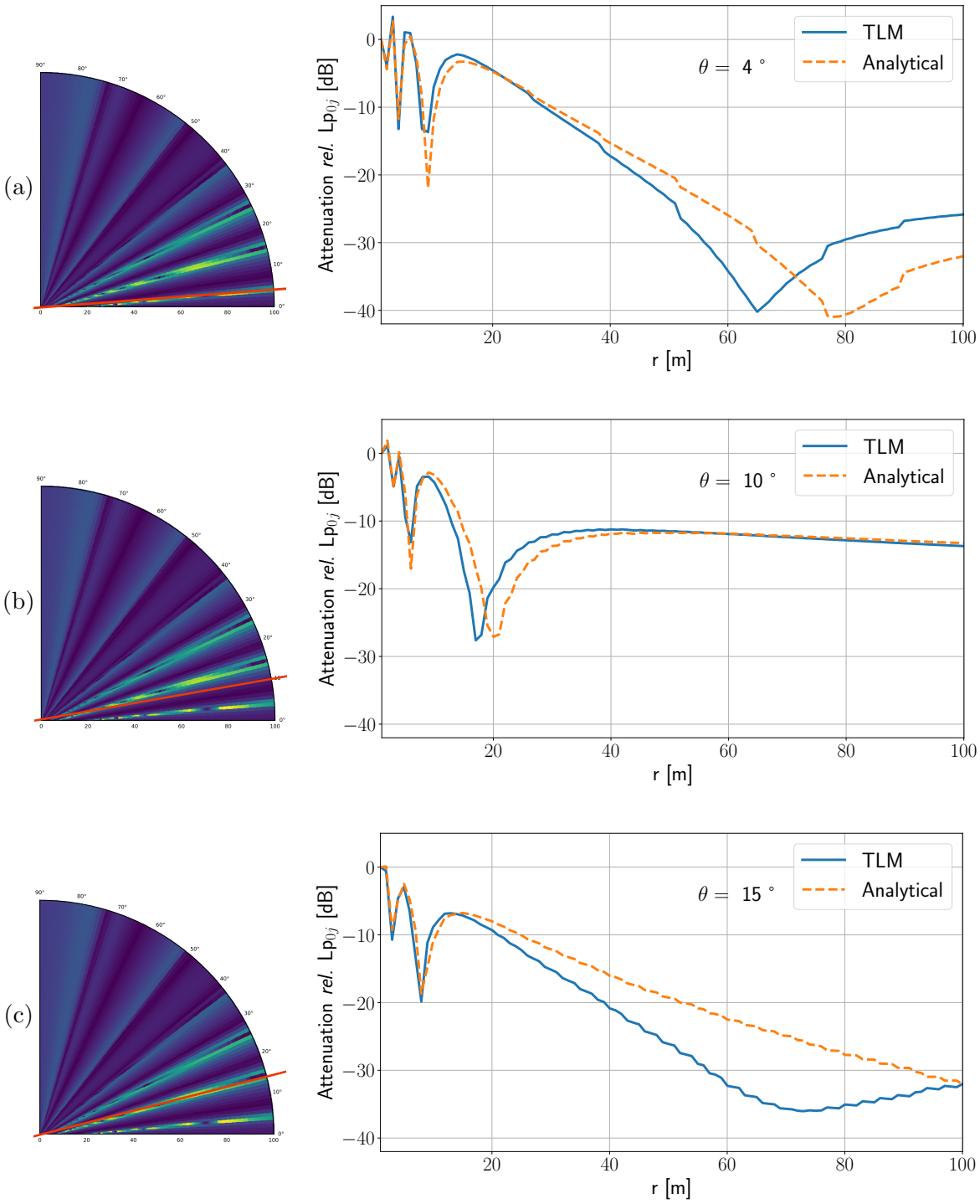

Figure 3.22. Numerical SPL attenuation relative to a reference receiver according to the propagation distance r (blue line), compared to the analytical solution (orange dashed line) for three source-receiver angles: (a) $\theta = 4°$, (b) $\theta = 10°$ and (c) $\theta = 15°$. Source located at $h_s = 2$ m and emitting a windowed sinusoidal signal at $f_{max} = 500$ Hz ($N_{ppw} = 10$). On the error maps on the left, red lines indicate the receiver lines corresponding to the SPL attenuation graphs on the right.

The "Sawtooth" effect on the attenuation profiles comes from the Cartesian discretization of the numerical domain. It does not affect the results as the effect appears for both analytical and

numerical solutions. On Fig. 3.22 (a) and (c) related to $\theta = 4°$ and $\theta = 15°$, it is confirmed that maxima of errors are due to misplacement of attenuation dips along the source-receiver distance. The line $\theta = 15°$ is the one which presents the largest gap because the third attenuation peak is simulated closer to the source than the analytical solution.

3.4.4.a Effect of source height for large frequency bandwidths, long range results

Given the previous results, longer-range scenarios, with a broader source spectrum are investigated. Pushing the model further allows the quantification of the errors in more realistic cases. SPL absolute error maps for source-receivers distances up to $\Delta z_{\max} = 120$ m and $\Delta y_{\max} = 500$ m with a maximal frequency of validity $f_{\max} = 2000$ Hz are presented on Figs. 3.23 and 3.24 for a Ricker wavelet and a windowed sine respectively.

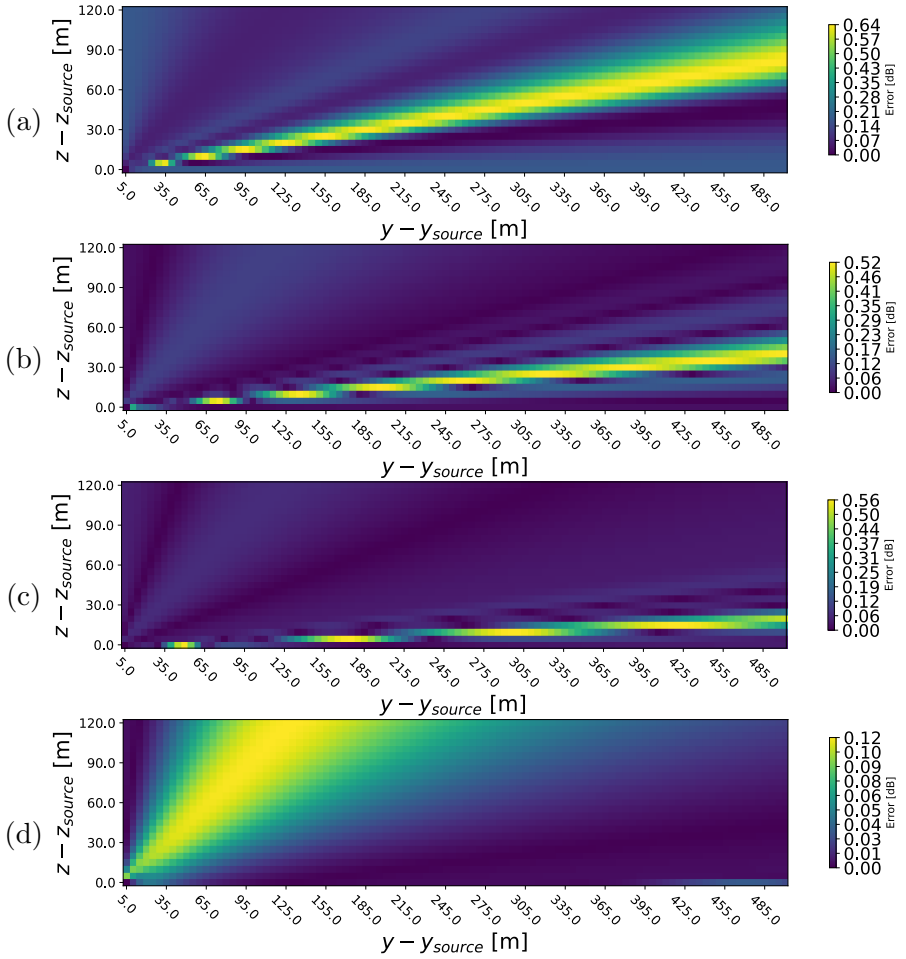

Figure 3.23. Maps of the absolute error ε_{j_1,j_2} for a Ricker wavelet source with $f_{\max} = 2000$ Hz for source heights of: (a) $h_s = 0.5$ m; (b) $h_s = 1$m; (c) $h_s = 2$ m; and (d) $h_s = 10$ m.

Fig. 3.23 shows that for an over-discretized broadband source, the errors induced by the dispersion can reach 0.64 dB in the worst source-height configuration (0.5 m here). On Fig. 3.23 (d) corresponding to $h_s = 10$ m, the visualized error is an artifact from the use of a rectangular receiver matrix and a normalization process relative to the receiver located in ($z - z_s = 0$ m, $y - y_s = 5$ m). In this case, the misplaced interference pattern is out of the figure canvas.

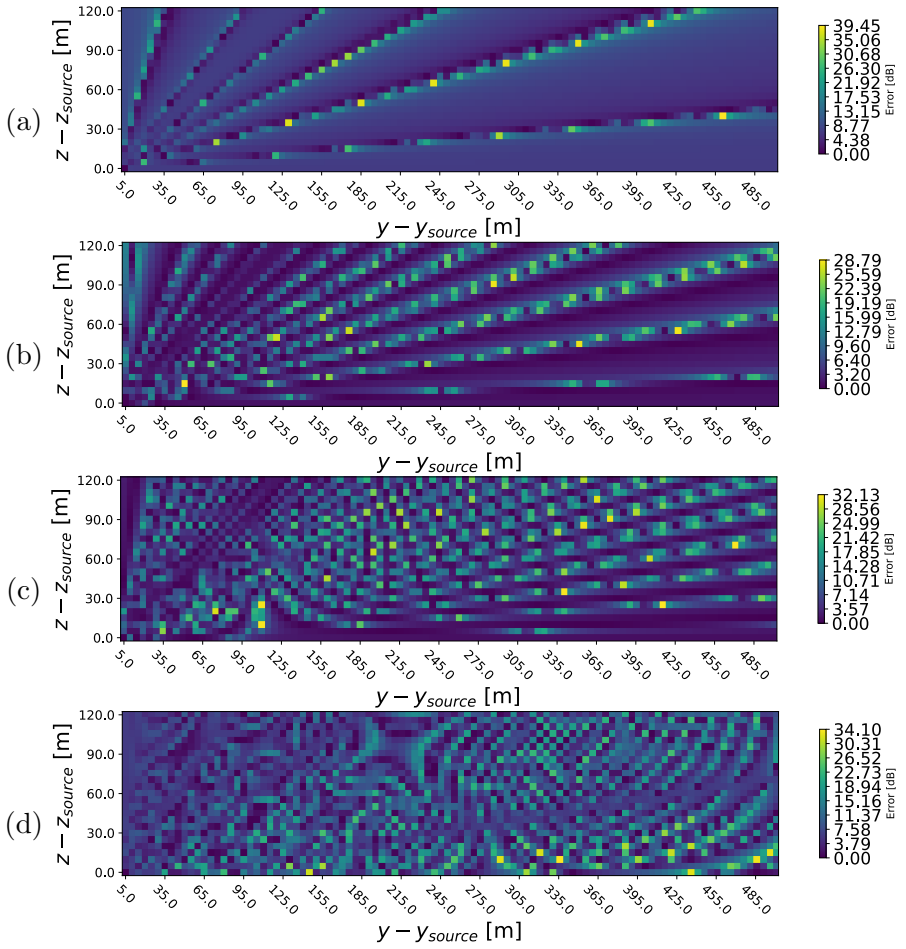

Figure 3.24. Map of the absolute error ε_{j_1,j_2} for a windowed sine source with $f_{\max} = 2000$ Hz for source heights of: (a) $h_s = 0.5$ m; (b) $h_s = 1$ m; (c) $h_s = 2$ m; (d) $h_s = 10$ m.

For more harmonic signals as in Fig. 3.24, the errors can locally rise up to 41 dB and are spatially localized. For both source types, these dispersion induced errors could be reduced by increasing the number of points per wavelength N_{ppw} but this leads to smaller spatial steps (*i.e.* more memory usage). The differences between maps (a) to (d) confirm the interfering behavior of the error and points out that the position of the source relative to the boundary has a significant impact. Indeed, the higher the source is, the more 'rays' of error are visible. For an extreme case such as Fig. 3.24 (d) with a source placed at 10 m from the ground, the spatial distribution of the error brings out its interfering behavior and the fact that dispersion leads to unwanted energy losses in the signals simulated by the TLM, even if the model itself is not dissipative.

3.4.5 Conclusion for fields with interfering waves

The results from distinct source signals emphasize the importance of the spatial discretization compared to the minimal wavelength of the study, represented by the number of points per wavelengths as a simulation parameter. The introduction of a perfectly reflective surface in the simulation domain shows that the numerical dispersion can impact the accuracy of the SPL prediction by altering the interferences between the direct and the reflected fields. In specific cases of reflection, misplaced simulated interferences appear due to the wrongly approximated phase speed of some spectral components of the wave packet. Relatedly, the link between the spatial distribution of the errors and the spectral distribution of the source has been highlighted.

One issue remaining is that reducing such dispersion-induced errors for a second-order scheme as the TLM would not be computationally efficient.

However, since a higher order of spatial integration requires a higher-order integration scheme for the boundary conditions [115], the idea of using a low-order scheme to model a complex environment needs further analysis. In addition, the use of a non-dissipative method such as TLM in multiple scatterers and source scenarios where the dispersion-induced error could be mitigated seems to be a promising and computationally efficient approach.

3.5 Numerical dispersion analysis: white noise application case

The perfectly reflective boundary case and the related conclusions (see Section 3.4) lead to consider a more realistic scenario. The analysis of potential errors brought by numerical dispersion is then considered in a case simulating a white noise source. Initially, this part was the first step toward a study on modeling road noise cases.

To approximate road noise sources, Gaussian white noise time-dependent signals were generated. A discrete-time white noise $W[n]$ is defined by:

$$E(W[n]) = 0 \tag{3.14a}$$

$$R_W[n] = E(W[k+n]W[n]) = \sigma^2\delta[n], \tag{3.14b}$$

$E()$ being the stochastic mean, $R_W[n]$ the auto-correlation function[5] and σ the standard deviation. A Gaussian white noise ($\sigma^2 = 1$) is displayed on Fig. 3.25. The primary idea was to assess the effect of numerical dispersion for each one-third octave band in order to quantify the errors in a realistic application case. However, theoretical limitations from signal processing theory tend to degrade the scientific validity of this experiment. Indeed, the time duration of the white noise affects its sinusoidal richness and thus impacts the results.

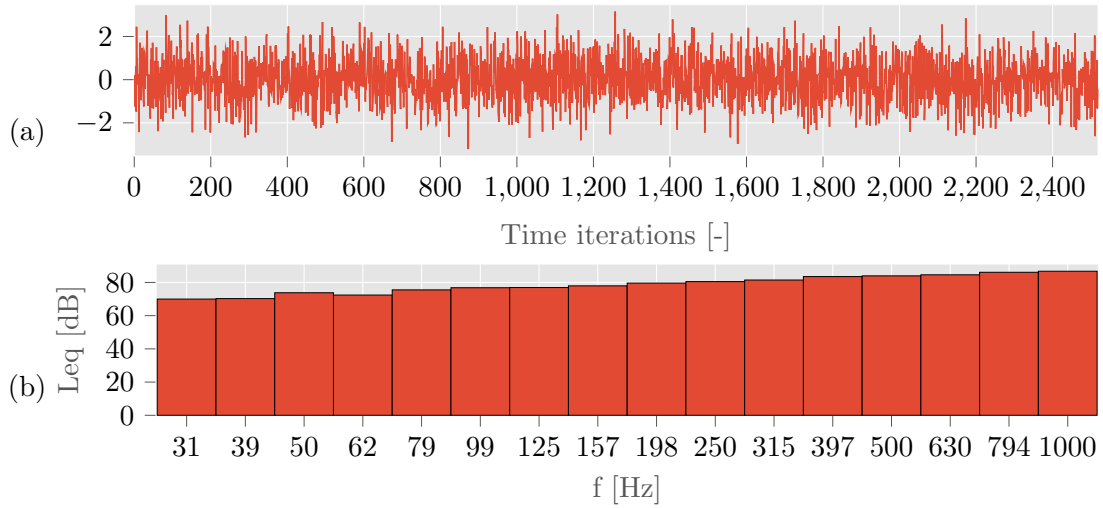

Figure 3.25. Example of Gaussian white noise signal: (a) time step values, (b) one-third octave band L_{eq} spectrum.

The filtering stages of the source signal are the following:

$$W[n] * Bi = fW_i[n] \ \textit{(first stage)}, \tag{3.15a}$$

$$fWi[n] \times H_{\text{anning}}[n] = fwW_i[n] \ \textit{(second stage)}, \tag{3.15b}$$

[5] as defined in the numpy function np.correlate()

Bi being the vector of Butterworth filters from `PyFilterbank` and $fW_i[n]$ the vector of one-third octave band filtered components. The result of the windowing process is displayed on Fig. 3.26 and shows that the Hanning window length is significant on the dynamic of the spectrum: the longer the sample, the more incoherent the source signal. Given that a coherent signal is more likely to show interference patterns when it interacts with itself, the duration of the Hanning window and therefore the duration of the simulation might impact the results. This observation, along with Fig. 3.26 reinforces the conclusion that the dispersion will create more error if the source has a more harmonic nature.

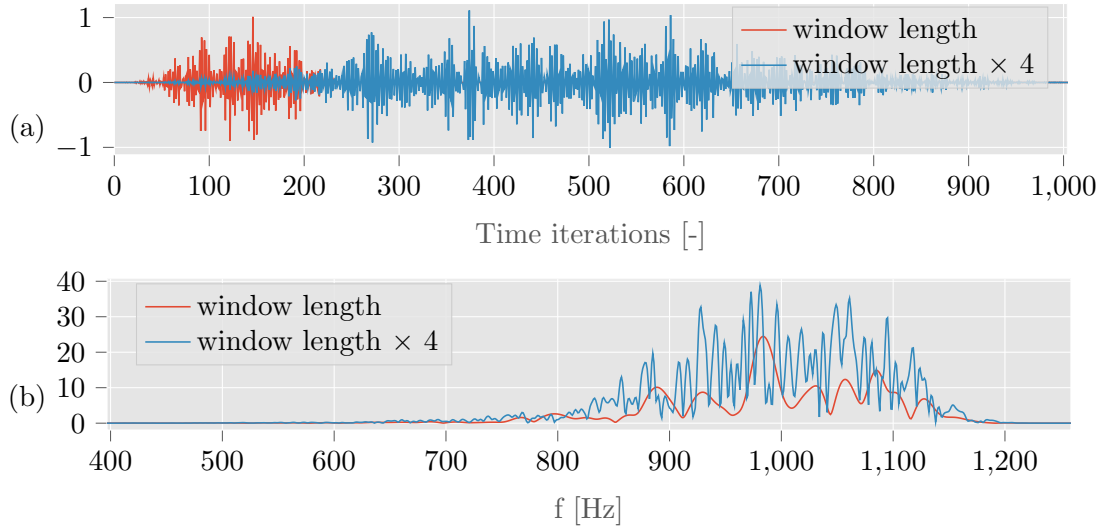

Figure 3.26. Filtered Gaussian white noise signal: (a) time step values, (b) spectrum for the nominal frequency $f_{\text{nominal}} = 1000$ Hz .

Finally, no results on the absolute SPL error are presented here, as simulation time would have an effect on the interference behavior of the incident and reflected fields. It would therefore be impossible to uncouple the contribution of this effect from that of numerical dispersion.

3.6 Chapter summary

This chapter has focused on the use of the Transmission Line Matrix (TLM) model as a solver for long-range outdoor sound propagation, quantifying the errors arising from anisotropic dispersion. Numerical aspects were extensively explored to highlight the limitations and reliability of the TLM model in various scenarios related to environmental acoustics. The findings from this chapter emphasize the significance of the number of points per wavelength as a crucial simulation parameter. Setting the right balance is essential: a high value of N_{ppw} leads to computational costs increase, while a low value compromises the frequency range of validity compared to the maximal simulated frequency. Source validation analysis revealed that at the source point, the resulting pressure is not solely determined by the input signal but is influenced by the convolution with the model impulse response.

In free-field configurations, the validity of the TLM results has been quantified by numerical experiments. Negligible errors are observed when an appropriate choice of the number of points per wavelength is made, considering that the equivalent sound pressure levels serve as the primary quantity of interest for evaluating sound disturbances in outdoor environments.

In scenarios involving interfering waves, the presence of perfect specular reflections in the model highlighted the impact of numerical dispersion on simulated sound pressure levels. Misplaced simulated interferences emerged due to the inaccurately approximated phase speed of spectral components of the wave packet. Furthermore, a correlation was observed between

the spatial distribution of errors and the spectral distribution of the source. Thus, addressing dispersion-induced errors for a second-order scheme like the TLM in a computationally efficient manner remains an open challenge.

In the context of the white noise case study, it was concluded that the impact of simulation duration and the need for source signal filtering were significant, making independent characterization of the impact of numerical dispersion challenging. Consequently, impulse simulations were favored for further investigations in this line of research.

The idea of employing a low-order scheme to model realistic complex environments warrants further analysis, as higher-order spatial integration necessitates a corresponding higher-order integration scheme for the boundary conditions. Additionally, leveraging a non-dissipative method such as TLM in scenarios involving multiple scatterers and sources is likely to mitigate dispersion-induced errors while maintaining computational efficiency.

Having successfully quantified the errors induced by numerical dispersion in the TLM model using test cases and comparing analytical solutions, the application of the model to forest environments can now be considered in Chapter 4. A comparison with in-situ measurements under real outdoor conditions should be made to characterize the reliability of the simulated sound pressure levels. In such realistic cases, more broadband sources and the use of impedance boundary conditions might reduce the errors created by numerical dispersion.

Chapter 4

TLM Applications to forests

Following the chapters dedicated to the TLM theory and the characterization of its inherent errors, this chapter presents the potential applications of the numerical method to sound propagation modeling in forest environments. Going further than previous research on this topic that included a comparison of TLM simulations with measurements in a semi-anechoic room [26, 28], this chapter represents a step towards comparing the model with real data from in-situ measurements. It provides insights into possible methodologies and required information on the propagation medium.

The first part of the chapter focuses on three-dimensional geometric scene generation, as the methods implemented are tailored to the available data. Subsequently, the use of virtual forests generated from the "*Risoux*" forest statistical data is explored, and TLM simulations applied to this scenario are presented. Finally, the methodology employed to compare TLM sound propagation simulations with an in-situ measurement campaign in the "*Nouragues*" forest is detailed, along with the results of the comparison.

4.1 Forests geometric modeling

Before simulating sound propagation within a forest, generating a geometric scene is necessary. Thus, this section addresses the underlying hypotheses and methodologies implemented to create forest meshes, which serve as input data for the TLM model. In this doctoral work, meteorological effects such as wind or temperature gradient were omitted as they can be considered negligible under the canopy (see Section 1.3). As for the geometric elements included in the simulation domains, foliage and stems were neglected in favor of tree trunks and ground impedance. Indeed, they are the main influencing factors that contribute to the sound field complexity in forest acoustics within the frequency range reachable by the TLM model when applied to the scenarios described below.

4.1.1 Trees description

In order to simulate sound propagation in forest media, the TLM model requires specific geometric data. The parameters needed to accurately describe the trees in the considered forest (diameter, height, *etc.*) are listed in Table 4.1. However, despite its optimized implementation, the model's frequency limitation due to current computational costs has necessitated a simplification in tree modeling (Eq. (3.1)). Indeed, 3D simulations have been performed up to 1500 Hz in the designed calculation domains, leading to approximating trees as cylinders. This simplification reduces the geometric parameters needed to describe the trees in the geometric model, since they therefore have no conical shape, stems nor leaves.

From an experimental perspective, this approximation also simplifies the data-collecting process, as it reduces the geometric description of trees to four parameters. Indeed, information on forest geometries is scarce and often not as straightforward as the discrete parameters mentioned in Table 4.1.

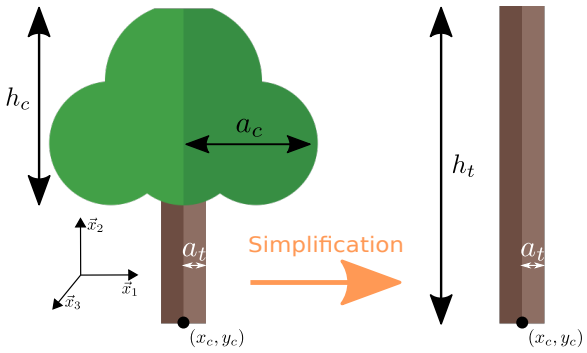

Figure 4.1. Simplification of tree descriptive parameters.

Parameter	Formalism
Trunks center coordinates	x_c, y_c
Tree height	h_t
Trunks radius	a_t
Canopy radius (approx.)	~~a_c~~
Canopy height	~~h_c~~
Tree species	"species"

Table 4.1. Geometric parameters' description. Canceled parameters are the ones not considered in the TLM simulations.

Additionally, as indicated in Table 4.1, the tree's species provides information about the type of bark covering the trunk. Unfortunately, little is known about tree bark acoustic parameters, even if refining the model with precise impedance boundary conditions for the tree trunks could provide valuable insights about their effect [91].

4.1.2 Mesh generation

As briefly mentioned in Section 3.1, a data file is the first input for the mesh generation process. For forests, it contains the locations of the trees x_c, y_c as long as their radii a_t. It is then processed by a Computer-Aided Design (CAD) software[1] to generate triangular sub-meshes of cylinders above an impedance plane embedded in a virtual box, as shown on Fig. 4.2a. The resulting mesh is then voxelized and a matrix storing the scene characteristics is created (Fig. 4.2b). Afterward, the nodes of the mesh that compose the Adapted Matched Layers (see Section 2.9) are specified to simulate open boundary conditions (all faces of the virtual box except the ground).

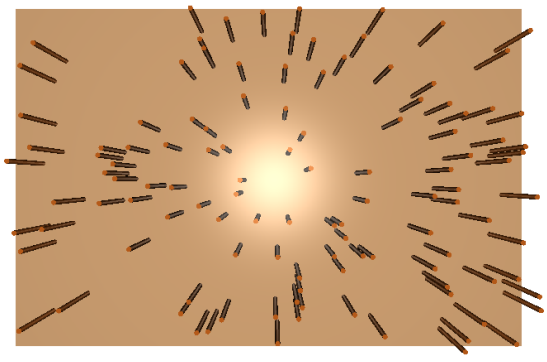

(a)

Figure 4.2. Meshing process description: (a) triangular mesh output, (b) voxelization output showing the face attribution on three slice planes along the main axes (-1) outside (0) fluid (1) reflective condition (9) index of impedance condition stored in the database (see Appendix A).

[1] In this case, the software is FreeCAD API controlled by Python code.

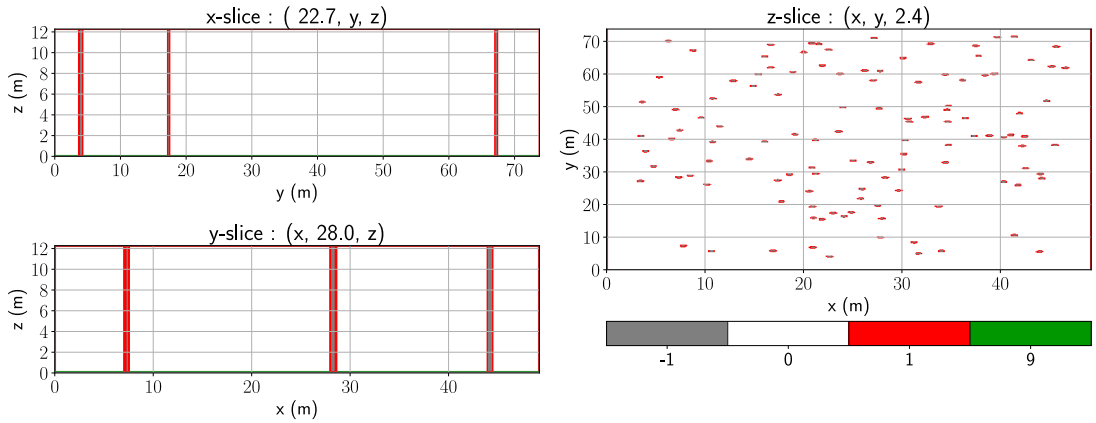

(b)

Figure 4.2. (continued) Meshing process description: (a) triangular mesh output, (b) voxelization output showing the face attribution on three slice planes along the main axes (-1) outside (0) fluid (1) reflective condition (9) index of impedance condition (see Appendix A).

To use this implementation, tree positions must be known, and two solutions were used: (*i*) generating positions with distributions based on statistical data from forestry, and (*ii*) integrating real geometric forest in-situ surveys that accurately describe the trunk positions.

4.1.3 Impedance characteristics

The impedance parameters used to describe the ground or the trunks were obtained from the literature [6] or Kundt's tube measurements that have been made at the UMRAE laboratory on three samples of oak bark. Other literature data that use mechanical properties to calculate air flow resistivity and porosity have also been considered [119]. The sets of parameters correspond to the ones introduced in Section 1.4.4 and are listed in Table 4.2. The "slit-pore" impedance model is used to calculate the complex impedance out of the parameters as it seems to be the most adapted to describe barks and forest grounds [6, 42].

Ground parameter	σ_0 $[kPa.s.m^{-2}]$	Ω $[-]$
#10, table VII [6] pine forest	102.5	0.58
34, table VIII [6] beech forest	22.5	0.50

(a)

Bark parameter	σ_0 $[kPa.s.m^{-2}]$	Ω $[-]$
Oak bark measurements	50.00×10^3	0.5
Test value (more absorbing)	10.00×10^3	0.5

(b)

Table 4.2. Parameters for "slit-pore" (semi-infinite) model: (a) Ground parameters, (b) Bark parameters.

An airflow resistivity value for pine bark from literature input [119] was initially considered as a simulation parameter. However, the value of $\sigma_0 = 35.54\ kPa.s.m^{-2}$ seems low and more comparable to the values expected for a very absorbing material such as snow. Moreover, when the normal incidence absorption coefficient is calculated, the oak bark measurement parameters are more consistent with the values found in the literature, namely: $\alpha \leq 0.1$ for frequencies up to 2000 Hz [91]. A test value is then used (Table 4.2b) as a rough estimation for a more absorbing bark type while keeping consistency with the values from the literature.

Unfortunately, no measurements of ground parameters are available for the Nouragues or Risoux forests. Values from Table 4.2a are then used in the simulations described in the Sections 4.2.3 and 4.3.4.

With the generation of the geometric scene and the main influencing parameters addressed, the following sections will describe applications of TLM simulations within either generated (Section 4.2) or realistic (Section 4.3) forest geometries.

4.2 Application to statistically generated forests

Two applications case are addressed in this section: an analysis of the multiple scattering effect due to tree trunks based on tree distributions (Section 4.2.2), and the generation of sound pressure level maps for qualitative evaluation of the forest sound field (Section 4.2.3). But first, the generation process of tree positions from statistical data needs to be introduced.

4.2.1 Generated forests from statistical data

Artificial forests with pseudo-realistic features are constructed based on the overall characteristics of the "*Risoux*" forest, French Jura. The numerical generation of artificial forests ("meta *Risoux*") involves using a random point process with Poisson's distribution and overlapping avoidance, as elaborated in the previous Ph.D. thesis on this subject [26] (p.78-80).

As shown in Fig. 4.3, three point processes were used to generate forests: a Complete Spatial Randomness (CSR), a clustered and a periodic distribution. The characteristics of the forest are summarized in Table 4.3 and were obtained from census reports of breeding avifauna associated with the high altitude Jura forests within the dB@Risoux project[2].

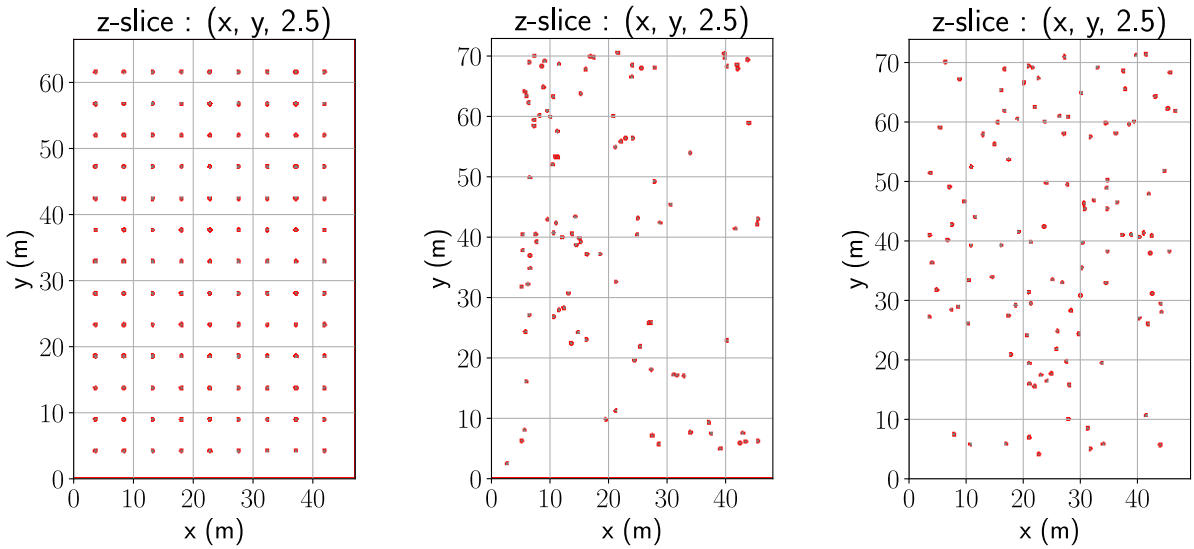

Figure 4.3. Cross-section at 2.5 m high of 3D forest media generated by three different point process distributions: (a) periodic, (b) clustered, (c) CSR.

Averaged values were used for tree heights h_t, and tree radii a_t were calculated from the mean Diameter at Breast Height (DBH), an indicator used to assess the diameter of a tree at approximately 1.3 m [53]. The forest report indicates that 67% of the area is composed of conifers, mainly spruce and fir, and the ground is a herbaceous ground cover.

[2]Website of the project: https://ear.cnrs.fr/dbjura/

$DBH_{average}$ $[m]$	Occupancy $[trees.m^{-2}]$	h_t (average) $[m]$
0.32	0.0374	13.05

Table 4.3. Risoux forest average characteristics from reports.

4.2.2 Effect of boundary conditions on the surface of tree trunks

2D simulations were performed with different boundary conditions on the trunk surfaces. The results serve to analyze to which extent the impedance conditions describing the bark impact sound propagation in comparison to perfectly reflective boundary conditions. The objective is to isolate the multiple scattering effect on trunks from the ground effect. Thus, a 2D slice of an artificial forest based on data from Section 4.2.1 is considered with 400 receivers at distances of 1 m up to 41 m from a Gaussian pulse source. The results for three different distributions of trees are displayed on Fig. 4.4 with two different sets of impedance parameters from Table 4.2 compared to the perfectly reflective case.

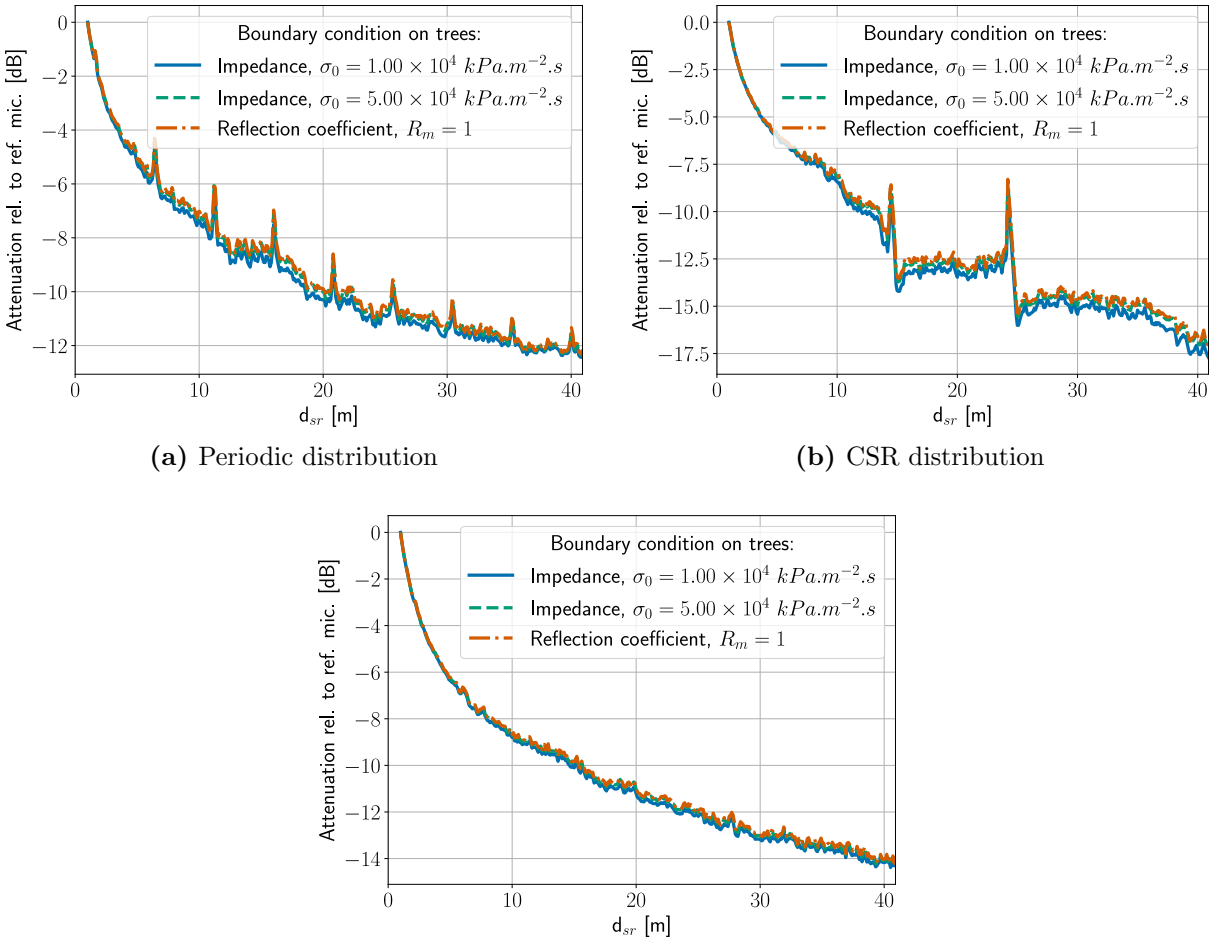

(a) Periodic distribution

(b) CSR distribution

(c) Clustered distribution

Figure 4.4. Global attenuations relative to a reference microphone at 1 m from the source for different tree distributions and different boundary conditions, $f_{\max} = 2000$ Hz, in 2D (no ground effect): (a) periodic distribution, (b) CSR distribution, (c) Clustered distribution.

The main result out of Fig. 4.4 is that, for the considered frequency range ($f \leq 2000$ Hz) and propagation distance (up to 40 m), using an impedance boundary condition for the trunks

with a high flow resistivity as measured for the oak bark (Section 4.1.3) is equivalent to using a perfectly reflective condition. Thus, as it is more computationally expensive to use impedance boundary conditions than perfectly reflective ones, the latter can be assigned to trunk faces when performing 3D simulations. Additionally, the observation that the CSR distribution is globally the most attenuating configuration compared to the periodic and clustered ones confirms the results exposed in previous work [26].

4.2.3 SPL maps generation in generated forests

This section investigates the potential generation of equivalent SPL maps using the TLM method. For this purpose, simulations were performed on a 3D realization of a part of the "meta *Risoux*" forest. The considered domain is 45-meters wide, 70-meters long and 12-meters high, with the upper part of the trees included in the AML layer. The simulations were performed using two different source signals (see Section 3.2). A Gaussian pulse signal ($f_{\text{max}} = 300$ Hz) and a sinusoidal source ($f_{\text{source}} = 250$ Hz and $N_{\text{ppw}} = 12$) emitting during the entire simulation duration (0.18 seconds) in order to approximate a steady state. The sinusoidal source test is a step toward making the results more comparable to those obtained with ray-tracing methods. Following this philosophy, an example of a simulation performed with a model based on CNOSSOS-EU is presented in Appendix C.

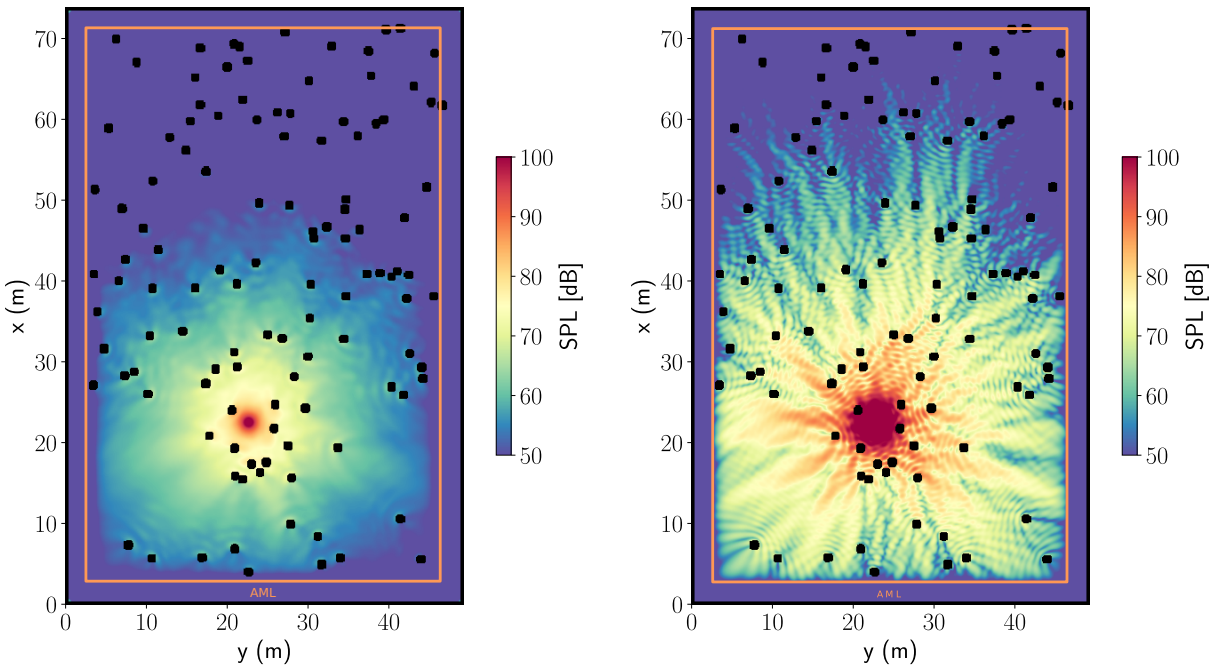

(a) Gaussian pulse source **(b)** Sinusoidal source

Figure 4.5. Equivalent sound pressure level (SPL) maps (horizontal slice at 1.5 m above the ground) from TLM simulations for $f_{\text{max}} = 300$ Hz, 10 N_{ppw}: (a) Gaussian source, (b) Sinusoidal sound source emitting during 0.18s at $f_{\text{source}} = 250$ Hz.

Fig. 4.5 displays interference features that are specific to wave-based methods, even when a less coherent source with a broader frequency bandwidth as a pulse is used. To compare the difference between the sources and the sound pressure levels they induce in the domain, the pulse amplitude should be normalized with the energy ratio of the source signals. However, it is displayed without normalization here, in order to show that time-domain methods should be used carefully when generating SPL maps.

Finally, the main outcome of this section is the possibility to assess the effect of given low-frequency sources in a statistically generated forest. While remaining preliminary, it could

be seen as a tool to improve knowledge on sound fields within forest environments. Indeed, these results could be used to calculate the detection space of a source by computing the signal-to-ambient-noise ratio in the simulation domain. This latter observation is inspired by the discussion brought by literature entry [70] that proposed a method to calculate detection distances in forests.

Now, the reliability of TLM simulation results in comparison to real in-situ acoustic measurements needs to be evaluated.

4.3 Comparison with Forest in-situ measurements

This section addresses a comparison between TLM simulation results and in-situ measurements from an experimental campaign conducted by a team of the *Institut de Systématique, Évolution, Biodiversité* (ISYEB), French National Museum of Natural History (MNHM) [70]. The campaign was conducted at the 'Nouragues'[3] CNRS scientific station, French Guiana. To perform the comparison, a systematic series of steps were followed. These include the numerical reproduction of the experimental scene, the description of the source and microphones, the configuration of the simulation setup and the post-processing of the measurements.

The measurements consisted in recording audio signals at different distances from a source emitting a sound sequence composed of various types of successive signals (white noise, sweep, etc.). The source-receiver distance was modified between each emission sequence from 0.5 m to 100 m by displacing the microphone along a linear transect (stretched rope). The GPS positions of the source and microphone were recorded for each source-receiver configuration. According to the analysis made by the ISYEB team, the useful signals for which the signal-to-noise ratio is satisfactory are limited to a maximum source-receiver distance of 40 m [70].

To reproduce the measurement conditions and maximize the reliability of the comparison, strong hypotheses were made, both regarding the spatial reconstitution of the propagation medium and processing of the recorded and simulated signals. These hypotheses are detailed in the Sections 4.3.2, 4.3.3 and 4.3.5. But first, the geometric dataset used to describe the trees is introduced in Section 4.3.1.

4.3.1 Data from geometric forest surveys

As sound recordings were available, the forest close to the CNRS Nouragues research station was chosen to validate simulations. Moreover, the Evolution and Biological Diversity laboratory (EDB)[4], Toulouse III University agreed to provide an impressive dataset of tree localizations and identifications from the COPAS project. Thus, geometric data from tree inventories were used [25]. This dataset comprises 1851 trees with radii $a_t \in [0.016 - 1.43]$ meters, as displayed in Fig. 4.6.

[3]Website of the Nouragues nature reserve: http://www.nouragues.fr/
[4]EDB website: https://edb.cnrs.fr/

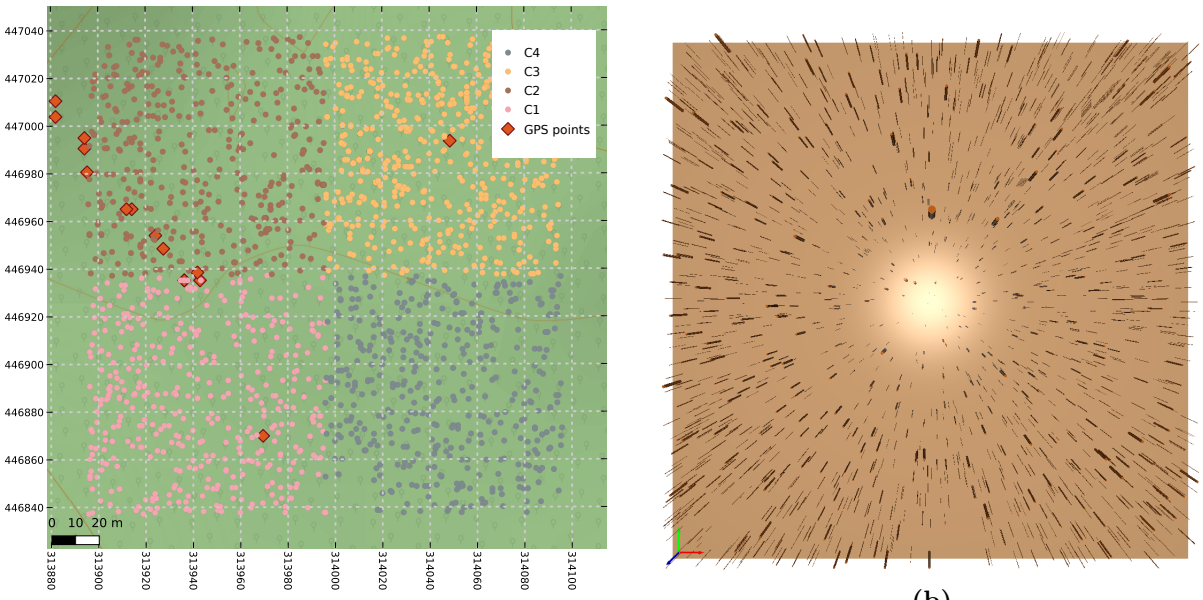

(a) (b)

Figure 4.6. Tree inventories of Nouragues nature reserve, French Guiana: (a) Map of the tree inventories in coordinates from projection `EPSG:2972`, four tree plots are represented (C1, C2, C3, C4), (b) Mesh of the 1851 trees composing the four plots.

In the dataset, the trees are separated into four plots denoted C1 to C4. They are described by their trunk position relative to a common position, their DBH, their plant family and their species name. As the reference position of the trees is not specified in the dataset, an assumption was made regarding that matter (see Section 4.3.2 below).

4.3.2 Numerical reproduction of the experimental site

As explained above in Section 4.3.1, tree localizations in four plots of the COPAS were used to generate forest meshes. The tree localizations available are described with a local coordinate system $(x_{\text{copas}}, y_{\text{copas}})$ and no GPS reference. Fortunately, the GPS position of one of the trees was recorded, allowing both the trees and the microphones to be placed in a geographic coordinate system (GCS) (see Fig. 4.7a).

However, with only one geometric reference available, a strong hypothesis was made: the x-axis of the tree positions corresponds to the east-west axis and the y-axis to the north-south axis of the local GCS. After replacing the GPS coordinates of the microphone in the $(x_{\text{copas}}, y_{\text{copas}})$ system, the accuracy of the GPS points (blue dots in Fig. 4.7b) was questioned since they do not appear to be placed every 10 m along a 100 m linear transect. The hypothesis is that the GPS accuracy in the rainforest is not reliable. Therefore, another geometric approximation process, shown on Fig. 4.7b, was applied to the data: estimated microphone positions are placed every 10 m along a regression line between the GPS positions.

Then, a rectangle area around the source and the four first microphones is created with a contour (dashed red line in Fig. 4.7b) 15 m away from the source and last receiver in the transect axis and 20 m away in the orthogonal axis. This rectangle represents the trees to consider in the simulation, its size is a trade-off between computational costs and the considered area of forest. Finally, the trees, source and microphone locations are rotated in the simulation setup coordinate system displayed on Fig. 4.7c, alongside the generated mesh (Fig. 4.7d).

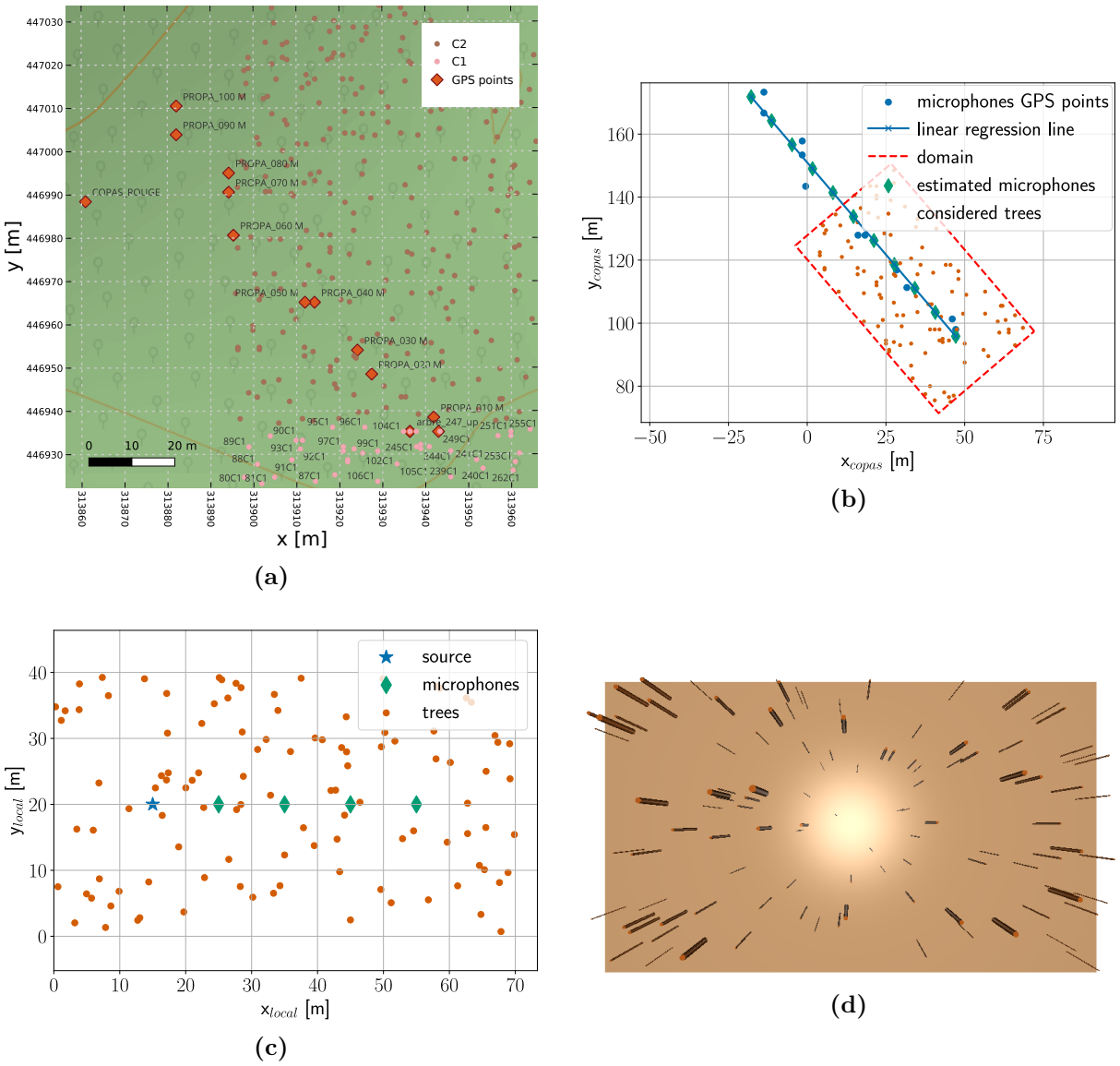

Figure 4.7. Geometric reproduction process of the experimental scene: (a) geographic positions (`EPSG:2972`) of the trees (dots) and experiment GPS points (orange diamonds), (b) regression line (blue line) process and tree area (red dashed rectangle) creation, (c) source (blue star) and microphones (green diamonds) positions in rotated coordinate system, (c) generated mesh of the simulation scene.

4.3.3 Source and receivers specifications

4.3.3.a Experimental source and receiver

The sound source used during the measurement campaign is a JBL Xtreme 2 loudspeaker. Further details regarding its characteristics and calibration can be found in Appendix B of reference entry [70]. As for the emitted signals, the sweeps (linear chirps here) were chosen for comparison instead of pure tone or white noise signals. This choice was made based on the results and observations from Sections 3.4 and 3.5: white noise and pure tone signals would have required either excessively long simulation times or a more refined mesh discretization (increase of N_{ppw}), respectively. Therefore, the emitted sweep signals of 1.1 s, with linear frequency modulation ranging from 0 to 20 kHz were elected for the comparison with the TLM model simulations.

The recording unit used as microphone during the measurement campaign is a class 1 sound level meter (SVANTEK 977A). It recorded the audio signals during the whole experiment at the microphone positions described in Section 4.3.2.

4.3.3.b Numerical source signal

The source signal used in the simulations is a low-pass filtered linear chirp to maintain consistency with the experiment while using the TLM model at the highest possible maximum frequency. As highlighted in Fig. 4.8, the cutoff frequency of the filter corresponds with the maximal frequency of the simulation $f_{\max}$. For the maximal frequencies of simulation reachable, filtering the signal allows to keep the simulation time at values that do not imply too long computation times ($t_{\text{end}} \leq 0.35s$).

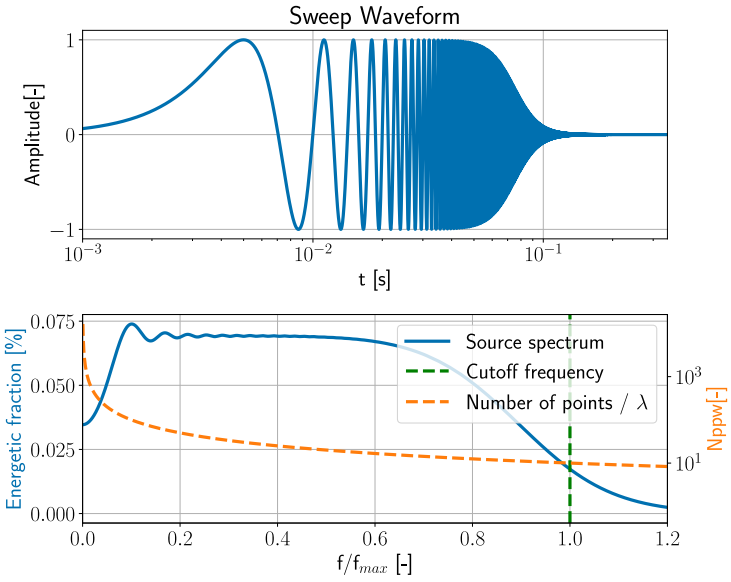

Figure 4.8. Time signal according to time (top) and spectral distribution (bottom) of a filtered (fourth-order low pass Butterworth filter) Sweep compared to N_{ppw} (orange dashed line) according to normalized frequency ($f_{\max} = 1500$ Hz).

4.3.4 Simulation setup for the 'Nouragues' nature reserve

Fig. 4.9 and Table 4.4 detail parameters used for the TLM simulation. As shown on Fig. 4.9, the trees' height is set equal to the computational domain one and the uppermost 3 meters of the trees are embedded in the adapted match layer. This choice was made to limit the computational costs of the simulation, as the sources and receivers are located at 1.5 m above the ground.

In the absence of information on the nature of the soil (its airflow resistivity, its porosity, *etc.*), the specific parameters of a pine forest ground were retained to model the ground acoustic impedance (Table 4.2a) [6].

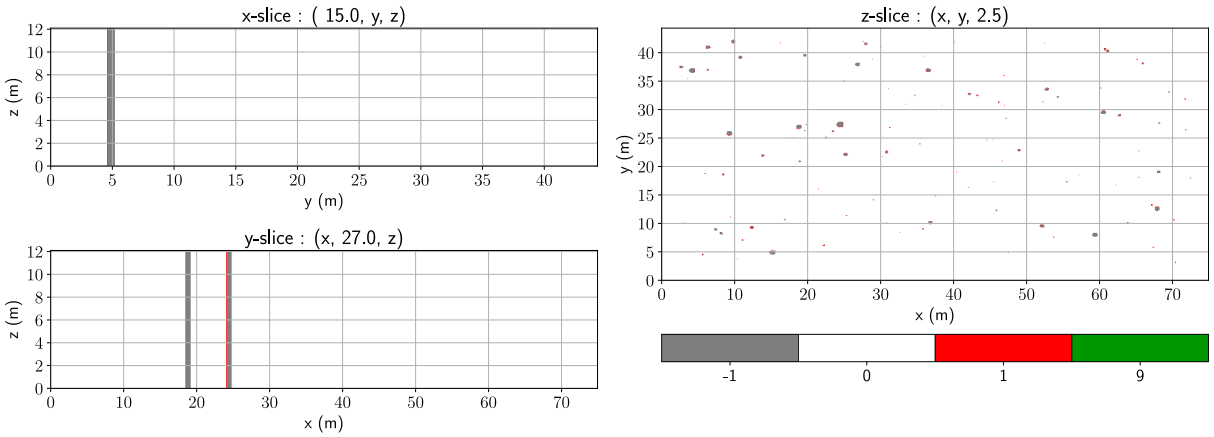

Figure 4.9. Slices of the 3D simulation setup for the Nouragues experiment reconstitution with displayed boundary conditions indexes (see Fig. 4.2 and Appendix A).

$\Delta\ell$ (m)	Δt (s)	$N_x \times N_y \times N_z$	Memory (GB)	t_{comp} (h)	$r_{\max}/\lambda_{\min}$
2.29e-02	3.90 e-05	3265 × 1931 × 527	6.65 Gb	97.25	174

Table 4.4. Configuration for the 3D simulation setup with $f_{\max} = 1500$ Hz, $N_{\text{ppw}} = 10$ and the source-receiver distance $r_{\max} = 40$ m. $N_x \times N_y \times N_z$ are the numbers of spatial points in the respective axes. The memory usage is given for a float32 numpy array. t_{comp} is the computation time needed for this configuration, distributed over two GPUs (Quadro RTX 5000 cards).

4.3.5 Measurement post-processing

The maximum validity frequency of TLM simulations reached on the HPC cluster is $f_{\max} = 1500$ Hz. Thus, post-processing of the recorded audio was performed to reliably compare experimental and numerical results. Additionally, the recorded signals exhibit a poor signal-to-noise ratio (SNR) below 100 Hz and the ambient noise level in the forest combined with the emission level of the source only allows the measurements to be used at distances below 40 m. Subsequently, experimental signals were filtered by a fourth-order Butterworth band-pass filter of range [120 - 1500 Hz]. An illustration of this process is displayed on Fig. 4.10 for both the sweep and background noise signals at 10 m from the source.

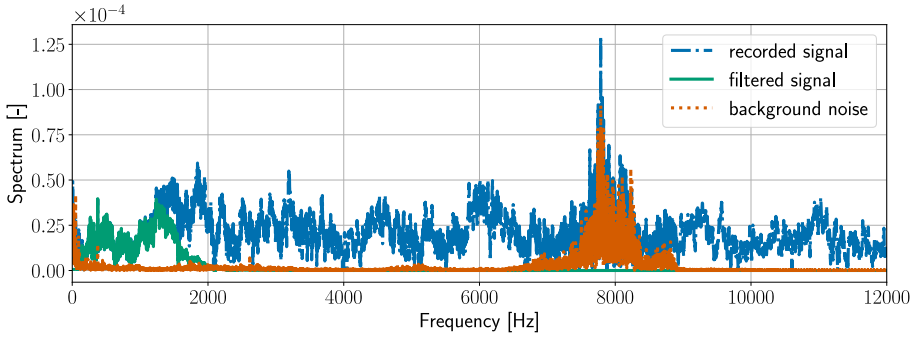

Figure 4.10. Spectrums of recorded sweep signals at 10 m from the source before filtering (blue dash-dotted) and after filtering (green). Ambient noise (orange dotted)

4.3.6 Comparison of the attenuation relative to a reference microphone

Following the hypotheses and processes described in Sections 4.3.2 to 4.3.5, the sound attenuation relative to a reference microphone at 1 m was calculated for both numerical and experimental results. The background noise level was subtracted from the experimental attenuations, using the audio recorded before the sweeps emissions.

For the experimental results, error bars were calculated to include the standard errors from the mean estimation and the use of a class 1 sound level meter. Three sequences of four successive sweeps were emitted at every distance from the source during the experiment, allowing a better estimation of the experimental attenuation. Therefore, the standard errors on the estimation of the mean were computed with Student's coefficients corresponding to a 95 % confidence level for a two-tailed distribution. The value of 1.5 dB was calculated for the standard error on the sound level measurements, according to the XP S 31-115 standard [48]. Finally, the comparison between the numerical and the experimental relative attenuations is displayed on Fig. 4.11 for two different ground types, representative of pine and beech forests, respectively.

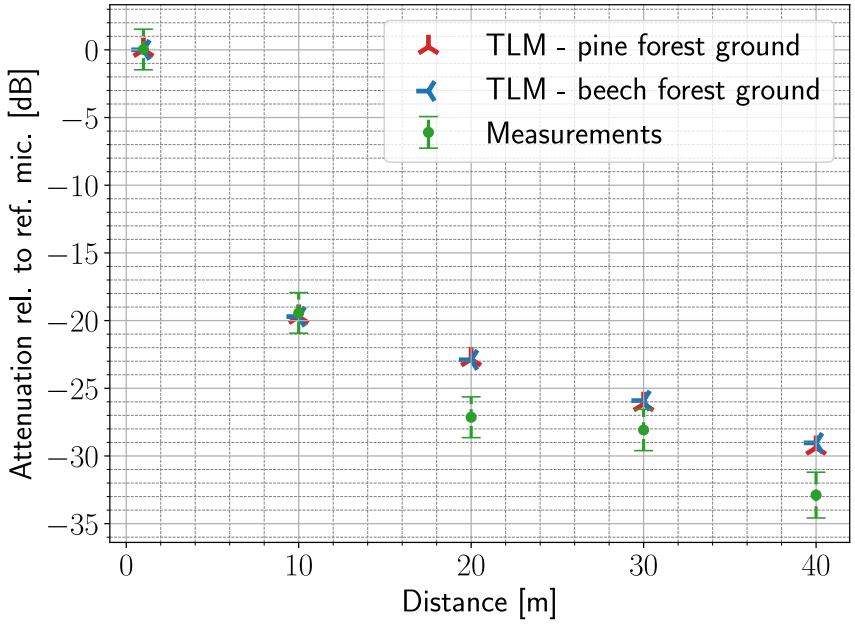

Figure 4.11. Results comparison for a simulation with $f_{\max} = 1500\ Hz$. Attenuations relative to a reference microphone at 1 m from the source: TLM results (triangle markers) for pine forest ground (orange) and beech forest ground (blue), in-situ measurements (green dots) with experimental error bars.

Although four spatial points (each with 12 experimental recordings) provide little information to make a meaningful comparison, Fig. 4.11 shows that the TLM model underestimates the forest attenuation overall. Indeed, the attenuation calculated at 10 m from the source might be mostly a contribution from the direct field and the ground reflections. Thus, the match of the results is logical and comforting about the hypothesis on the ground impedance parameters used.

For the receiver located at 20 m, a difference of 5 dB in attenuation is observed. Similar behavior is noted at the other receivers, with slightly lower values: 2 dB at 30 m and 3 dB at 40 m. These discrepancies could be due to the numerous approximations made in the geometric positions of the trees and microphones when reproducing the experimental scene and to uncertainties in influencing parameter values (*e.g.*, ground impedance). Therefore, running more simulations with variations in ground boundary conditions and regression line azimuth could improve the comparison by providing numerical error bars.

In addition, it can be brought that the global behavior of the attenuation is close to -6 dB per doubling distance, as it would be in free field with geometric spreading only. Yet, it is not observed for the numerical results between the points at 10 m and 20 m, which display an attenuation of -3 dB for a doubling of source-receiver distance. This behavior could be due to local interference patterns and/or to a barrier effect of the trees, highlighting the need for a larger number of measurement points.

Additional results with frequency analysis are available in Appendix D.

4.4 Chapter summary

In this chapter, some applications of the TLM model in the context of forest acoustics were explored. Simulations of sound propagation in forests environment were described and analyzed. The applicability and performance of the TLM method were evaluated for such scenarios.

The first part of the chapter focused on the geometric modeling of forests. Various techniques for generating realistic and statistically generated forest geometries were detailed, along with the crucial consideration of accurate tree position data obtained from field surveys. Additionally, the introduction and discussion of impedance parameters from the literature provided an overview of the currently available data.

The applications of the TLM method to simulate sound propagation in "meta *Risoux*" generated forests provided insights into their potential use, notably by analyzing the effect of bark impedance in simulations below 2000 Hz and within 40 m. It was concluded that tree trunk surfaces can be modeled with perfectly reflective boundary conditions in this frequency range. Another application of modeling sound propagation in generated forests was presented as a preliminary attempt to generate SPL maps with the TLM method.

Then, the TLM method was applied to a realistic case using experimental data from a measurement campaign in a forest part of the Nouragues nature reserve, French Guiana. It enabled a comparison between simulations and experimental results. The methodology used to carry out the comparison was detailed, as the strong and original hypotheses that were formulated. While discrepancies were observed between the simulations and measurements, the overall agreement is encouraging, demonstrating the TLM method's potential as a reliable tool for forest acoustics.

Overall, the accuracy of the simulated results is subject to the precision of input data, such as tree positions and acoustical properties of the boundary conditions. Additionally, certain simplifications in the model and assumptions made during simulations may affect the results. A parametric study on the methodology presented in this chapter would represent a meaningful contribution toward the understanding of the model. For instance, performing more simulations with variations in the regression line azimuth and other ground parameters would provide numerical error bars and thus more insight into the comparison.

Finally, this chapter demonstrated the need for accurate geometric data, in-situ sound measurements and ground impedance characteristics to better assess the potential of the TLM method in simulating sound propagation in forests. An improvement in the method efficiency and memory consumption would also represent an opportunity to increase the maximal frequency of the simulations, hence the relevance of the comparisons to in-situ measurements.

General conclusion

In this document, the work carried out during three doctoral years at the Joint Research Unit in Environmental Acoustics (UMRAE) is presented. This research project is placed in a biodiversity crisis context and aims to evaluate the potential assistance of numerical methods for passive acoustic monitoring in forest environments. The method proposed to achieve this goal is the development pursuit of a wave-based three-dimensional sound propagation numerical model able to integrate approximations of complex phenomena that occur in forests (ground absorption, multiple scattering on trunks, interferences, *etc.*). To ensure the best use of the chosen method, its limitations have been investigated, leading to insights into its further applications and developments.

1 Results synthesis

In the literature review presented in the first chapter, special attention was given to describing the complexity of the physical phenomena that occur during sound propagation within forest media. As an attempt to showcase the diversity of this domain of acoustics, existing analytical and numerical methods were presented through references and overviews of the underlying theory. The major highlights of this state-of-the-art are the description of frequency-based and time-domain models, the mention of the growing development of hybrid numerical models and a personal proposition to compare the existing numerical methods in the context of outdoor sound propagation.

Based on previous studies carried out at the UMRAE laboratory, the TLM model is considered as a candidate to model sound propagation in forests. Indeed, this numerical method is a 2D/3D wave-based model that integrates most of the physical phenomena contributing to sound propagation within woodlands. In addition, its matrix formulation allows it to be parallelized over high-performance computing clusters. Therefore, the second chapter of this Ph.D. manuscript addresses the theoretical aspects of the TLM method. The main contribution of this part resides in the d-dimensional revised formulation of the model, which identified the TLM as equivalent to an order-two Finite Difference method in the Time Domain (FDTD). Thus, a comparison between TLM and equal-order and higher-order FDTD implementations, as well as dispersion relations, helped to understand the method's place in the ecosystem of wave equation solvers. Important consequences of the model theory revision were also drawn out, such as the non-validity of the atmospheric absorption in the presence of sound speed inhomogeneities. A superior order of integration of the recursive convolution in the TLM was also proposed compared to the available literature, allowing the model to maintain a second order when solving impedance boundary conditions.

The third chapter of the manuscript addresses the computational and technical aspects of the TLM implementation. Sound source analysis revealed that for a time-dependent source excitation, the resulting pressure is not solely determined by the input signal but is strongly influenced by the convolution with the model impulse response. Consequently, a numerical approach to assess the impulse response at the source node was proposed. However, the main

contribution of this chapter resides in the approach proposed to quantify numerical dispersion-induced errors as it is original to the existing literature. The methodology produces sound pressure level (SPL) error maps that reflect the impacts of numerical dispersion induced by spatial Cartesian grids. In terms of SPL, the reliability of TLM simulations was demonstrated for long-range free-field propagation scenarios. Then, an extension of the study above a perfectly reflective boundary revealed the high error levels that can rise when a coherent source signal is modeled. These discrepancies with analytical solutions were found to be caused by misplaced simulated interference patterns due to numerical dispersion errors.

Finally, the possibility to apply the TLM model to sound propagation within forests was demonstrated in the fourth chapter. In this study, the forests were modeled as distributions of cylinders over an impedance ground. In the process, perfectly reflective boundary conditions on trunk surfaces were found adapted for simulations below 2000 Hz and up to 40 m propagation distance. The original content of this chapter is the comparison of numerical simulations using real tree positions with in-situ sound measurements made in the Nouragues forest. Overall, the agreement between the measurements and the TLM predictions is encouraging, even if the spatial locations of the microphones and trees were approximated, based on the available data subject to uncertainties.

2 Perspectives

Several perspectives have emerged based on the results of this research. They are listed in the following paragraphs and sorted by chapters.

Chapter one An original way to model stems and leaves as homogenized volumes would be to transpose the effective wavenumber included in the parabolic equation applied to forests to time-domain methods. This improvement could save meshing complexity and enable the statistical description of forest features. In addition, a hybrid method coupling a time domain and a diffusion equation solver could be a workaround to take into account the high-frequency phenomena occurring during sound propagation through wooded environments.

Chapter two and three The adaptability of the TLM model - *i.e.* the link between the method and the Euler equations - could benefit from further investigations in the electromagnetic research field literature. Additional developments in its theory could then strengthen the TLM capacity to directly discretize equations. This could lead to an integration of the Adapted Differential Equation method and a formulation of perfectly matched layers for instance. Additionally, sound sources as initial conditions with spatial support could easily be implemented and the formulation of the TLM impulse response at the source node could be generalized to improve the source amplitude modeling.

Chapter four Although the acoustic measurements used in this doctoral work were not initially designed to be compared with TLM simulations, the comparison shows promising outcomes in future collaborations between the bioacoustics and numerical communities. Moreover, acoustic monitoring campaigns could benefit from in-situ impedance measurements of ground and bark to provide useful input data for simulations. Thus, parametric studies on the simulation input parameters could provide numerical error bars and improve the comparison methodology with experimental data. Further validation of the TLM model through a dedicated in-situ measurement campaign should also be considered. The accuracy of the recording conditions and geometric measurements of the environment should be of primary importance. For instance, trees description could be made more sophisticated thanks to technologies such as Lidar and 3D point clouds [20]. Complementary studies could also be considered, *e.g.* 3D printed scale

models in anechoic rooms enabling measurements in controlled laboratory conditions.

Finally, the outcomes of this doctoral work traduce that interdisciplinary collaborations involving specialists from bioacoustics, numerical methods and experimental research communities would lead to significant improvements for biodiversity conservation in forests. Indeed, sharing knowledge about which data is relevant from one community to another is crucial for the efficiency of research projects. Focusing on sound propagation models in the time domain that use spatial resolution on meshes, the main limitation resides in the computational resources needed to push further the high-frequency limit of modeling. This last point is fundamental when considering wildlife communication, which often has a wide frequency range of vocalizations.

Acknowledgments

I would like to express my gratitude to the following individuals and organizations who have contributed to the completion of this thesis:

Technical acknowledgments

The author would like to acknowledge the High Performance Computing Center of the University of Strasbourg for supporting this work by providing scientific support and access to computing resources. Part of the computing resources were funded by the Equipex Equip@Meso project (Programme Investissements d'Avenir) and the CPER Alsacalcul/Big Data.

The author would like to warmly thank the ISYEB team of the French National Museum of Natural History for sharing their measurement data, allowing me to go further in the TLM evaluation and to give a more ecological meaning to my work. Special thanks to Jérôme Châve for sharing the tree localization data.

Of course, thanks to the reviewers and jury members for attending the defense and for the great discussions that took place in the process. Special thanks to Didier and Guillaume for following my work during the CSIs for three years.

Personal acknowledgments - Remerciements

Merci à tous ces sommets,
d'altitudes égales,
situés dans les massifs de
Strasbourg, Nantes, Seattle,
Pornichet, Paris et Finkwiller!

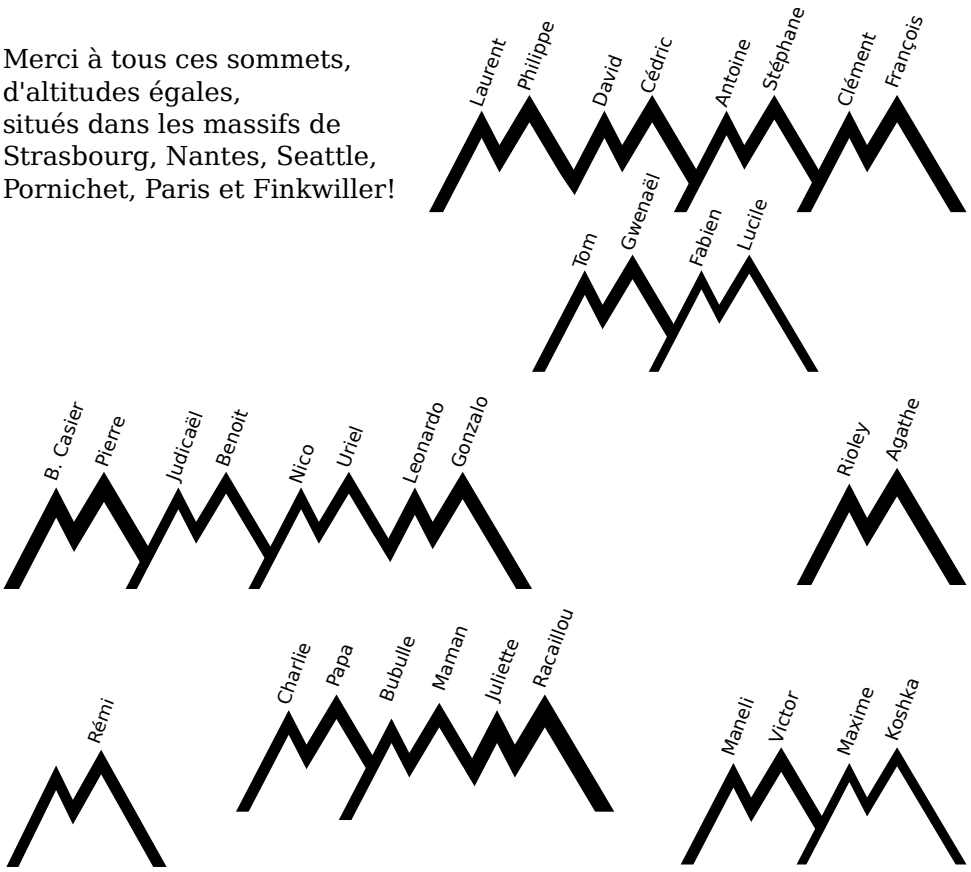

References

[1] *ANSI S1.26-1995 (R1999) - Method for the Calculation of Absorption of Sound by the Atmosphere.*

[2] *ISO 9613-1:1993 - Acoustics - Attenuation of sound during propagation outdoors - Part 1: Calculation of the absorption of sound by the atmosphere.*

[3] *Directive 2002/49/EC of the European Parliament and of the Council of 25 June 2002 relating to the assessment and management of environmental noise - Declaration by the Commission in the Conciliation Committee on the Directive relating to the assessment and management of environmental noise*, June 2002.

[4] D. G. Albert, M. E. Swearingen, F. E. Perron, and D. L. Carbee, *Low frequency acoustic pulse propagation in temperate forests*, The Journal of the Acoustical Society of America, 138 (2015), pp. 735–747.

[5] A. V. Astaneh, B. Keith and L. Demkowicz, *On perfectly matched layers for discontinuous Petrov-Galerkin methods*, Computational Mechanics, 63 (2019), pp. 1131–1145.

[6] K. Attenborough, I. Bashir and S. Taherzadeh, *Outdoor ground impedance models*, The Journal of the Acoustical Society of America, 129 (2011), pp. 2806–2819.

[7] K. Attenborough and T. V. Renterghem, *Chapter 10 - Predicting Effects of Vegetation, Trees and Turbulence*, in Predicting Outdoor Sound, Second Edition, CRC Press, Mar. 2021, pp. 467–547.

[8] ——, *Predicting Outdoor Sound*, CRC Press, Mar. 2021.

[9] K. Attenborough and S. Taherzadeh, *Sound propagation through forests and tree belts*, Proceedings of the Institute of Acoustics, 38 (2016), pp. 114–125.

[10] P. Aumond, G. Guillaume, B. Gauvreau, C. Lac, V. Masson, and M. Bérengier, *Application of the Transmission Line Matrix method for outdoor sound propagation modelling – Part 2: Experimental validation using meteorological data derived from the meso-scale model Meso-NH*, Applied Acoustics, 76 (2014), pp. 107–112.

[11] T. M. Barry, J. A. Reagan, null, and United States. Federal Highway Administration, *FHWA highway traffic noise prediction model*, tech. rep., Jan. 1978.

[12] H. E. Bass, L. C. Sutherland and A. J. Zuckerwar, *Atmospheric absorption of sound: Update*, The Journal of the Acoustical Society of America, 88 (1990), pp. 2019–2021.

[13] H. E. Bass, L. C. Sutherland, A. J. Zuckerwar, D. T. Blackstock, and D. M. Hester, *Atmospheric absorption of sound: Further developments*, The Journal of the Acoustical Society of America, 97 (1995), pp. 680–683.

[14] I. Baydoun, D. Baresch, R. Pierrat, and A. Derode, *Scattering mean free path in continuous complex media: Beyond the Helmholtz equation*, Physical Review E, 92 (2015), p. 033201.

[15] ——, *Radiative transfer of acoustic waves in continuous complex media: Beyond the Helmholtz equation*, Physical Review E, 94 (2016), p. 053005.

[16] M. C. Bérengier, M. R. Stinson, G. A. Daigle, and J. F. Hamet, *Porous road pavements: Acoustical characterization and propagation effects*, The Journal of the Acoustical Society of America, 101 (1997), pp. 155–162.

[17] E. Bocher, G. Guillaume, J. Picaut, G. Petit, and N. Fortin, *NoiseModelling: An Open Source GIS Based Tool to Produce Environmental Noise Maps*, ISPRS International Journal of Geo-Information, 8 (2019), p. 130.

[18] C. Bogey and C. Bailly, *A family of low dispersive and low dissipative explicit schemes for flow and noise computations*, Journal of Computational Physics, 194 (2004), pp. 194–214.

[19] E. Bossy and Q. Grimal, *Numerical Methods for Ultrasonic Bone Characterization*, in Bone Quantitative Ultrasound, P. Laugier and G. Haïat, eds., Springer Netherlands, Dordrecht, 2011, pp. 181–228.

[20] M. Bouvier, S. Durrieu, R. A. Fournier, and J.-P. Renaud, *Generalizing predictive models of forest inventory attributes using an area-based approach with airborne LiDAR data*, Remote Sensing of Environment, 156 (2015), pp. 322–334.

[21] H. Brumm and H. Slabbekoorn, *Acoustic Communication in Noise*, in Advances in the Study of Behavior, vol. 35, Academic Press, Jan. 2005, pp. 151–209.

[22] M. Bruneau, *Fundamentals of Acoustics*, ISTE Ltd, London ; Newport Beach, CA, 2006.

[23] R. T. Buxton, M. F. McKenna, D. Mennitt, K. Fristrup, K. Crooks, L. Angeloni, and G. Wittemyer, *Noise pollution is pervasive in U.S. protected areas*, Science, 356 (2017), pp. 531–533.

[24] G. Campos and D. Howard, *On the computational efficiency of different waveguide mesh topologies for room acoustic simulation*, IEEE Transactions on Speech and Audio Processing, 13 (2005), pp. 1063–1072.

[25] J. Chave, S. J. Davies, O. L. Phillips, S. L. Lewis, P. Sist, D. Schepaschenko, J. Armston, T. R. Baker, D. Coomes, M. Disney, L. Duncanson, B. Hérault, N. Labrière, V. Meyer, M. Réjou-Méchain, K. Scipal, and S. Saatchi, *Ground Data are Essential for Biomass Remote Sensing Missions*, Surveys in Geophysics, 40 (2019), pp. 863–880.

[26] P. Chobeau, *Modeling of Sound Propagation in Forests Using the Transmission Line Matrix Method: Study of Multiple Scattering and Ground Effects Related to Forests*, PhD thesis, 2014.

[27] P. Chobeau, D. Ecotière, G. Dutilleux, and J. Picaut, *An absorbing matched layer implementation for the transmission line matrix method*, Journal of Sound and Vibration, 337 (2015), pp. 233–243.

[28] P. Chobeau, G. Guillaume, J. Picaut, D. Ecotière, and G. Dutilleux, *A Transmission Line Matrix model for sound propagation in arrays of cylinders normal to an impedance plane*, Journal of Sound and Vibration, 389 (2017), pp. 454–467.

[29] A. Chopard, D. Ecotière, G. Dutilleux, P. Chobeau, and J. Picaut, *Etude paramétrique numérique de la propagation acoustique en forêt*, in Proceedings of CFA 2016, Le Mans, France, 2016.

[30] G. C. Cohen, *Higher-Order Numerical Methods for Transient Wave Equations*, vol. 110 of Scientific Computation, Springer Berlin Heidelberg, Berlin, Heidelberg, 2002.

[31] M. D. Collins, *A split-step Padé solution for the parabolic equation method*, The Journal of the Acoustical Society of America, 93 (1993), pp. 1736–1742.

[32] R. H. Cowie, P. Bouchet and B. Fontaine, *The Sixth Mass Extinction: Fact, fiction or speculation?*, Biological Reviews, 97 (2022), pp. 640–663.

[33] D. de Cogan, W. J. O'Connor and S. Pulko, *Transmission Line Matrix (TLM) in Computational Mechanics*, CRC Press, Nov. 2005.

[34] M. E. Delany and E. N. Bazley, *Acoustical properties of fibrous absorbent materials*, Applied Acoustics, 3 (1970), pp. 105–116.

[35] L. Ding, T. Van Renterghem, D. Botteldooren, K. Horoshenkov, and A. Khan, *Sound absorption of porous substrates covered by foliage: Experimental results and numerical predictions*, The Journal of the Acoustical Society of America, 134 (2013), pp. 4599–4609.

[36] M. Douillet, G. Sipos, L. Delugin, B. Bulliot, L. Remontet, and E. Bidault, *Estimation du coût social du bruit en France et analyse de mesures d'évitement simultané du bruit et de la pollution de l'air.*, tech. rep., ADEME, I CARE & CONSULT, ÉNERGIES DEMAIN, 2021.

[37] D. Dragna, *Modélisation Par Une Approche Temporelle de La Propagation Acoustique En Milieu Extérieur : Traitement de Frontières Complexes et Validation Sur Site Ferroviaire.*, PhD thesis, 2011.

[38] D. Dragna, K. Attenborough and P. Blanc-Benon, *On the inadvisability of using single parameter impedance models for representing the acoustical properties of ground surfaces*, The Journal of the Acoustical Society of America, 138 (2015), pp. 2399–2413.

[39] D. Dragna, P. Blanc-Benon and F. Poisson, *Modeling of Broadband Moving Sources for Time-Domain Simulations of Outdoor Sound Propagation*, AIAA Journal, 52 (2014), pp. 1928–1939.

[40] D. Dragna, B. Cotté, P. Blanc-Benon, and F. Poisson, *Time-Domain Simulations of Outdoor Sound Propagation with Suitable Impedance Boundary Conditions*, AIAA Journal, 49 (2011), pp. 1420–1428.

[41] D. Dragna, M. Hornikx, P. Blanc-Benon, F. Poisson, and R. Waxler, *Chebyshev pseudospectral time-domain method for simulations of outdoor sound propagation*, Jan. 2011.

[42] D. Dragna, P. Pineau and P. Blanc-Benon, *A generalized recursive convolution method for time-domain propagation in porous media*, The Journal of the Acoustical Society of America, 138 (2015), pp. 1030–1042.

[43] W. Duan and R. Kirby, *The sound power output of a monopole source in a cylindrical pipe containing area discontinuities*, in Proceedings of Acoustics 2012, Nantes, France, 2012, p. 7.

[44] C. A. Duquette, S. R. Loss and T. J. Hovick, *A meta-analysis of the influence of anthropogenic noise on terrestrial wildlife communication strategies*, Journal of Applied Ecology, 58 (2021), pp. 1112–1121.

[45] K. Duru, L. Rannabauer, A.-A. Gabriel, G. Kreiss, and M. Bader, *A stable discontinuous Galerkin method for the perfectly matched layer for elastodynamics in first order form*, Numerische Mathematik, 146 (2020), pp. 729–782.

[46] G. Dutilleux, J. Defrance, D. Ecotière, B. Gauvreau, M. Bérengier, F. Besnard, and E. L. Duc, *NMPB-Routes-2008: The Revision of the French Method for Road Traffic Noise Prediction*, Acta Acustica united with Acustica, 96 (2010), pp. 452–462.

[47] G. Dutilleux and A. Fontaine, *Bruit routier et faune sauvage*, Cerema Bron, (2015).

[48] D. Ecotière, M. Rumeau, D. Brassenx, F. Junker, H. Lefevre, E. Marchal, C. Ribeiro, and C. Rosin, *XP S 31-115 : Une nouvelle norme pour évaluer les incertitudes métrologiques pour la mesure du bruit dans l'environnement*, in Proceedings of CFA 2018, Le Havre, France, Apr. 2018.

[49] European Commission. Joint Research Centre. ICHP., *Common Noise Assessment Methods in Europe (CNOSSOS-EU): To Be Used by the EU Member States for Strategic Noise Mapping Following Adoption as Specified in the Environmental Noise Directive 2002/49/EC.*, Publications Office, LU, 2012.

[50] C. F. Eyring, *Jungle Acoustics*, The Journal of the Acoustical Society of America, 18 (1946), pp. 257–270.

[51] O. Faure, *Analyse Numérique et Expérimentale de La Propagation Acoustique Extérieure : Effets de Sol En Présence d'irrégularités de Surface et Méthodes Temporelles*, PhD thesis, 2014.

[52] D. Felbacq, G. Tayeb and D. Maystre, *Scattering by a random set of parallel cylinders*, JOSA A, 11 (1994), pp. 2526–2538.

[53] T. R. Feldpausch, L. Banin, O. L. Phillips, and et al., *Height-diameter allometry of tropical forest trees*, Biogeosciences (Online), 8 (2011), pp. 1081–1106.

[54] T. Gao, X. C. Wang, R. Chen, H. H. Ngo, and W. Guo, *Disability adjusted life year (DALY): A useful tool for quantitative assessment of environmental pollution*, Science of The Total Environment, 511 (2015), pp. 268–287.

[55] R. Gibb, E. Browning, P. Glover-Kapfer, and K. E. Jones, *Emerging opportunities and challenges for passive acoustics in ecological assessment and monitoring*, Methods in Ecology and Evolution, 10 (2019), pp. 169–185.

[56] K. E. Gilbert and X. Di, *A fast Green's function method for one-way sound propagation in the atmosphere*, The Journal of the Acoustical Society of America, 94 (1993), pp. 2343–2352.

[57] Q. Goestchel, G. Guillaume, D. Ecotière, and B. Gauvreau, *Analysis of the numerical properties of the transmission line matrix model for outdoor sound propagation*, Journal of Sound and Vibration, 531 (2022), p. 116974.

[58] E. Grinfeder, S. Haupert, M. Ducrettet, J. Barlet, M.-P. Reynet, F. Sèbe, and J. Sueur, *Soundscape dynamics of a cold protected forest: Dominance of aircraft noise*, Landscape Ecology, 37 (2022), pp. 567–582.

[59] A. Guibard, F. Sèbe, D. Dragna, and S. Ollivier, *Influence of meteorological conditions and topography on the active space of mountain birds assessed by a wave-based sound propagation model*, The Journal of the Acoustical Society of America, 151 (2022), pp. 3703–3718.

[60] G. Guillaume, *Application de La Méthode TLM à La Modélisation de La Propagation Acoustique En Milieu Urbain*, PhD thesis, 2009.

[61] G. Guillaume, P. Aumond, B. Gauvreau, and G. Dutilleux, *Application of the transmission line matrix method for outdoor sound propagation modelling - Part 1: Model presentation and evaluation*, Applied Acoustics, 76 (2014), pp. 113–118.

[62] G. Guillaume, O. Faure, B. Gauvreau, F. Junker, M. Bérengier, and P. L'Hermite, *Estimation of impedance model input parameters from in situ measurements: Principles and applications*, Applied Acoustics, 95 (2015), pp. 27–36.

[63] G. Guillaume and N. Fortin, *Optimized transmission line matrix model implementation for graphics processing units computing in built-up environment*, Journal of Building Performance Simulation, 7 (2014), pp. 445–456.

[64] G. Guillaume, N. Fortin, B. Gauvreau, J. Picaut, G. Guillaume, N. Fortin, B. Gauvreau, J. Picaut, and T. L. M. Opencl, *TLM OpenCL multi-GPUs implementation*, Acoustics 2012, al-0080417 (2012), pp. 3249–3255.

[65] G. Guillaume and J. Picaut, *A simple absorbing layer implementation for transmission line matrix modeling*, Journal of Sound and Vibration, 332 (2013), pp. 4560–4571.

[66] G. Guillaume, J. Picaut and G. Dutilleux, *Use of the transmission line matrix method for the sound propagation modeling in urban area*, The Journal of the Acoustical Society of America, 123 (2008), pp. 3924–3924.

[67] G. Guillaume, J. Picaut, G. Dutilleux, and B. Gauvreau, *Time-domain impedance formulation for transmission line matrix modelling of outdoor sound propagation*, Journal of Sound and Vibration, 330 (2011), pp. 6467–6481.

[68] J. Gulliver, D. Morley, D. Vienneau, F. Fabbri, M. Bell, P. Goodman, S. Beevers, D. Dajnak, F. J Kelly, and D. Fecht, *Development of an open-source road traffic noise model for exposure assessment*, Environmental Modelling & Software, 74 (2015), pp. 183–193.

[69] A. L. Hastings and John A. Volpe National Transportation Systems Center (U.S.), *Traffic Noise Model 3.0: Technical Manual*, Tech. Rep. FHWA-HEP-20-012, Dec. 2019.

[70] S. Haupert, F. Sèbe and J. Sueur, *Physics-based model to predict the acoustic detection distance of terrestrial autonomous recording units over the diel cycle and across seasons: Insights from an Alpine and a Neotropical forest*, Methods in Ecology and Evolution, 14 (2023), pp. 614–630.

[71] J. S. Hesthaven and T. Warburton, *Nodal Discontinuous Galerkin Methods: Algorithms, Analysis, and Applications*, no. 54 in Texts in Applied Mathematics, Springer, New York, NY, 2008.

[72] J. Hofmann and K. Heutschi, *Simulation of outdoor sound propagation with a transmission line matrix method*, Applied Acoustics, 68 (2007), pp. 158–172.

[73] M. Hornikx, *Ten questions concerning computational urban acoustics*, Building and Environment, 106 (2016), pp. 409–421.

[74] M. Hornikx, D. Botteldooren, T. Renterghem, and J. Forssén, *Modelling of scattering of sound from trees by the PSTD method*, in Forum Acusticum, Jan. 2011, p. 844.

[75] M. Hornikx, M. Kaltenbacher and S. Marburg, *A Platform for Benchmark Cases in Computational Acoustics*, Acta Acustica united with Acustica, 101 (2015), pp. 811–820.

[76] M. Hornikx, R. Waxler and J. Forssén, *The extended Fourier pseudospectral time-domain method for atmospheric sound propagation*, The Journal of the Acoustical Society of America, 128 (2010), pp. 1632–1646.

[77] International Electrotechnical Commission, International Electrotechnical Commission and Technical Committee 29, *Electroacoustics: Octave-Band and Fractional-Octave-Band Filters. Part 1*, 2014.

[78] ISO 9613-2, *Acoustics — Attenuation of sound during propagation outdoors — Part 2: General method of calculation*, Dec. 1996.

[79] M. D. Jennings and G. M. Harris, *Climate change and ecosystem composition across large landscapes*, Landscape Ecology, 32 (2017), pp. 195–207.

[80] E. Johansson, *The sound amplifying forest, with emphasis on sounds from wind turbines*, tech. rep., 2010.

[81] P. Johns, *On the Relationship Between TLM and Finite-Difference Methods for Maxwell's Equations (Short Paper)*, IEEE Transactions on Microwave Theory and Techniques, 35 (1987), pp. 60–61.

[82] P. Johns and R. Beurle, *Numerical solution of 2-dimensional scattering problems using a transmission-line matrix*, Proceedings of the Institution of Electrical Engineers, 118 (1971), pp. 1203–1203.

[83] Y. Kagawa, T. Tsuchiya, B. Fujii, and K. Fujioka, *Discrete Huygen's model approach to sound wave propagation*, Journal of Sound and Vibration, 218 (1998), pp. 419–444.

[84] Y. Kagawa, T. Tsuchiya, T. Hara, and T. Tsuji, *Discrete Huygens' modelling simulation of sound wave propagation in velocity varying environments*, Journal of Sound and Vibration, 246 (2001), pp. 419–439.

[85] B. Kayser, D. Mascarenhas, B. Cotté, D. Ecotière, and B. Gauvreau, *Validity of the effective sound speed approximation in parabolic equation models for wind turbine noise propagation*, The Journal of the Acoustical Society of America, 153 (2023), pp. 1846–1854.

[86] J. Khan, M. Ketzel, S. S. Jensen, J. Gulliver, E. Thysell, and O. Hertel, *Comparison of Road Traffic Noise prediction models: CNOSSOS-EU, Nord2000 and TRANEX*, Environmental Pollution, 270 (2021), p. 116240.

[87] C. Khodr, D. Dragna, P. Blanc-Benon, R. Marchiano, L. Aubry, O. Gainville, and C. Millet, *PLetma—Parallel software package for intensive infrasound simulation*, The Journal of the Acoustical Society of America, 150 (2021), pp. A180–A180.

[88] R. Kirby, *On the modification of Delany and Bazley fomulae*, Applied Acoustics, 86 (2014), pp. 47–49.

[89] J. Kragh, *Traffic Noise Prediction with Nord2000 - An Update*, in Proceedings of Acoustics 2011, Gold Coast, Australia, 2011.

[90] C. Lagarrigue, J. P. Groby and V. Tournat, *Sustainable sonic crystal made of resonating bamboo rods*, The Journal of the Acoustical Society of America, 133 (2013), pp. 247–254.

[91] M. Li, T. Van Renterghem, J. Kang, K. Verheyen, and D. Botteldooren, *Sound absorption by tree bark*, Applied Acoustics, 165 (2020), p. 107328.

[92] F. Mietlicki, D. Bernfeld and E. Thibier, *Quantification of the social cost of noise in France and application of the methodology to the Ile-de-France region*, in Internoise 2022, Glasgow, 2022.

[93] Y. Miki, *Acoustical properties of porous materials. Modifications of Delany-Bazley models.*, Journal of the Acoustical Society of Japan (E), 11 (1990), pp. 19–24.

[94] S. Miklavcic, J. Ericsson et al., *Practical implementation of the 3D tetrahedral TLM method and visualization of room acoustics*, Proceedings of the 7th Int. Conference on Digital Audio Effects, (2004), pp. 262–267.

[95] F. Monteghetti, *Analysis and Discretization of Time-Domain Impedance Boundary Conditions in Aeroacoustics*, PhD thesis, 2018.

[96] M. B. Muhlestein, V. E. Ostashev, D. K. Wilson, and D. G. Albert, *Acoustic pulse propagation in forests*, The Journal of the Acoustical Society of America, 143 (2018), pp. 968–979.

[97] T. Münzel, M. Sørensen and A. Daiber, *Transportation noise pollution and cardiovascular disease*, Nature Reviews Cardiology, 18 (2021), pp. 619–636.

[98] C. Nugent, N. Blanes, F. Jaume, and M. Sainz de la Maza, *Quiet areas in Europe — The environment unaffected by noise pollution — European Environment Agency*, publication, 2016.

[99] P. Opdam and D. Wascher, *Climate change meets habitat fragmentation: Linking landscape and biogeographical scale levels in research and conservation*, Biological Conservation, 117 (2004), pp. 285–297.

[100] W. H. Organization, *Environmental Noise Guidelines for European Region*, WHO Regional Office for Europe, Copenhagen, 2019.

[101] V. E. Ostashev, S. L. Collier, D. K. Wilson, D. F. Aldridge, N. P. Symons, and D. Marlin, *Padé approximation in time-domain boundary conditions of porous surfaces*, The Journal of the Acoustical Society of America, 122 (2007), pp. 107–112.

[102] V. E. Ostashev, D. Keith WILSON, M. B. Muhlestein, and K. Attenborough, *Sound propagation in a forest based on 3D multiple scattering theories*, (2019), pp. 574–581.

[103] V. E. Ostashev, M. B. Muhlestein and D. K. Wilson, *Radiative transfer formulation for forest acoustics*, The Journal of the Acoustical Society of America, 142 (2017), pp. 3767–3780.

[104] ——, *Extra-wide-angle parabolic equations in motionless and moving media*, The Journal of the Acoustical Society of America, 145 (2019), pp. 1031–1047.

[105] V. E. Ostashev and D. K. Wilson, *Acoustics in Moving Inhomogeneous Media*, CRC Press, Boca Raton, 2nd edition ed., Sept. 2015.

[106] V. E. Ostashev, D. K. Wilson, L. Liu, D. F. Aldridge, N. P. Symons, and D. Marlin, *Equations for finite-difference, time-domain simulation of sound propagation in moving inhomogeneous media and numerical implementation*, The Journal of the Acoustical Society of America, 117 (2005), pp. 503–517.

[107] V. E. Ostashev, D. K. Wilson and M. B. Muhlestein, *Effective wavenumbers for sound scattering by trunks, branches, and the canopy in a forest*, The Journal of the Acoustical Society of America, 142 (2017), pp. EL177–EL183.

[108] E. Peris, *Environmental noise in Europe — 2020 — European Environment Agency*, publication, 2020.

[109] Y. Reymen, M. Baelmans and W. Desmet, *Time-domain impedance formulation based on recursive convolution*, Collection of Technical Papers - 12th AIAA/CEAS Aeroacoustics Conference, 6 (2006), pp. 3674–3687.

[110] S. W. Rienstra, *Impedance models in time domain*, in 12th AIAA/CEAS Aeroacoustics Conference, no. May, Cambridge, MA, USA, 2006, pp. 1–20.

[111] S. Rigal, V. Dakos, H. Alonso, and et al., *Farmland practices are driving bird population decline across Europe*, Proceedings of the National Academy of Sciences, 120 (2023), p. e2216573120.

[112] T. D. Rossing, ed., *Springer Handbook of Acoustics*, vol. 4, Springer New York, New York, NY, 2014.

[113] I. Rudnick, *The Propagation of an Acoustic Wave along a Boundary*, The Journal of the Acoustical Society of America, 19 (1947), pp. 348–356.

[114] S. M. Rytov, Y. A. Kravstov and V. I. Tatarskii, *Principles of Statistical Radiophysics: Wave Propagation through Random Media*, Springer, 2011.

[115] E. M. Salomons, *Computational Atmospheric Acoustics*, Springer Netherlands, Dordrecht, 2001.

[116] P. Schäfer and M. Vorländer, *Atmospheric Ray Tracing: An efficient, open-source framework for finding eigenrays in a stratified, moving medium*, Acta Acustica, 5 (2021), p. 26.

[117] I. J. Scott and D. de Cogan, *An improved transmission line matrix model for the 2D ideal wedge benchmark problem*, Journal of Sound and Vibration, 311 (2008), pp. 1213–1227.

[118] G. Shannon, M. F. McKenna, L. M. Angeloni, K. R. Crooks, K. M. Fristrup, E. Brown, K. A. Warner, M. D. Nelson, C. White, J. Briggs, S. McFarland, and G. Wittemyer, *A synthesis of two decades of research documenting the effects of noise on wildlife*, Biological Reviews, 91 (2016), pp. 982–1005.

[119] J. Smardzewski, W. Batko, T. Kamisiński, A. Flach, A. Pilch, D. Dziurka, R. Mirski, E. Roszyk, and A. Majewski, *Experimental study of wood acoustic absorption characteristics*, Holzforschung, 68 (2014), pp. 467–476.

[120] J. Sueur, B. Krause and A. Farina, *Climate Change Is Breaking Earth's Beat*, Trends in Ecology & Evolution, 34 (2019), pp. 971–973.

[121] M. E. Swearingen and M. J. White, *Influence of scattering, atmospheric refraction, and ground effect on sound propagation through a pine forest*, The Journal of the Acoustical Society of America, 122 (2007), pp. 113–119.

[122] C. K. W. Tam and J. C. Webb, *Dispersion-Relation-Preserving Finite Difference Schemes for Computational Acoustics*, Journal of Computational Physics, 107 (1993), pp. 262–281.

[123] G. Taraldsen and H. Jonasson, *Aspects of ground effect modeling*, The Journal of the Acoustical Society of America, 129 (2011), pp. 47–53.

[124] A. I. Tarrero, M. A. Martín, J. González, M. Machimbarrena, and F. Jacobsen, *Sound propagation in forests: A comparison of experimental results and values predicted by the Nord 2000 model*, Applied Acoustics, 69 (2008), pp. 662–671.

[125] L. N. Trefethen, *Group Velocity in Finite Difference Schemes*, SIAM Review, 24 (1982), pp. 113–136.

[126] R. Troian, D. Dragna, C. Bailly, and M. A. Galland, *Broadband liner impedance eduction for multimodal acoustic propagation in the presence of a mean flow*, Journal of Sound and Vibration, 392 (2017), pp. 200–216.

[127] T. Tsuchiya, *Numerical simulation of sound wave propagation with sound absorption in time domain*, 13th International Congress on Sound and Vibration 2006, ICSV 2006, 4 (2006), pp. 2839–2846.

[128] A. Tunick, *Calculating the micrometeorological influences on the speed of sound through the atmosphere in forests*, The Journal of the Acoustical Society of America, 114 (2003), pp. 1796–1806.

[129] V. Twersky, *Multiple Scattering of Waves and Optical Phenomena*, JOSA, 52 (1962), pp. 145–171.

[130] T. Van Renterghem, *Efficient Outdoor Sound Propagation Modeling with the Finite-Difference Time-Domain (FDTD) Method: A Review*, International Journal of Aeroacoustics, 13 (2014), pp. 385–404.

[131] H. Wang and M. Hornikx, *Time-domain impedance boundary condition modeling with the discontinuous Galerkin method for room acoustics simulations*, The Journal of the Acoustical Society of America, 147 (2020), pp. 2534–2546.

[132] H. Wang, I. Sihar, R. Pagán Muñoz, and M. Hornikx, *Room acoustics modelling in the time-domain with the nodal discontinuous Galerkin method*, The Journal of the Acoustical Society of America, 145 (2019), pp. 2650–2663.

[133] Y. Wang, *Frequencies of the Ricker wavelet*, GEOPHYSICS, 80 (2015), pp. A31–A37.

[134] M. White and M. E. Swearingen, *Sound Propagation Through a Forest : A predictive model*, tech. rep., Engineer Research and Development Center, Champaign IL Construction Engineering Research Lab, 2004.

[135] G. W. Witmer, *Wildlife population monitoring: Some practical considerations*, Wildlife Research, 32 (2005), pp. 259–263.

[136] Q.-Y. Zhou, J. Park and V. Koltun, *Open3D: A Modern Library for 3D Data Processing*, Jan. 2018.

[137] C. Zwikker and C. Kosten, *Sound Absorbing Materials*, Elsevier Science Ltd, 1949.

Appendix A

TLM code specifications

This appendix is complementary to Section 3.1 and provides additional information on the TLM code.

1 Boundary material management

The `.ply` and `.json` files generated by FreeCAD API and Open3D respectively are complementary. The `.ply` files store triangular surface mesh geometric data, while the `.json` files contain information about materials and boundary conditions (see Listing A.2). This part of the implementation is new and was conducted during the doctoral research, including the supervision of a second-year computer science student from the University Institute of Technology (IUT) in Strasbourg. A correspondence table, displayed by Listing A.1, storing material names and indices has also been updated and should continue to be updated to ensure clarity and reproducibility.

Listing A.1. `materials_tab.json`

```
{
  "main": {
    "Out": -1,
    "Air": 0,
    "Raw": 1
  },
  "ground": {
    "RawGround": 2,
    "Pine10Ground": 9,
    "Beech34Ground": 11
  },
  "wood": {
    "FirWood": 4,
    "FirLeaves": 5,
    "OakWood": 6,
    "OakLeaves": 7,
    "GuyaBark" : 3,
    "SpruceBark": 8,
    "OakBarkMeasured": 10,
    "TestValAbs": 12
  }
}
```

Listing A.2. `copas.json`

```
{
  "bbox": {
   "vertex": [...],
   "face": [...],
   "material": {
    "name": "Raw",
    "id": 1,
    "matrix_value": 1,
    "reflection_coefficient": 1.0,
    "impedance_model": "",
    "impedance_parameters": {}
   },
   "global_face": [...]
  },
  "ground": {
   "vertex": [...],
   "face": [...],
   "material": {
    "name": "Pine10Ground",
    "id": 9,
    "matrix_value": 2,
    "reflection_coefficient": 1.0,
    "impedance_model": "SlitPore",
    "impedance_parameters": {
     "sigma": 102500.0,
     "omega": 0.58,
     "q": 1.3130643285972257,
     "Pr": 0.71
    }
   },
   "global_face": [...]
  },
  "tree_94_trunk": {...},
  "tree_99_trunk": {...},
   .
   .
   .
  "tree_233_trunk": {...},
  "tree_683_trunk": {
   "vertex": [...],
   "face": [...],
   "material": {
    "name": "Raw",
    "id": 1,
    "matrix_value": 1,
    "reflection_coefficient": 1.0,
    "impedance_model": "",
    "impedance_parameters": {}
   },
   "global_face": [...]
  }
}
```

2 Main contributions to the TLM code

Major modifications made to the code during this doctoral work include the following:

- Update from Python 2.7 to Python 3.8
- Automatization of the code installation on Linux OS
- Setting up Git versioning, with a branch designed for High Performance Computing (HPC)
- Complete change of the scenes generation and material properties' affectation
- PLRC implementation
- Debugging, maintenance and setting up safeties all over the code
- Docstring writing and documentation generation
- Data processing and results management developments
- 2704 commits since December 2020 and still growing

As the author of this document, I work and hope for an available public GitHub repository.

Appendix B

Analytic solutions for monopolar mass flow sources

For time-domain numerical methods, TLM included, it is relevant to know the free-field solution of the wave equation with sources. It enables partial validation of numerical results to assess the behavior of the model applied to academic test cases. First, let's consider the linearized wave equation written in pressure, in the presence of a monopolar mass flow source.

$$\Delta p - \frac{1}{c^2}\frac{\partial^2 p}{\partial t^2} = -\rho_0 \frac{\partial q}{\partial t}, \tag{B.1}$$

p being the acoustic pressure, c the medium sound celerity, ρ_0 the constant medium density and q a volumetric flow traducing the introduction of a volume of matter by unity of volume by unity of time.

Before any further theoretical developments, let's define the Fourier transform used afterward. For the time dependencies, the convention is as defined in the NUMPY.FFT() module:

$$TF\{f(t)\} = \hat{f}(\omega) = \int_{-\infty}^{+\infty} f(t)\exp(-i\omega t)dt, \tag{B.2a}$$

$$TF^{-1}\{\hat{f}(\omega)\} = f(t) = \frac{1}{2\pi}\int_{-\infty}^{+\infty} \hat{f}(\omega)\exp(i\omega t)d\omega \tag{B.2b}$$

1 Spherical source with Gaussian mass flow

Let's consider a spherical source of radius ϵ similarly as defined in [43], but with a Gaussian flow [22]:

$$q(\underline{r},t) = 4\pi\epsilon^2 v(\underline{r} = \underline{r}_0 + \underline{\epsilon})\exp(-\pi^2(f_c t - 1)^2)\delta(\underline{r} - \underline{r}_0)\mathrm{H}(t) = Q_0(t)\delta(\underline{r} - \underline{r}_0) \tag{B.3}$$

$\mathrm{H}(t)$ being the Heaviside function and $\delta(\underline{r} - \underline{r}_0)$ being the spatial Dirac density such as:

$$\int_\Omega \delta(\underline{r} - \underline{r}_0)d\Omega = 1. \tag{B.4}$$

Applying the Fourier transform to Eq. (B.1) leads to the Helmoltz equation:

$$\Delta\hat{h}(\underline{r},\omega) + k_w^2\hat{h}(\underline{r},\omega) = -\delta(\underline{r} - \underline{r}_s) \tag{B.5}$$

with $\hat{h}(\underline{r},\omega) = \dfrac{\hat{P}(\underline{r},\omega)}{-i\omega\rho_0\hat{Q}_0(w)}$ and $k_w = \pm\dfrac{w}{c}$. The known solutions of this equation in free-field are the Green functions of the free-field:

$$\hat{G}_d(\underline{r},\omega) = \begin{cases} \frac{1}{4i} H_0^{(1)}(-k_w r) \text{ in 2D, } H_0^{(1)} \text{ being the Hankel function of the first kind} \\ \frac{\exp(-ik_w r)}{4\pi r} \text{ in 3D.} \end{cases} \tag{B.6}$$

Then,

$$\hat{P}(\underline{r},\omega) = -i\omega\rho_0 \hat{Q}_0(w)\hat{G}_d(\underline{r},\omega), \tag{B.7}$$

and

$$p(\underline{r},t) = TF^{-1}\left\{-i\omega\rho_0\hat{Q}_0(w)\hat{G}_d(\underline{r},\omega)\right\}. \tag{B.8}$$

In 3D, the time-domain formulation of the Green function is relatively straight-forward [22] and then, the pressure can be written as:

$$\begin{aligned} p(\underline{r},t) &= -\rho_0 \frac{\partial q}{\partial t} * g_{3D}(\underline{r},t) = -\rho_0 \frac{\partial q}{\partial t} * \frac{1}{4\pi r}\delta\left(t - \frac{r}{c}\right) \\ p(\underline{r},t) &= \frac{\rho_0 f_c \pi Q_s}{2r} (f_c\tau) \exp\left(-\pi^2 (f_c\tau)^2\right), \text{ with } \tau = t - \frac{r}{c} \text{ the reduced time} \end{aligned} \tag{B.9a}$$

and $Q_s = 4\pi\epsilon^2 v(\underline{r} = \underline{r}_0)$, the spherical flow amplitude being set by two parameters.

2 Analytical image source

The analytical solution of the 2D case with one reflective boundary is computed using the image source theory. This formulation is only valid for purely reflective boundaries, *i.e.* with pressure reflection coefficient R=1 [113]. Thus, the unique input value needed to calculate the reflected pressure field p_{refl} is the distance r' between the image source **S'** and the receiver (Fig. B.1). The total acoustic pressure field $p_{\text{tot}}(r,t)$ is then described as follows:

$$p_{\text{tot}}(r,t) = p_{\text{direct}}(r,t) + p_{\text{refl}}(r',t) = p(r,t) + R \times p(r',t). \tag{B.10}$$

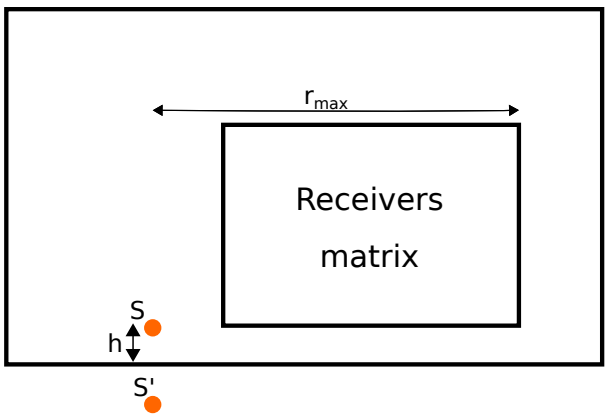

Figure B.1. Numerical experiment setup of Section 3.4 with the image source theory.

p being calculated as in Section 1. If the 2D case is considered and for a simulation setup as in Section 3.4, the distances r and r' become:

$$r = \sqrt{(x_{\text{mic}} - x_{\text{src}})^2 + (y_{\text{mic}} - y_{\text{src}})^2}, \tag{B.11a}$$

$$r' = \sqrt{(x_{\text{mic}} - x_{\text{src}})^2 + (y_{\text{mic}} + y_{\text{src}})^2}. \tag{B.11b}$$

However, when these distances are discretized throughout the TLM code, special care must be taken because of the spatial discretization of the domain. Indeed, as shown on Fig. B.2, the distance to the boundary surface is not exactly $\Delta x_i = j_i \Delta\ell$ because the meshing process introduces two artificial nodes to interface with the solver code [64]. The presence of the marker nodes ("outside" and "boundary") leads to:

$$\Delta x_i = (j_i - \frac{3}{2})\Delta\ell. \tag{B.12}$$

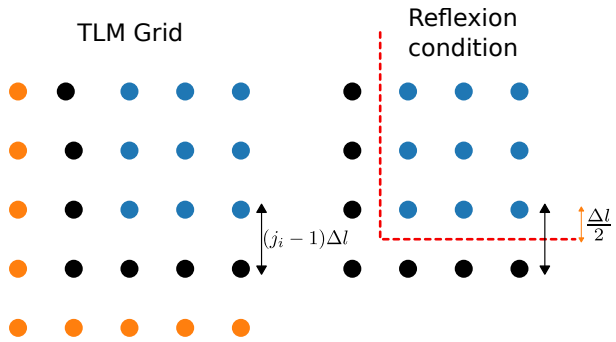

Figure B.2. Modeling of the boundaries in the TLM implementation. Orange dots: "outside" nodes; black dots: "boundary" nodes; blue dots: "fluid" nodes.

Thus, the distances of interest are computed as:

$$r_{j_1,j_2} = \sqrt{((j_1 - j_{\text{src}})\Delta\ell)^2 + ((j_2 - j_{\text{src}})\Delta\ell)^2}, \tag{B.13a}$$

$$r'_{j_1,j_2} = \sqrt{((j_1 - j_{\text{src}})\Delta\ell)^2 + ((j_2 + j_{\text{src}} - 3)\Delta\ell)^2}. \tag{B.13b}$$

Reintroducing these distances in Eq. (B.10) gives the analytical solution for the discrete pressure ${}_n p_{j_1,j_2}$.

Appendix C

NoiseModelling applied to generated forests

This appendix serves as support for a qualitative low-frequency comparison between the CNOSSOS-EU method implementation in the NoiseModelling software[1] [17] and the TLM model. The differences between the numerical methods are large, as CNOSSOS [49] is in the frequency domain and not designed for modeling sound propagation in forests, and the TLM model is in the time domain and integrates more sound propagation phenomena. Nevertheless, Fig. C.1 serves as basis for discussion on the differences between the results obtained using the TLM model and an engineering model. The figure should be analyzed carefully, as the colormap on Fig. C.1 is discrete whereas the one on Fig. 4.5b is continuous.

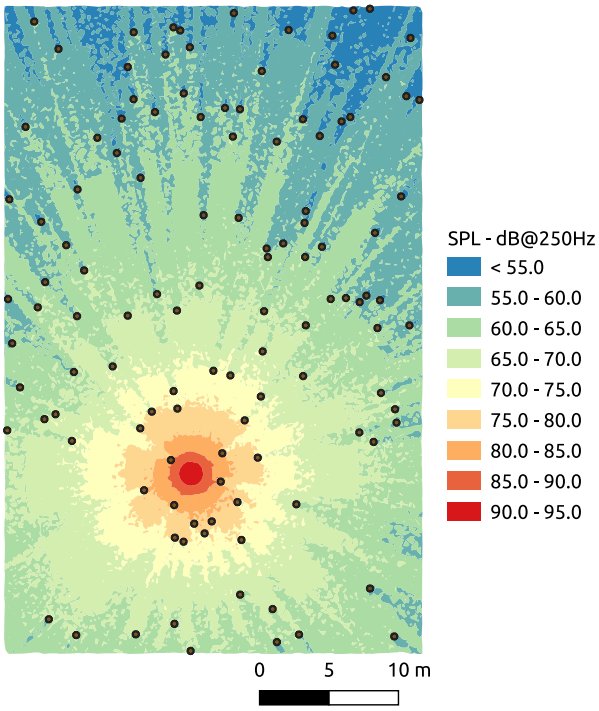

Figure C.1. Sound pressure level (SPL) map at 1.5m above the ground generated with NoiseModelling, $f_{\text{source}} = 250$ Hz.

To perform this simulation using NoiseModelling, a random distribution of 50000 receivers was generated in order to evaluate the sound pressure level on a dense grid of points. The calculation integrated paths between the source and the receivers with up to 10 reflections on

[1] NoiseModelling GitHub repository: https://github.com/Universite-Gustave-Eiffel/NoiseModelling

surfaces (reflection order of 10). The ground absorption is modeled with an adimensional parameter at the highest value possible (G=1). The diffraction feature of the model was activated to take into account vertical edges and horizontal edges.

Even if making a comparison between Fig. 4.5 and Fig. C.1 is highly debatable and qualitative, it enables some observations and discussions about wave-based numerical methods and engineering methods. Indeed, on Fig. 4.5b, the forest seems to have a stronger attenuating behavior than the one simulated with the ray-tracing method (Fig. C.1). This difference could be caused by the approximative implementation of the ground absorption and diffraction in the ray-tracing model compared to the impedance boundary condition and full-wave phenomena integrated in the TLM model. Additionally and as expected, multiple scattering and interferences appear to have an impact on the sound pressure levels that is not accounted by the ray-tracing method: the shapes of the observable patterns are specific of rays and waves for the respective method used.

Appendix D

Comparison with in-situ measurements - Frequency analysis

The following results are complementary to Section 4.3.6.

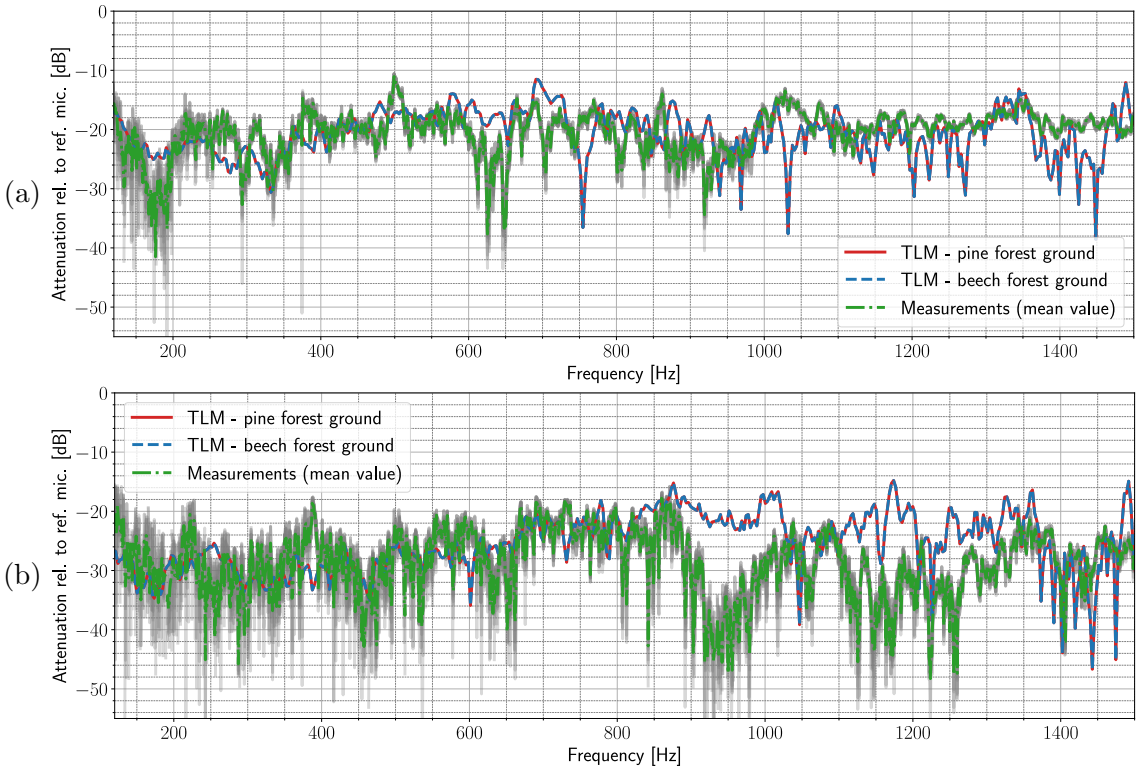

Figure D.1. Results comparison for a simulation with $f_{\max} = 1500\ Hz$, frequency analysis for different source-receiver distances. Attenuations relative to a reference microphone at 1 m from the source: TLM results for pine forest ground (orange line) and beech forest ground (blue dashed line), in-situ measurements (green dot-dashed line) with experimental dispersion (gray). Microphone at 10 m (a), 20 m (b), 30 m (c), 40 m (d).

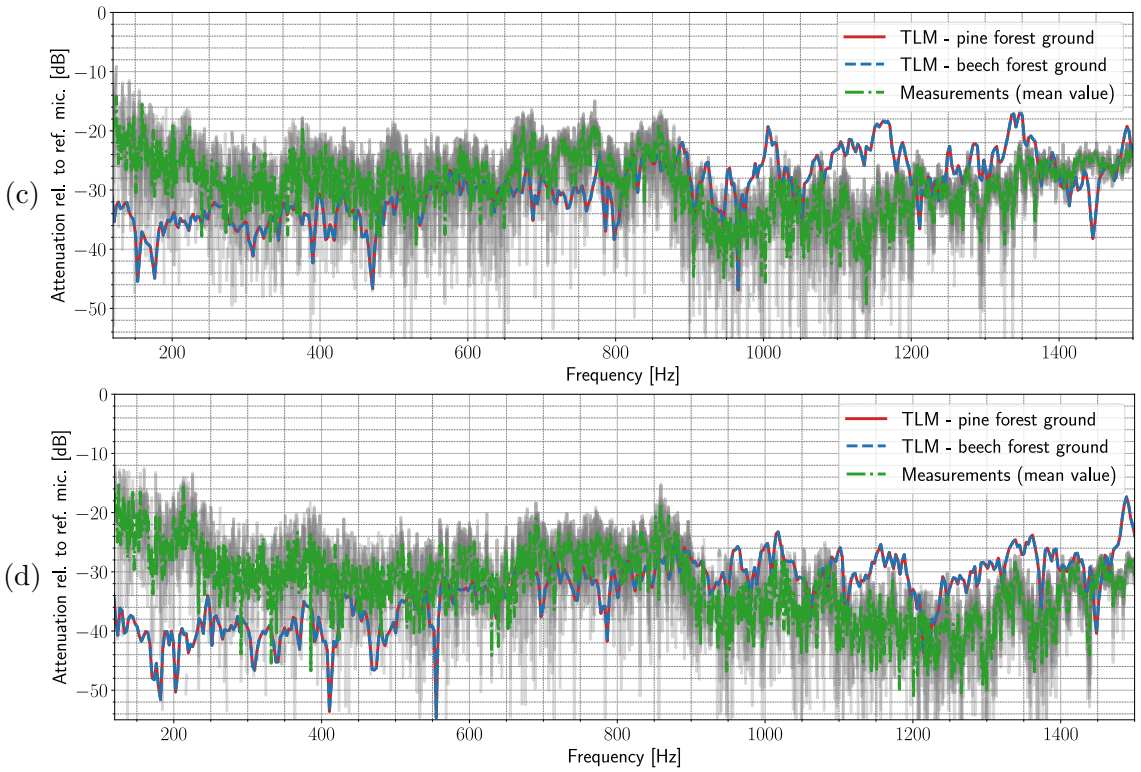

Figure D.1. Results comparison for a simulation with $f_{\max} = 1500\ Hz$, frequency analysis for different source-receiver distances. Attenuations relative to a reference microphone at 1 m from the source: TLM results for pine forest ground (orange line) and beech forest ground (blue dashed line), in-situ measurements (green dash-dotted line) with experimental dispersion (gray). Microphone at 10 m (a), 20 m (b), 30 m (c), 40 m (d).

zs

Appendix E

List of abbreviations

Abbreviation	Meaning
DALY	Disability Adjusted Life Years
UMRAE	*Unité Mixte de Recherche en Acoustique Environnementale* - Joint Research Unit in Environmental Acoustics
CEREMA	*Centre d'études et d'Expertise sur les Risques, l'Environnement, la Mobilité et l'Aménagement* - Centre for Studies on Risks, the Environment, Mobility and Urban Planning
UGE	University Gustave Eiffel
ISYEB	*Institut de Systématique, Évolution, Biodiversité*
MNHM	National Museum of Natural History (French)
EDB	Evolution and Biological Diversity laboratory
ISO	International Organization for Standardization
3D, 2D	Three Dimensions, Two Dimensions
PDE	Partial Differential Equation
GA	Geometrical Acoustics
CNOSSOS-EU	European Common Noise Assessment Methods
NMPB-2008	*Nouvelles Méthodes de Prédiction du Bruit - 2008*
TRANEX	TRANEX
FHWA	FHWA
FDTD	Finite Differences in Time Domain
LEE	Linearized Euler Equation
TLM	Transmission Line Matrix
TL	Transmission Line
CFL	Courant-Friedrichs-Lewy
Dr1OD2	First-order derivative, discretized at order two
Dr1OD4	First-order derivative, discretized at order four
Dr2OD2	Second-order derivative, discretized at order two
Dr2OD4	Second-order derivative, discretized at order four
PE	Parabolic Equation

Abbreviation	Meaning
WAPE	Wide Angle Parabolic Equation
CNPE	Crank-Nicolson Parabolic Equation
GFPE	Green's Function Parabolic Equation
TD - DG	Time Domain Discontinuous Galerkin
FEM	Finite Element Method
DGFEM	Discontinuous Galerkin Finite Element Method
PSTD	Pseudo-Spectral Time Domain
RTE	Radiative Transfer Equation
CAD	Computer-Aided Design
OS	Operating System
IUT	University Institutes of Technology (French higher education)
HPC	High-Performance Computing
PCRC	Piecewise Constant Recursive Convolution
PLRC	Piecewise Linear Recursive Convolution
ADE	Auxiliary Differential Equation
PML	Perfectly Matched Layer
AML	Adapted Matched Layer
FT	Fourier Transform
MSE	Mean Square Error
SPL	Sound Pressure Level
IR	Impulse Response
GPU	Graphic Processing Unit
CPU	Central Processing Unit
API	Application Programming Interface
CSR	Complete Spatial Randomness
GPS	Global Positioning System
GCS	Geographic Coordinate System
SNR	Signal to Noise Ratio

COLLEGE SCIENCES
DOCTORAL DE L'INGENIERIE
PAYS DE LA LOIRE ET DES SYSTEMES

Le Mans Université

Titre : Propagation acoustique en milieu boisé. Méthodes numériques dans le domaine temporel vers des applications à la bioacoustique.

Mots clés : Modèle de propagation du son, Forêt, Méthodes Numériques, Applications Ecologiques

Résumé : Ce manuscrit étudie la modélisation de la propagation du son dans les environnements forestiers, dans le but de mieux comprendre les modèles numériques et leurs applications possibles. Le sujet est introduit par une présentation des préoccupations existantes concernant l'impact du bruit sur la santé et la biodiversité. Une revue de la littérature examine les recherches précedentes et les modèles de propagation existants, tant analytiques que numériques, pour leur applicabilité aux forêts.

Ensuite, en tant que solveur dans le domaine temporel, le modèle Transmission Line Matrix (TLM) fait l'objet d'une étude approfondie, et la mise à jour de sa théorie permet de mettre en évidence certaines limitations pour les cas longue distance en extérieur.

Des expériences numériques sont ensuite présentées pour quantifier les erreurs et les limites du modèle TLM.

Les implications informatiques de la modélisation d'un nombre important de points impliqués par le rapport de distance-fréquence de simulations forestières sont discutées.

Des applications à des scénarios forestiers, avec de multiples conditions d'impédance sont présentées, et la validation est effectuée par des comparaisons avec des mesures in-situ provenant de la station de recherche des Nouragues (Guyane). Dans l'ensemble, cette recherche contribue à la compréhension de la simulation de la propagation du son dans les forêts et des applications pratiques potentielles qui peuvent en découler.

Title : Acoustic propagation in forest environments. Time domain numerical methods toward bioacoustic applications.

Keywords : Sound Propagation Model, Forest, Numerical Methods, Environmental Applications

Abstract : This manuscript investigates sound propagation modeling in forest environments, intending to understand the limitations of existing models and explore their potential bioacoustic applications. The subject is introduced by presenting current concerns about the impact of noise on health and biodiversity. A literature review examines previous studies and existing outdoor sound propagation models, both analytical and numerical, for their applicability to forest scenarios.

Then, as a time-domain solver, the Transmission Line Matrix (TLM) model is thoroughly investigated, and the update of its theory allows for highlighting limitations when modeling outdoor long-range sound propagation.

Numerical experiments are presented to quantify the subsequent errors and limitations in the TLM model. The computational implications of modeling a significant number of points implied by large frequency-distance ratios are discussed.

Finally, some applications to model sound propagation within forests, with multiple impedance boundary conditions, are presented, and a validation method is proposed through comparisons with in-situ measurements at the Nouragues research station (French Guiana). Overall, this research contributes to the understanding of how to simulate sound propagation within forests and the potential practical applications that can arise from it.